

# Two Problems in Viscous Flow: Fluid-Structure Interaction and Contact Drop Formation

by

Bian Qian

B.Eng., Mechanical Engineering, Shanghai Jiaotong University, 2003

M.Eng., Mechanical Engineering, National Univeristy of Singapore, 2006

M.Sc., Applied Mathematics, Brown University, 2009

A dissertation submitted in partial fulfillment of the  
requirements for the degree of Doctor of Philosophy  
in the Division of Engineering at Brown University

PROVIDENCE, RHODE ISLAND

May 2010

Abstract of “Two Problems in Viscous Flow: Fluid-Structure Interaction and Contact Drop Formation” by Bian Qian, Ph.D., Brown University, May 2010

This thesis deals with two problems in viscous flow.

In the first part, fluid-structure interactions were investigated, with connections to swimming microorganisms. Motivated by a numerically proposed swimming mechanism, we studied an elastic straight rod rotating on an imaginary cone. The shapes of the rod which rotates at either prescribed torques or speeds were experimentally measured and theoretically calculated. The rod undergoes a discontinuous transition to a helical shape at a critical torque, with increased propulsion force. A simple model was presented to capture and explain the essential physics. In addition, the longstanding hypothesis of hydrodynamic synchronization was investigated using a scale model experiment. We demonstrated that hydrodynamic interactions can cause synchronization between rotating paddles driven at constant torque if the shafts supporting the paddles have some flexibility. The synchronization state depends on the symmetry of the paddles and the torque mismatch. Excellent agreements were shown between the experiments and the regularized stokeslets simulations. And a simple analytic theory was built to predict the synchronization time as a function of paddle separation.

In the second part, contact drop formation on a hydrophobic surface was examined experimentally and theoretically. A wide range of droplet sizes can result from the same syringe by varying the dispensing speed. Three dispensing regimes were identified according to the motion of the contact line, a line coexisting between liquid/vapor/solid interfaces. In the fixed and the expanding contact-line regimes, a power dependence of the drop sizes on the dispensing speeds was observed experimentally and obtained theoretically. In the receding contact-line regime, the contact-line motion consists of two stages: a slow retraction at the beginning and a rapid retreation immediately prior to drop breakup. The dispensing process was modeled as a stretching liquid bridge with a free moving contact-line. A quasi-static analysis and numerical calculations were performed to accurately predict the initial evolution of the liquid bridge and the final breakup respectively. The

influences of the contact-line movement on the onset instabilities of liquid bridges and thus the deposited drop sizes were discussed.

© Copyright 2010 by Bian Qian

This dissertation by Bian Qian is accepted in its present form  
by the Division of Engineering as satisfying the  
dissertation requirement for the degree of Doctor of Philosophy.

Date \_\_\_\_\_  
Kenneth S. Breuer, Advisor

Recommended to the Graduate Council

Date \_\_\_\_\_  
Thomas R. Powers, Reader

Date \_\_\_\_\_  
Martin Maxey, Reader

Date \_\_\_\_\_  
Anubhav Tripathi, Reader

Approved by the Graduate Council

Date \_\_\_\_\_  
Sheila Bonde, Dean of the Graduate School

## The Vita of Bian Qian

Bian Qian was born in the city of Qinzhou, P. R. China. He graduated with a Bachelor degree in Mechanical Engineering from Shanghai Jiaotong University in China in 2003. Upon graduation, he attended National University of Singapore in Singapore to study fluid dynamics with Professor Sigurdur Thoroddsen and obtained a Master degree in Engineering. In 2005, he enrolled at Brown University in Providence to pursue a Doctor of Philosophy degree in Engineering under the guidance of Professor Kenneth Breuer. During the PhD study, he was awarded the Simon Ostrach Fellowship in 2008 and received another Master degree in Applied Mathematics from Brown University in 2009. Upon completion of his graduate studies, Mr. Qian plans to begin a postdoctoral appointment at Princeton University in Princeton, New Jersey.

## Preface

This dissertation consists of studies of the fluid-structure interactions in a viscous environment and the dynamics of liquid bridges stretching on a partial wetting surface. The contents are as follows:

**Chapter 1.** Introduction. Included are descriptions of the features in microorganisms swimming and contact drop dispensing, discussions of the fundamental questions arising therefrom, and reviews of the previous research works.

**Chapter 2.** “Shape transition and propulsive force of an elastic rod rotating in a viscous fluid” by Bian Qian, Thomas R. Powers and Kenneth S. Breuer. *Physical Review Letters*, **100**, 078101, 2008. Experiments were conceived, executed and analyzed by Qian with Breuer’s assistance. Theoretical calculations were carried out by Qian with Powers assisting in theoretical modeling. The simple lumped model was proposed by Breuer and analyzed by Powers. The summary of results was composed by Powers, Breuer and Qian.

**Chapter 3.** “Minimal model for synchronization induced by hydrodynamic interactions” by Bian Qian, Hongyuan Jiang, David Gagnon, Kenneth S. Breuer and Thomas R. Powers. *Physical Review E*, **80(6)**, 061919, 2009. The project was conceived by Powers, Breuer and Qian. Experiments were executed and analyzed by Qian and Gagnon. Numerical simulations and analytical modeling were carried out by Jiang and Powers. Results were interpreted and summarized by Powers, Breuer and Qian.

**Chapter 4.** “Micron-scale droplet deposition on a hydrophobic surface using a retreating syringe” by Bian Qian, Melissa Loureiro, David Gagnon, Anubhav Tripathi and Kenneth S. Breuer. *Physical Review Letters*, **102**, 164502, 2009. The project was conceived and designed by Loureiro, Tripathi, Breuer and Qian. Experiments were executed and analyzed by Qian and Loureiro with Gagnon’s assistance. Theoretical analyses and numerical calculations were carried out by Qian. Results were interpreted and summarized by Breuer and Qian.

**Chapter 5.** “The motion, stability and breakup of a stretching liquid bridge with a receding

contact line” by Bian Qian and Kenneth S. Breuer. submitted to *Journal of Fluid Mechanics*, 2010. Experiments, theoretical analyses and numerical simulations were carried out by Qian with Breuer assisting in interpreting and summarizing.

**Chapter 6.** Conclusion. Final remarks and recommendations for future work.

## Acknowledgments

First and foremost, I would like to express my deep gratitude and indebtedness to Professor Kenneth Breuer, for his guidance and assistance on every aspect of my research during the course of this work. He taught me the correct attitude towards work, the efficient way to solve problems, and the skills for lab and communication, which are great benefits to developing my professional academic career.

I would like to thank my dissertation readers, Professor Thomas Powers, Professor Anubhav Tripathi and Professor Martin Maxey, for their insightful comments during dissertation revisions. The previous and ongoing collaborations with Professor Thomas Powers, Professor Anubhav Tripathi and Doctor Hongyuan Jiang are deeply acknowledged, which are creative and produce the large portion of the work in this thesis.

I would also like to acknowledge all the members in the lab during my time at Brown University, Professor Peter Huang, Arnold Song, Charles Peguero, Rye Waldman, Rick He, John DiBenedetto, Alexandre de Chaumont Quitry, Melissa Loureiro, David Gagnon, Adam Hoffman, and Anthony Zorzos for their all kinds of helps. It is my pleasure to work within such a collaborative, active and productive research environment. A special thanks is due to my former labmates, Doctor Jeffrey Guasto, who is an outstanding teacher patiently introducing me the total internal reflection velocimetry system and a good friend generously sharing his experience and idea on researches and experiments.

In addition, many thanks are given to Michael Jibitsky of the Brown University Microelectronics Facility for instruction on using various equipments, Charles Vickers of the Joint Engineering Physics Instrument Shop for technical support, and especially our administrative assistant, Jeff Brown, for his kind administrative helps, which made research much easier.

My special appreciation goes to my parents and brother for their understanding, endless patience and continuous support through my education.

Finally, I would like to express special thanks to my wife Professor Wei Wang. Her love and mental support help me overcome all the difficulties during the course of this work. Without her help and encouragement, it would have been impossible for me to finish this work.

# Contents

<b>Preface</b>	<b>v</b>
<b>Acknowledgments</b>	<b>vii</b>
<b>1 Introduction</b>	<b>1</b>
1.1 SWIMMING OF MICROORGANISMS . . . . .	2
1.1.1 Swimming at low Re number . . . . .	3
1.1.2 Coordinated motions at low Re number . . . . .	6
1.2 CONTACT DROP DISPENSING . . . . .	7
1.2.1 Dominant dimensionless parameters . . . . .	9
1.2.2 Static liquid bridge with a fixed contact line . . . . .	10
1.2.3 Dynamic liquid bridge with a fixed contact line . . . . .	10
1.2.4 Liquid bridge with a moving contact line . . . . .	11
<b>2 Shape transition and propulsive force of an elastic rod rotating in a viscous fluid</b>	<b>14</b>
2.1 INTRODUCTION . . . . .	15
2.2 EXPERIMENT . . . . .	17
2.3 SIMPLE MODEL FOR ROTATING ROD . . . . .	18
2.4 THEORY . . . . .	19
2.4.1 Theoretical model . . . . .	19

2.4.2	Dominant dimensionless number . . . . .	20
2.4.3	Linear model equation . . . . .	21
2.5	RESULTS AND DISCUSSIONS . . . . .	23
<b>3</b>	<b>Minimal model for synchronization induced by hydrodynamic interactions</b>	<b>25</b>
3.1	INTRODUCTION . . . . .	26
3.2	EXPERIMENT . . . . .	28
3.3	NUMERICAL CALCULATION . . . . .	33
3.4	SIMPLE MODEL FOR ASYMMETRIC PADDLES . . . . .	35
3.4.1	Oseen tensor model . . . . .	35
3.4.2	Separation of time scales . . . . .	36
3.4.3	Dimensionless far-field equations of motion for $\theta_i$ and $\mathbf{x}_i$ . . . . .	37
3.4.4	Far-field equations of motion for average angular speed and phase difference . . . . .	38
3.4.5	Physical explanation for phase locking . . . . .	40
3.4.6	Power dissipation . . . . .	42
3.5	SIMPLE MODEL FOR SYMMETRIC PADDLES . . . . .	42
3.5.1	Oseen model and nondimensionalization . . . . .	42
3.5.2	Far-field equations of motion . . . . .	44
3.6	CONCLUSION . . . . .	49
<b>4</b>	<b>Micron-scale droplet deposition on a hydrophobic surface using a retreating syringe</b>	<b>50</b>
4.1	INTRODUCTION . . . . .	51
4.2	EXPERIMENT . . . . .	52
4.3	SCALING ARGUMENT . . . . .	55
4.4	NUMERICAL MODEL . . . . .	55
4.5	RESULTS AND DISCUSSIONS . . . . .	58

4.5.1	Scaling velocity for dispensing speed . . . . .	58
4.5.2	Contact line speeds for retreating contact lines . . . . .	58
4.6	CONCLUSION . . . . .	60
<b>5</b>	<b>The motion, stability and breakup of a stretching liquid bridge with a receding contact line</b>	<b>61</b>
5.1	INTRODUCTION . . . . .	62
5.2	EXPERIMENTAL SETUP . . . . .	66
5.3	THEORETICAL CONSIDERATIONS . . . . .	67
5.3.1	Stability of an equilibrium static liquid bridge . . . . .	67
5.3.2	Numerical model of a dynamic stretching liquid bridge . . . . .	69
5.4	RESULTS AND DISCUSSIONS . . . . .	70
5.4.1	Overall behavior of constant volume deposition . . . . .	70
5.4.2	Stability of static liquid bridge . . . . .	74
5.4.3	Dynamics of the stretching liquid bridge . . . . .	79
5.5	CONCLUSION . . . . .	84
<b>6</b>	<b>Conclusion</b>	<b>87</b>
<b>A</b>	<b>Oseen tensor for symmetric paddles</b>	<b>89</b>

# List of Tables

# List of Figures

1.1	Fluorescent flagellar filaments of <i>E.coli</i> . . . . .	2
1.2	Swimming patterns of hyperactivated bull spermatozoa . . . . .	3
1.3	Illustration of drop dispensing on a hydrophobic surface . . . . .	8
1.4	Images of drop dispensing on a partial wetting surface at different syringe speeds . . . . .	12
2.1	Orthogonal images of steady-state shapes of rotating rod with torque below and above the critical torque . . . . .	16
2.2	Sketch of the lumped parameter model . . . . .	17
2.3	Dimensionless rotational torque measured as a function of rotational speed . . . . .	19
2.4	Equilibrium shapes of a rotating filament from experimental measurements . . . . .	22
2.5	Theoretical calculation of the dimensionless propulsion force . . . . .	24
3.1	Schematic of the model system for hydrodynamic synchronization . . . . .	27
3.2	Phase difference versus dimensionless time for symmetric and asymmetric paddles . . . . .	30
3.3	Dimensionless synchronization time versus dimensionless gap size for symmetric and asymmetric paddles . . . . .	30
3.4	Comparison of phase difference evolution between experiment and numerical simulation . . . . .	31
3.5	Phase difference evolution at various rotational torque for symmetric paddles . . . . .	31
3.6	Influence of torque mismatch on the the steady state of phase-lock . . . . .	33
3.7	Model for asymmetric paddles. . . . .	36

3.8	Physical explanation for synchronization. . . . .	41
3.9	Model for symmetric paddles. . . . .	43
4.1	Typical sequence of images of drop dispensing at different syringe speeds . . . . .	53
4.2	Pinch-off height in regions of expanding and fixed contact line . . . . .	54
4.3	Normalized drop sizes at different scaled syringe speeds for three syringe radii . . . . .	56
4.4	Contact line speed versus contact line location for various scaled syringe speeds . . . . .	57
5.1	Geometry and coordinate system for an axisymmetric liquid bridge with a free moving contact line on the substrate. . . . .	63
5.2	Typical sequence of images of drop dispensing on a hydrophobic surface with a receding contact line and corresponding measured contact line locations as a function of bridge's heights. . . . .	71
5.3	Experimentally measured dimensionless contact line speeds from constant volume dispensing for different rod speeds . . . . .	73
5.4	Experimentally measured dispensing drop sizes vary with rod speeds for three bridge volumes. . . . .	74
5.5	Starting moving point of a fixed contact line $\Upsilon = 1$ on the $(\Lambda, V)$ plane under a constraint of the contact angle $\theta \geq \theta_r$ . . . . .	75
5.6	Static calculation of the locations of a free moving contact line as a function of the bridge height under a contact angle constraint . . . . .	76
5.7	Evolution of contact lines from static calculation compared to those from experiments at three different stretching speeds . . . . .	77
5.8	Calculated critical radius as a function of limiting wetting angles from static theory . . . . .	79
5.9	Calculated dispensing drop sizes compared to experiment for three bridge volumes . . . . .	80
5.10	Comparison in contact line speeds between experiments and numerical calculations with the velocity dependent contact angle model . . . . .	82

5.11 Effects of static receding angles on the contact line speeds for one stretching speed	
from dynamic contact angle calculation . . . . .	83
5.12 Influences of model parameters on the numerically calculated drop sizes . . . . .	84

# Chapter 1

## Introduction

The motion of fluid is governed by Navier-Stokes equations which are derived from the conservation of mass and momentum for an arbitrary control volume. For an incompressible flow of a Newtonian fluid with constant density  $\rho$  and constant viscosity  $\eta$ , the dimensionless form of the Navier-Stokes equations is

$$\frac{\partial \mathbf{u}}{\partial t} + \mathbf{u} \cdot \nabla \mathbf{u} = \frac{1}{\text{Re}}(-\nabla p + \nabla^2 \mathbf{u}), \quad (1.1a)$$

$$\nabla \cdot \mathbf{u} = 0, \quad (1.1b)$$

where  $t$  is the time,  $\mathbf{u}$  is the flow velocity, and  $p$  is the pressure. The relevant dimensionless parameter in the equations of motion is the Reynolds number, which is defined as  $\text{Re} = \rho LU/\eta$ .  $L$  and  $U$  is the characteristic length and the characteristic flow velocity. The Reynolds number gives a measure of the relative importance of inertial forces,  $\rho U^2 L^2$ , to viscous forces,  $\eta UL$ . The fluid flow where inertial forces are negligible in comparison to viscous forces,  $\text{Re} \ll 1$ , is called viscous flow or Stokes flow. Viscous flows exist when the length scales involved are pretty small. Examples include swimming of microorganisms and flows in microchannels. In this thesis, we considered two problems in viscous flow. One is the fluid-structure interaction, with connections to swimming of

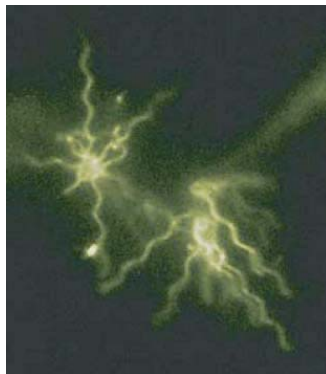


Figure 1.1: Fluorescent flagellar filaments of *E.coli*. Reprint from [6].

microorganisms. Another one is the contact drop formation, with applications to microdispensing.

## 1.1 SWIMMING OF MICROORGANISMS

Motile microorganisms have been studied for a long time and are still of great interest to date due to their significance in industry and technology. In industry, bacteria in combination with yeasts have long been used for preparing fermented foods. The ability of bacteria to degrade organic compound has also been widely used in waste water treatment and bioremediation. Recently, the potential use of bacteria has been explored in a variety of microfluidics systems and biomedical applications. Flagellated bacteria are ideal actuators for enhancing mixing and transportation of flows in microchannels [1, 2]. The chemotactic ability of bacteria can be used for detecting specific chemicals of interest [3, 4]. Moreover, bacteria as well as micro-scale artificial swimmers are promising workhorses for delivering drug and chemicals [5]. These applications take advantage of the swimming motions of microorganisms and motivate intensive experimental and theoretical investigations of microorganisms motility.

Many microorganisms propel themselves by exploiting the motions of flagella attached in their bodies. These filamentous appendages can be semi-rigid helix or rod-like flexible filaments. For example, *Esherischi coli* is a swimmer based on helical flagella which are randomly distributed

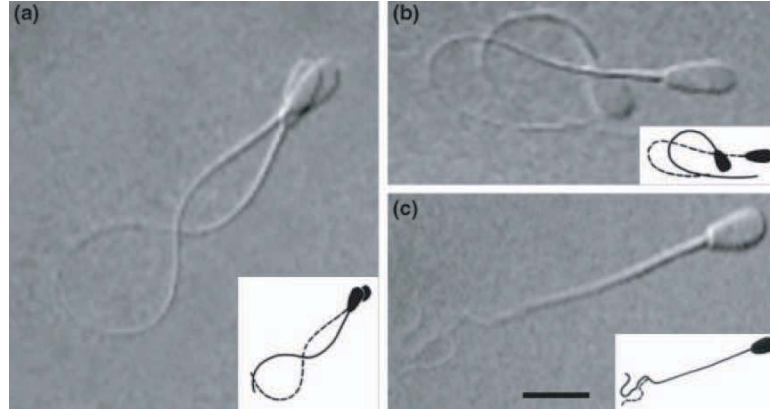


Figure 1.2: Images of bull spermatozoa swimming in shallow chambers. (a) an activated sperm in a viscous fluid. (b) a hyperactivated sperm in a viscous fluid. (c) a hyperactivated sperm in a viscoelastic fluid. Reprint from [7].

around its cell body (Fig.1.1). Each filament is connected to a molecular motor via a hook. When all of the motors rotate counter-clockwise, the filaments gather to form a tight bundle that pushes the cell forward. When one or more motors spin clockwise, the filaments leave the bundle and the cell body displays a “tumble” motion [3]. *Spermatozoa* swim, as distinct from *E. coli*, using the beating deformation of its flexible flagellum, which is actuated by the motors distributed along the filament (Fig. 1.2-a). The beat patterns of flagella are not only determined by the actuation but also affected by the surrounding flows. Evidence for this is that the swimming pattern of a sperm in a Newtonian fluid is different from that in a complex fluid (Fig. 1.2). Since the beat pattern affects the swimming motion, it is important to understand how the filamentous structures interact with the surrounding fluids and how these fluid-structure interactions lead to locomotion.

### 1.1.1 Swimming at low Re number

In contrast with fish swimming by imparting momentum to the surrounding fluid, microorganisms use viscous forces to propel themselves. This difference in swimming mechanisms can be understood by taking a look at the Reynolds number. A fish swimming in water ( $\rho \approx 10^3 \text{ kgm}^{-3}$ ,  $\eta \approx 10^{-3} \text{ Pa}$  s) with a speed,  $U \approx 0.1 \text{ m/s}$ , and a body length,  $L \approx 0.1 \text{ m}$ , has a Reynolds number  $\text{Re} = 10^4$ .

Therefore, the flow around its body is dominated by inertial forces. For bacteria, such as *E. coli* with  $U \approx 10 \mu\text{ms}^{-1}$  and  $L \approx 1 - 10 \mu\text{m}$ , the Reynolds numbers are pretty small,  $Re \approx 10^{-5} - 10^{-4}$ . In the limit of  $Re \ll 1$ , the viscous term becomes dominant and the inertial term can be appropriately ignored, for which the governing equations (1.1) simplify to Stokes equations,

$$-\nabla p + \nabla^2 \mathbf{u} = 0, \quad (1.2a)$$

$$\nabla \cdot \mathbf{u} = 0. \quad (1.2b)$$

The time-independence and the linearity of Stokes equations lead to the “scallop theorem” which states that any reciprocal body deformation does not contribute to the average motion regardless of the rate at which the body deforms [8].

To escape the scallop theorem, many microorganisms deform their flexible flagella to generate non-reciprocal motions. One example of such organisms is *Spermatozoon*, an uniflagellar sperm having a  $50 \mu\text{m}$  long tail. The core of its tail is an axoneme, which consists of two central microtubules and nine outer microtubules doublets. The relative sliding of the neighboring microtubule doublets causes the tail to bend [9]. This bending motion like a wave propagates along the tail, producing a net propulsion force. Another example is provided by *Chlamydomonas*. This biflagellated alga sweeps its flagella in a non-reciprocal fashion [10]. Each cycle motion consists of a rigid power stroke and a relaxed recovery stroke. During the power stroke, the straight flagella beat stiffly and experience large friction. As they pull back during the recovery stroke, the flagella fold, thereby offering lower resistance. The difference of viscous drag during these two strokes results in a movement.

The propulsion generated by flagellar deformation has motivated some theoretical modeling. In an early work, Machin [11] considered a filament passively actuated by angular oscillation of the proximal end. The deformation of the filament was determined by balancing the bending force with the viscous drag from the fluid. To simplify the modeling, Machin assumed the filament was

vanishingly thin and its deflection from the straight state was small. With these simplifications, he derived a hyper-diffusion equation for the shape of the filament. The solution of this equation indicated that a bending wave propagates from the proximal end to the distal end with exponential decay of the amplitude. Noting that the resulting wave form did not agree with the experimentally observed one, Machin concluded that there must be active actuating elements existing along the length of the flagellum. Another important finding in Machin’s work is that the wave length and the damping distance of the bending wave were proportional to a scale length  $l_0 = (A/\xi_{\perp}\omega)^{1/4}$ . This scale length depends on the bending modulus of the filament  $A$ , the actuation frequency  $\omega$ , and the perpendicular viscous coefficient  $\xi_{\perp}$  [12]. The ratio of the filament length to this scale length,  $S_p = L/l_0$ , is a relevant dimensionless number which is often called the ‘sperm number’. The ‘sperm number’  $S_p$  represents the relative importance of viscous to elastic stress on the filament, and it governs the shape of the filament and thus the propulsion force. When  $S_p \ll 1$ , the filament behaves like a rigid rod and no propulsion is generated. In the limit of  $S_p \gg 1$ , the filament undulates appreciably. Further examination of Machin problem showed that the optimal propulsion force was around  $S_p \approx 2$  [13], and this observation was confirmed in a table-top experiment [14].

Another related fluid-structure interaction problem, an elastic filament rotating on a cone driven by a torque, was investigated by Manghi *et al.* [15, 16]. Using numerical methods, they calculated the equilibrium shapes and the rotational speeds of the filament at prescribed driven moments. At low torque, the filament rotates slowly and rigidly. As torque increases, the filament bends to balance the viscous drag. Since the friction is larger at the free end, the filament adopts a curved shape. At a critical torque, the free end of the filament abruptly jumps close to the rotational axis and the filament takes a helical shape. This shape bifurcation induces a dramatic increase in the rotational speed and the propulsion force. Motivated by these observations, we built an experimental system to realize this design. The equilibrium shapes of the filament have been measured either at prescribed torques or at rotational speeds. A theoretical model was built to predict the filament shape and the propulsion force. In Chapter 2 of this thesis, the experiment results are presented

and compared along with the theoretical predictions, and the observed behaviors are interpreted via a simple physical model.

### 1.1.2 Coordinated motions at low Re number

Coordination is ubiquitous in swimming motions of microorganisms. One example of such phenomena is the in-phase beating of flagella. *Chlamydomonas reinhardtii*, a biflagellated alga, switches between whip-like and folded beating. When both flagella beat synchronously, the non-reciprocal deformation of the flagella produce a net force pulling the cell body. In contrast, out-of-phase beating causes a force mismatch in the moving direction and results in a moment to reorient the cell body, which is the mechanism used by *Chlamydomonas* for steering [17, 18]. Similar in-phase beating, but in a different form, occurs as individual spermatozoa cells come into close proximity [19]. Another example is provided by swimming *Paramecium* whose body is covered by densely packed hair-like cilia [20]. These cilia, though actuated independently, beat at a constant phase difference with respect to their neighbors and exhibit a directional traveling wave, which is termed a *metachronal wave*. The metachronal wave propels and directs the surrounding fluid in a continuous way, which is critical for many biological processes such as sweeping mucus out of the lungs, transporting sperm during fertilization [21], and breaking organ symmetry in developing vertebrate embryos [22].

The origin of these coordinative behaviors is one of the central questions of microorganism swimming. A long proposed mechanism is that these synchronous motions are mediated by the surrounding fluid which functions like the supporting beam in synchronization of pendulums [23]. The theoretical investigation of this hypothesis was initiated by G. I. Taylor [24]. Motivated by the in-phase beating of spermatozoa flagella, Taylor studied two infinite sheets nearby undulate in a sinusoidal form. He found that whatever the initial phase difference between the sheets there is a force that arises from hydrodynamic interaction which drives the sheets into phase. The energy dissipation also achieves a minimum in synchrony. In contrast to the fixed undulation in Taylor's

model, the beating motion of an individual flagellum (or cilium) is modulated by the flow induced by the neighbors. The fact of dynamic change of the beating motion was included into the modeling in the subsequent studies of collective motions of cilia. Via a phenomenological model of the internal force of cilia, numerical simulation has successfully reproduced the metachronal wave observed in ciliary movement [25, 26]. In the spirit of modeling a cilium as a discrete phase oscillator, a simple model has been developed recently to analytically study the phase-lock between neighboring cilia [27]. The most important modification in this model, comparing to the previous work [28], is the inclusion of some kind of flexibility so that the phase oscillator allows to be perturbed from the prescribed trajectory, which has agreements with the previous numerical simulation of hydrodynamic interaction between rigid helices [29, 30].

Although more and more theoretical and numerical works have provided evidences in support of the conjecture of hydrodynamic synchronization, there are few experiments that can be used to test the existing theories. For this reason, we set up a scaled experiment to find out the minimum ingredient required for hydrodynamic synchronization and quantify the dependence of synchronization on system parameters. In Chapter 3, the model system is described, and the experimental results are discussed along with numerical and analytical calculations.

## 1.2 CONTACT DROP DISPENSING

Contact drop dispensing is a technique that produces small liquid drops by deforming and breaking a liquid column entrapped between two solid surfaces. The dispensing process consists of two steps. First, a wetted tip is brought into contact with a substrate. When in contact, a liquid bridge forms between the tip and the substrate (Fig. 1.3). Secondly, the tip is raised to stretch the liquid bridge. At a critical height, the liquid bridge becomes unstable and then breaks up, which leaves a drop on the substrate. Contact drop dispensing has broad applications in industry and technology. It is an integral part of a number of industrial processes, such as ink-jet printing, assembling and packaging

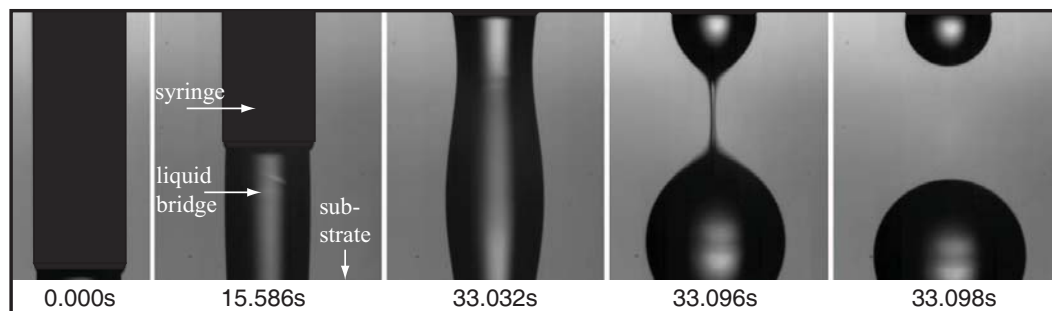


Figure 1.3: Sequence of images of drop dispensing on a hydrophobic surface.

of integrated circuit, manufacture of particles and microcapsules. The drop-based microarrays have emerged as powerful tools for DNA and biochemical analysis [31]. Most recently, contact drop dispensing has been adapted for nanostructure fabrications, such as direct scanning probe lithography [32] and micromachined fountain-pen techniques [33]. Given the current importance of biochip analysis and microfluidics, the deposited drops should be monodisperse and amenable to miniaturization, and the dispensing process should be repeatable and fast. These requirements present challenges to the current technique and motivate a number of experimental and theoretical investigations of contact drop formation.

Study of drop formation is a challenging problem for experimentalists, theoreticians, and computational scientists. In experiment, to capture the rapid motions of liquid-bridge ruptures requires ultrafast imaging systems. The up-to-date fastest imaging system is capable of taking 100 million pictures per second [34] but it is costly. Additionally, strong illumination is needed for this imaging system and the heat from the illumination might have undesired effects on the liquid. Moreover, to capture the final stage of drop pinch-off, the imaging system must have high optical resolutions, which demands higher illumination input. In theory, studies of contact drop formation are based on a simplified model, in which the dispensing process is modeled as a stretching liquid bridge with imposed boundary conditions. The equations for modeling a stretching liquid bridge are highly nonlinear and intractable analytically. The solutions of these equations mainly rely on the numeri-

cal calculations. Several numerical algorithms have been developed and have achieved successes in predictions of breakup features and liquid-bridge evolutions. However, it is numerically challenging to capture the finite-time singularity exhibited in liquid-bridge breakup. Moreover, the boundary effects, such as flow inside the syringe and dynamic wetting on the substrate, are still not clear due to the difficulties of modeling and numerical treatment.

### 1.2.1 Dominant dimensionless parameters

Although an accurate prediction is difficult, we can get some physical insights into this complex problem through dimensional analysis. During stretching, the liquid bridge is subject to gravitational, inertial, viscous, and capillary forces. Performing dimensionless analysis leads to three relevant dimensionless numbers: Weber number  $We \equiv \rho U^2 R / \gamma$ , Bond number  $Bo \equiv g \rho R^2 / \gamma$ , and capillary number  $Ca \equiv \mu U / \gamma$ . Here  $U$  is the syringe speed,  $R$  is the syringe diameter,  $g$  is the gravity constant.  $\rho$ ,  $\mu$  and  $\gamma$  is the density, the viscosity and the surface tension of liquid. These three dimensionless groups represent the relative importance of inertial force/surface tension, gravity/surface tension and viscous force/surface tension respectively. Note that in the capillary number the syringe speed  $U$  is used as the typical flow speed, which is correct during bridge stretching. If we form a capillary number using the capillary wave speed,  $u_{cp} = \sqrt{\gamma / \rho R}$ , instead of the syringe speed, we arrive at the Ohnesorge number,  $Oh \equiv \mu u_{cp} / \gamma$ , which is a better measure of the relative importance of viscous force/surface tension during bridge breakup. In this thesis, we were interested in drop dispensing in micron scale. Therefore, with a typical syringe speed  $U = 0.01$  m/s, the dimensionless numbers have values,  $We \sim \mathcal{O}(10^{-4})$ ,  $Bo \sim \mathcal{O}(10^{-3})$ , and  $Ca \sim \mathcal{O}(10^{-3})$ . These small values implicate that during bridge stretching only the capillary forces are important and the bridge evolution is considered to be quasi-static.

### 1.2.2 Static liquid bridge with a fixed contact line

The static liquid bridge has been investigated intensively due to its applications to crystal growth. The main goal of studying static liquid bridge is to predict the stabilities of the liquid bridge. Two approaches have been used to achieve this goal. The first approach is using perturbation techniques to investigate the influences of small perturbations to a cylindrical liquid column in the “Plateau-Rayleigh” limit. The “Plateau-Rayleigh” limit is named after Plateau and Rayleigh for their pioneering works in studying the stabilities of liquid jets [35, 36]. Plateau observed that the ratio of the maximum stable length of a cylindrical liquid jet to the jet radius is a constant  $2\pi$  [37] and the theoretical derivation of the observed maximum stable length was given subsequently by Rayleigh using linear stability analysis [36]. Based on the works of Plateau and Rayleigh, the influences of perturbations like small volume changes, disk rotation, and microgravitational effects, have been extensively studied for an axisymmetric liquid bridge supported between two equal disks [38, 39, 40]. Soon after, the influence of unequal disks was examined [41]. The perturbation analyses give intuitions how the bridge stabilities depend on the parameters like volume changes but are invalid for large variations of parameters. In contrast, the second approach based on finding the local energy minimum [42] allows to investigate the stabilities of liquid bridges for a wide range of parameters. With this method, the stable heights of an axisymmetric liquid bridge on equal disks were calculated for volume changes [43]. And the influences of gravity and asymmetric supporting were investigated [44, 45].

### 1.2.3 Dynamic liquid bridge with a fixed contact line

Although the static theory has a good prediction of the onset instability, it can not solve the dynamics of bridge breakup, during which  $\text{Oh} \sim \mathcal{O}(1)$  indicates the viscous stresses become comparable to capillary forces. Using a one-dimensional inviscid slice model, Mesequer first investigated the time variation of liquid-bridge interface and the fluid velocity field inside the liquid bridge [46].

The model is based on the assumption of radial-independent axial flow and therefore the radial momentum equation is decoupled from the governing equations. This manipulation simplifies the model equation and allows for calculations with standard numerical algorithms. However, the model is only applicable to inviscid liquid bridges. Based on the same assumption, another similar one-dimensional model, but derived from slender-jet approximation, was developed by Eggers [47]. Eggers' model is able to handle both viscous and inviscid cases. Consequently, it was applied to the studies of stretching liquid bridges [48, 49]. The representative work by Zhang *et al.* exhaustively investigated the dependence of bridge breakup on the stretching speed and the liquid properties with both experimental and numerical methods [48]. Excellent agreements between experiments and simulations were obtained when comparing the breakup features for moderate stretching speeds. However, discrepancies were observed at higher stretching speeds due to the limitation of the slender-jet approximation. To improve the prediction accuracy, the 2D model equations must be solved. For this purpose, a sophisticated and reliable numerical algorithm was designed based on the finite element method. Subsequently, this numerical algorithm was extended for investigating asymmetric liquid bridge [50] and the effects of surfactants [51, 52]. Most recently, the rapid advances in parallel computing and numerical modeling enable the mesoscopic and microscopic calculations of liquid-bridge rupture. Examples include Monte Carlo simulation based on the lattice gas model [53] and molecular dynamic simulation [54]. The advantage of these particle-based methods is that the pinch-off singularity is removed within the microscopic descriptions and thus it allows the prediction of the dynamic behaviors after ruptures.

#### 1.2.4 Liquid bridge with a moving contact line

Most of the previous theoretical studies of contact drop formation mainly rely on an overly simplified liquid-bridge model in which the wetting phenomenon is not included. This simplification prevents the study of a stretching liquid bridge with a moving contact line on the substrate. The dynamic moving contact line is a commonplace observation in many applications of contact drop dispensing

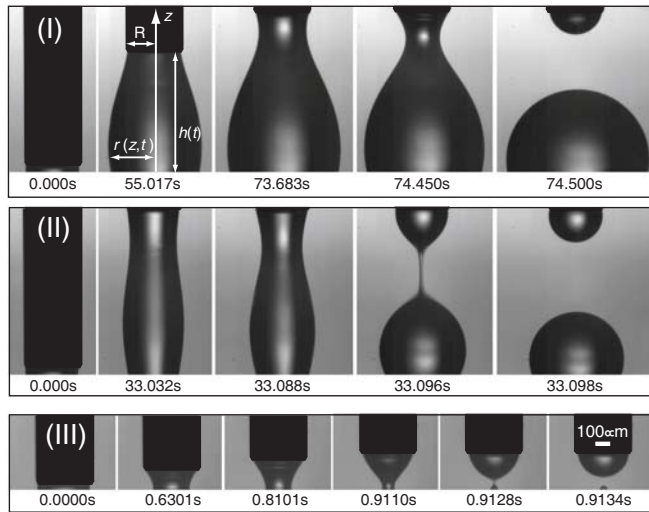


Figure 1.4: Typical sequence of images of drop dispensing at syringe speeds of (I)  $15 \mu\text{m/s}$ , (II)  $35 \mu\text{m/s}$  and (III)  $400 \mu\text{m/s}$ . The syringe radius is  $205 \mu\text{m}$ .

and its motion plays an important role in the dispensing process. Evidence has been provided in a recent experiment in which a quill pin microarraying system was used to print features on a gold-coated glass slide [55]. It showed that a broad range of feature sizes can be printed by varying the substrate wettability while keeping other system parameters the same and the feature sizes increase with the surface wettabilities. Another evidence is given in a simpler table-top experiment [49]. In this experiment, drops were dispensed on a hydrophobic surface via a small size syringe. The syringe was mounted on a motorized microstage to allow for changing the dispensing speed. Experiments showed that by changing the dispensing speed, one can control the contact line motion. At slow retraction speeds, the contact line expands and large droplets can be achieved (Fig. 1.4-I). At moderate needle speeds, a quasi-cylindrical liquid bridge forms resulting in drops approximately the size of the needle (Fig. 1.4-II). Finally, at high speeds, the contact line retracts and droplets much smaller than the syringe diameter are observed (Fig. 1.4-III). Through these means, one can generate a broad range of drop sizes using a single syringe. These observations motivated us to find out what controls the contact line motions and how the contact line movements affect the dispensing

process and the drop size. In Chapter 4, we presented the experimental measurements of the drop sizes and the contact-line movements, identified dispensing regimes, and discussed the dominant mechanisms in different dispensing regimes. Further analyses and discussions of stretching liquid bridge with a “receding” contact line were presented in Chapter 5.

## Chapter 2

# Shape transition and propulsive force of an elastic rod rotating in a viscous fluid

Bian Qian, Thomas R. Powers and Kenneth S. Breuer. *Physical Review Letters*, 100, 078101, 2008.

*The deformation of an elastic rod rotating in a viscous fluid is considered, with applications related to flagellar motility. The rod is tilted relative to the rotation axis and experiments and theory are used to study the shape transition when driven either at constant torque or at constant speed. At low applied torque, the rod bends gently and generates small propulsive force. At a critical torque, the rotation speed increases abruptly and the rod forms a helical shape with increased propulsive force. We find good agreement between theory and experiment. A simple physical model is presented to capture and explain the essential behavior.*

## 2.1 INTRODUCTION

Understanding how flagella and cilia work is a central aim of the field of cell motility. The problem may be split into two parts: the means of actuation, and the fluid-structure interaction. In this article we consider the fluid-structure interaction for thin filaments in a viscous fluid. At micron scales, viscous effects dominate inertia, and the fluid-structure interaction problem simplifies because the Stokes equations governing the fluid motion are linear. Gray and Hancock used this linearity to develop a simple theory that successfully predicted the swimming speed of a sperm cell with a load-independent pattern of bending waves propagating along the flagellum [12]. Soon after, Machin considered the fluid-structure interaction [11]. He argued that the motors must be distributed along the length of the flagellum, since, for small amplitudes, a passive flexible rod waved at one end has an exponentially decaying envelop of deflection, whereas the amplitude of deflection in real flagellar bending waves increases slightly with distance from the head [11]. The shapes and propulsive forces of a passive rod actuated at one end have recently been examined theoretically [13, 14] and experimentally [14]. Although sperm flagella are not passive, the results of [11, 13, 14] are important for modeling real flagella since the modes that Machin found also enter models in which the flagellum is actuated along its entire length [56].

Rotating flagella are also common. For example, nodal cilia [57] have an internal structure similar to that of sperm flagella. However, instead of beating in a plane like most sperm flagella, nodal cilia rotate along the surface of an imaginary cone. The flow set up by these flagella has been implicated in the formation of left-right asymmetry in developing embryos (see [57] and references therein). Bacterial flagella provide another example. These flagella are helical, much thinner than eukaryotic flagella, and driven by a rotary motor embedded in the cell wall. Fluid-structure interactions are important for polymorphic transformations in swimming bacteria [6] and the bundling of multiple flagella [58].

Complementary to the problem of understanding how biological flagella work is the problem of

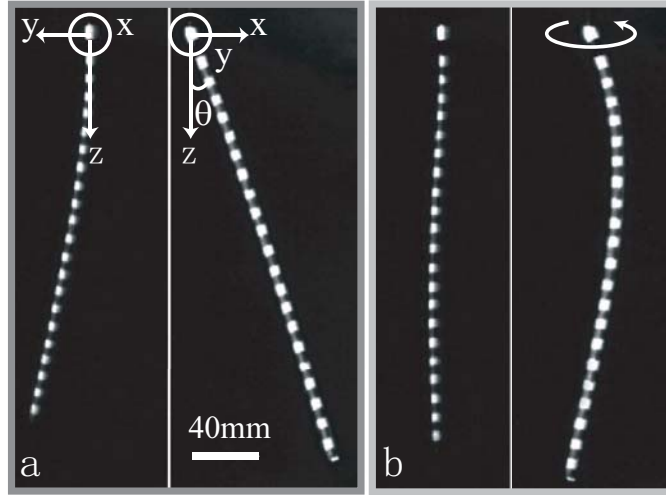


Figure 2.1: Orthogonal images of steady-state shapes of rotating rod with torque just below (a) and just above (b) the critical torque. The motor (not shown) is at the top, with rotation axis along  $z$ . Gravity points down. In (a) and (b), the left panel is the side view, and the right panel is the front view. The rod is marked with white dots for contrast. The axes in (b) are the same as in (a). The curved arrow in (b) denotes the sense of rotation of the rod.

building an artificial microscopic flagellum-propelled swimmer, recently demonstrated by Dreyfus et al. [59], who used a rotating external magnetic field to generate propagating planar bending waves in a filament composed of a string of colloidal magnetic particles. A challenge in building an artificial microscopic swimmer is the means of actuation. Manghi et al. proposed a mechanism in which a microscopic flexible rod rotates along the surface of an imaginary cone [15, 16]. Using numerical methods, they predicted that at a critical driving torque the rod will undergo a discontinuous transition to a helical shape with significant propulsive force, independent of the sense of rotation. In the rest of the manuscript, we present a macroscopic experimental realization of this system, as well as new theoretical results that complement previous hydrodynamic calculations [15, 16]. In addition, we present a simple physical model which captures the essential physics, and helps in the interpretation of the the observed behavior.

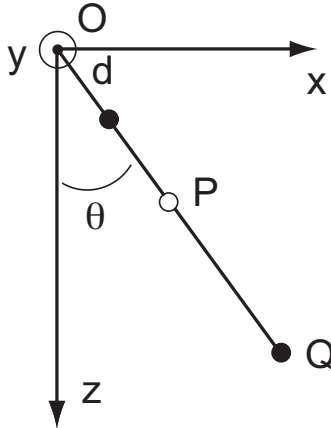


Figure 2.2: Lumped parameter model consisting of two rigid links connected by a torsional spring (open circle). The top link is clamped. All drag is concentrated at the two filled circles.

## 2.2 EXPERIMENT

In our experiment, a servo motor rotates a flexible rod in highly viscous silicone oil. The rod is connected to the motor shaft such that the base of the rod makes a fixed angle with the rotation axis (Fig. 2.1a). The motor may be operated either at constant speed, or at constant torque. The range of torques explored was 0.5 to 8 mN·m, and the maximum rotation frequency was less than 0.3 Hz. The rod is a steel extension spring wrapped in Teflon<sup>TM</sup> tape; the tape stiffens the rod to minimize sagging. The diameter of the rod is  $a = 2.5$  mm, and the bending modulus is  $A \approx 3 \times 10^{-3}$  N·m<sup>2</sup>. Rod lengths  $L$  from 210 mm to 290 mm were tested. The silicone oil has viscosity  $\eta \approx 110$  N·s/m<sup>2</sup> and is held in a tank 420 mm on each side. With these parameters, the Reynolds number  $Re = \rho v L / \eta \approx 10^{-2}$ , where  $\rho \approx 10^3$  kg/m<sup>3</sup> is the fluid density,  $v \approx 10^{-1}$  m/s is the typical velocity of the free end of the rod, and  $L \approx 10^{-1}$  m. Front and side images of the steady-state three-dimensional shape of the rotating rod at each torque were captured using a single camera and a single mirror. The imaging system was carefully calibrated to account for perspective, achieving an accuracy of  $\pm 2$  mm.

At low torque, the rotation speed is relatively slow and the rod bends slightly (Fig. 2.1a). Above

a critical torque, the rod adopts a helical shape and rotates much faster (Fig. 2.1b). To illustrate the physics, we first present a simple analysis of this shape transition using the lumped parameter model shown in Fig. 2.2. The rod is modeled by two rigid links of unit length connected by a torsional spring. The link OP is fixed at angle  $\theta$  between the rotation axis  $\hat{\mathbf{z}}$  and the base of the rod in our experiment. Since the Reynolds number is small, we take  $\text{Re}=0$ . Thus, we may work in the rod's rotating rest frame without introducing fictitious forces. The flow in this frame at point  $\mathbf{r}$  is  $\omega\hat{\mathbf{z}} \times \mathbf{r}$ .

### 2.3 SIMPLE MODEL FOR ROTATING ROD

The torsional spring represents the bending resistance, and is only sensitive to changes in the angle between the vectors OP and PQ. Assuming  $\theta \ll 1$  and  $K$  is sufficiently large, the moment about P on PQ from the spring is  $M_b \approx K(\text{OP} \times \text{PQ}) \approx K(y, 2\theta - x, 0)$ , where  $K$  is the torsional spring constant, and  $(x, y, 2) \approx \mathbf{r}_Q$  is the position of the point Q to leading order in  $\theta$ . To find the steady-state position of Q, equate the moment on PQ due to the torsional spring to the moment on PQ due to the flow. Assuming all drag on PQ is concentrated at Q (Fig. 2.2), the viscous moment about P is  $M_v \approx -\zeta\omega(x, y, 0)$ , where  $\zeta$  is a resistance coefficient. Solving moment balance for  $x$  and  $y$  yields  $x = 2\theta/[1 + (\zeta\omega/K)^2]$  and  $y = x\zeta\omega/K$ . As  $\omega$  increases from zero, the link PQ deflects and  $y$  increases, which causes Q to experience a viscous force in the negative  $x$  direction. These forces push Q toward the rotation axis, and tend to cause the rod in our experiment to wrap around the  $z$  axis. As  $\omega$  increases further, Q moves closer to the rotation axis, and  $y$  begins to decrease. There is also some drag on the link OP, concentrated a distance  $d$  from O. The moment about O due to flow is

$$M_O = \zeta\omega\theta^2 \left( d^2 + \frac{4}{1 + \zeta^2\omega^2/K^2} \right). \quad (2.1)$$

For  $d^2 < 1/2$ , we find that the moment first increases with  $\omega$ , then decreases as the link folds in toward the rotation axis where the flow is slow. The moment then increases again as the drag from

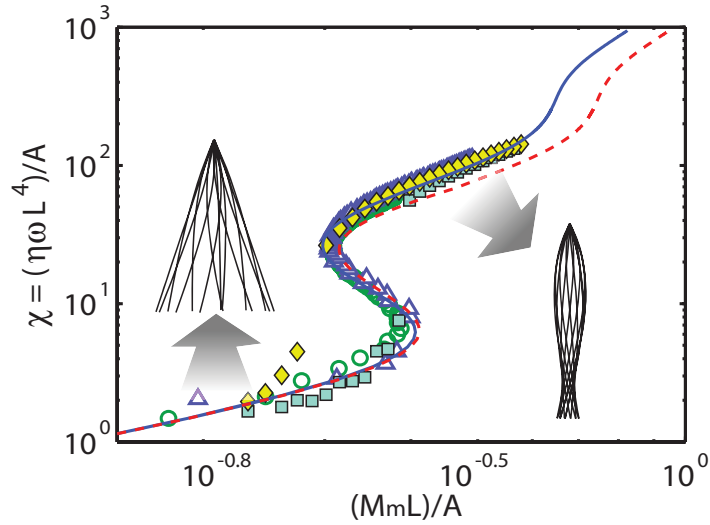


Figure 2.3: Dimensionless motor torque  $M_m L/A$  was measured as a function of dimensionless speed  $\chi$  for  $L = 250$  mm ( $\circ$ ) and  $L = 290$  mm ( $\triangle$ ) with angle  $\theta = 26^\circ$ . For  $L = 250$  mm, speed was measured as a function of increasing torque ( $\blacksquare$ ) and decreasing torque ( $\blacklozenge$ ). Note the hysteresis. The linear (—) and nonlinear (---) predictions are shown. The insets show examples of the steady state filament shapes in the low (left) and high (right) speed regimes.

the base link OP dominates. If  $M_O$  is plotted vs.  $\omega$ , then we find an S-shaped curve, just as in our experiment (Fig. 2.3), with discontinuous transitions in shape and speed as moment varies.

## 2.4 THEORY

### 2.4.1 Theoretical model

We now turn to a more complete quantitative analysis. We will continue to prescribe  $\omega$  rather than motor torque  $M_m$  and we limit the analysis to steady-state shapes. Unlike Manghi et al. [15, 16], we disregard hydrodynamic interactions between distant parts of the rod and use resistive force theory to model the force per unit length  $\mathbf{f}$  acting on the rod [12, 60]:

$$\mathbf{f} = \zeta_{\perp}(\mathbf{v} - \mathbf{r}_s \mathbf{r}_s \cdot \mathbf{v}) + \zeta_{\parallel} \mathbf{r}_s \mathbf{r}_s \cdot \mathbf{v}, \quad (2.2)$$

where  $\zeta_{\perp} = 4\pi\eta/[\log(L/a)+1/2]$  and  $\zeta_{\parallel} = 2\pi\eta/[\log(L/a)-1/2] \approx \zeta_{\perp}/2$ ,  $\mathbf{r}(s, t)$  is the position of the point on the rod centerline with arclength  $s$  at time  $t$ ,  $\mathbf{v}(s, t)$  is the velocity of the undisturbed flow relative to the velocity of the rod at  $s$ , and  $\mathbf{r}_s = \partial\mathbf{r}/\partial s$  is the tangent vector to the rod centerline. There is also a hydrodynamic torque distributed along the rod which induces twist [61, 62, 63]. However, the effects of this torque are smaller by a factor of  $(a/L)^2$  relative to effects due to translation of the rod [61] and will henceforth be disregarded. The constitutive relation for the elastic rod is

$$\mathbf{M} = A\mathbf{r}_s \times \mathbf{r}_{ss}, \quad (2.3)$$

where  $\mathbf{M}$  is the moment due to internal stresses exerted on the cross-section of the rod at  $s$ , and  $A$  is the bending modulus [64]. The shape of the rod is determined by force and moment balance,

$$\mathbf{F}_s + \mathbf{f} + \mathbf{f}_g = \mathbf{0} \quad (2.4)$$

$$\mathbf{M}_s + \mathbf{r}_s \times \mathbf{F} = \mathbf{0}, \quad (2.5)$$

where  $\mathbf{F}$  is the force due to internal stresses acting on the rod cross section at  $s$ ,  $\mathbf{F}_s = \partial\mathbf{F}/\partial s$ , and  $\mathbf{f}_g = (\mu_{\text{rod}} - \pi a^2 \rho_{\text{oil}})g\hat{\mathbf{z}}$  is the buoyancy force per unit length due to the density difference between the rod (linear density  $\mu_{\text{rod}} = 0.0478 \text{ kg/m}$  with oil inside) and silicone oil ( $\rho_{\text{oil}} = 970 \text{ kg/m}^3$ ). The boundary conditions are  $\mathbf{r}(0) = \mathbf{0}$ ,  $\mathbf{r}_s(0) = \hat{\mathbf{x}} \sin \theta + \hat{\mathbf{z}} \cos \theta$ ,  $\mathbf{F}(L) = \mathbf{0}$ , and  $\mathbf{M}(L) = \mathbf{0}$  [64]. As in the lumped parameter model,  $\mathbf{v} = \omega\hat{\mathbf{z}} \times \mathbf{r}$  at steady state in the rod frame.

#### 2.4.2 Dominant dimensionless number

The primary dimensionless groups governing the rod shape are the angle  $\theta$  and the dimensionless rotation speed  $\chi = \eta\omega L^4/A = (L/\ell)^4$ , where  $\ell = [A/(\eta\omega)]^{1/4}$  is the characteristic length scale determined by bending resistance and viscous drag [11, 13]. In addition, the aspect ratio  $L/a$  and the non-dimensional gravitational force  $g\mu_{\text{rod}}L^3/A$  are included in the analysis, but not parametrically

explored since they play a minor role. Figure 2.3 shows that experimental measurements, using two rod lengths, collapse well onto a single curve when dimensionless speed,  $\chi$ , is plotted against dimensionless motor torque,  $M_m L/A$ . The open symbols represent constant velocity rotation and trace out the entire S-shaped curve. The filament shape is stable at every prescribed value of  $\chi$ , and the shape changes continuously from the slightly bent shape to a helical shape as  $\chi$  increases. The closed symbols represent constant torque operation. When driven at constant torque, there is a discontinuity in rotation speed and filament shape at two different torque values, depending if torque is ascending or descending. For descending torque, the time to reach steady state is prohibitively long, and the diamond symbols lying above the curve in Fig. 2.3 represent shapes that are relaxing slowly to steady state.

### 2.4.3 Linear model equation

The nonlinear behavior of the speed-torque curve displayed in Fig 2.3 can be qualitatively explained using linear approximations valid for small rod deflections. For small  $\theta$ , the rod is aligned mainly along the  $z$ -axis and, disregarding gravity, the deflection  $\mathbf{r}_\perp(z) = (x(z), y(z))$  obeys

$$-A \frac{\partial^4 \mathbf{r}_\perp}{\partial z^4} + \zeta_\perp \omega \hat{\mathbf{z}} \times \mathbf{r}_\perp = \mathbf{0}. \quad -\ell^4 \frac{\partial^4 \mathbf{r}_\perp}{\partial z^4} + \hat{\mathbf{z}} \times \mathbf{r}_\perp = \mathbf{0}. \quad (2.6)$$

The solution to Eq. (2.6) is a generalization of Machin's solution to the in-plane bending problem [11], and of the same form as the solution for a flexible rod held parallel to but some distance from the axis of rotation [65].

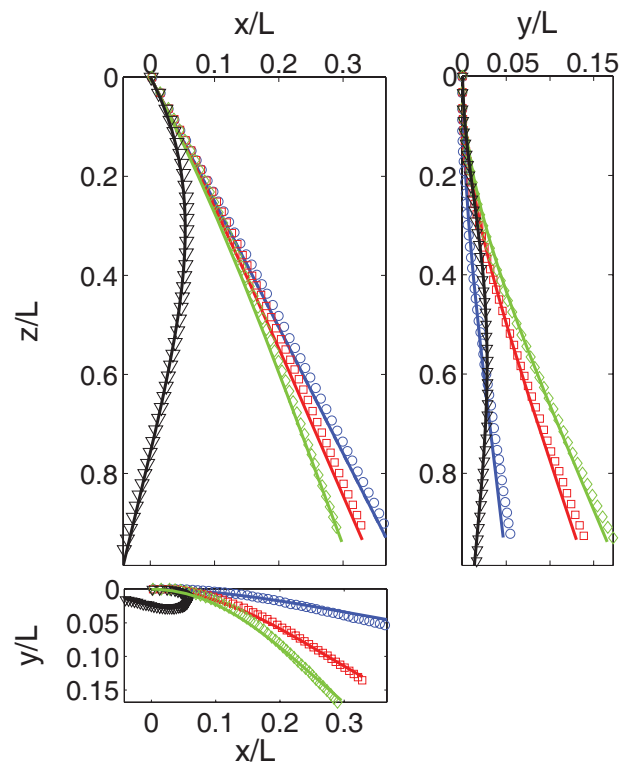


Figure 2.4: (Color online) Steady-state shapes of a rotating rod from experimental measurements for ( $\chi = 1.38$ ) ( $\circ$ ), 4.25 ( $\square$ ), 5.91 ( $\diamond$ ) (before transition), and 164.63 ( $\nabla$ ) (after transition), along with the shapes calculated from the nonlinear (-) theory. The rod has ( $L = 210$ ) mm and ( $\theta = 20^\circ$ ).

## 2.5 RESULTS AND DISCUSSIONS

To calculate the torque  $M_m$  required to rotate the rod at speed  $\omega$ , observe that the moment due to viscous drag must equal the elastic moment at the base of the rod:

$$M_m = -\hat{\mathbf{z}} \cdot \int \mathbf{r} \times \mathbf{f} ds = -A\hat{\mathbf{z}} \cdot \mathbf{r}_s \times \mathbf{r}_{ss}(0). \quad (2.7)$$

The second equality of (2.7) follows from (2.4–2.5). The results of the linear calculation for driving torque vs. speed are shown in Fig. 2.3 along with the experimental data for  $\theta = 26^\circ$ . For small  $\chi$ ,  $M_m$  increases linearly with  $\chi$ . For large  $\chi$ , Eq. (2.6) implies that the shape of the rod is helical with an envelope that decays exponentially with length scale  $\ell$ . Assuming isotropy  $x \sim y$  and using force balance (2.6), the viscous force per length  $f \sim \eta\omega y \sim Ay/\ell^4$ , which implies a total viscous moment  $M_v L/A \sim Ly^2/\ell^3$ . On the other hand, the bending moment at the base of the rod scales as  $M_b L/A \sim yL/\ell^2$ . Equating  $M_v$  and  $M_b$  yields  $y \sim \ell = L\chi^{-1/4}$  [66]. Thus, for  $\chi \gg 1$ , the motor torque must scale as  $M_m L/A \sim \chi^{1/4}$ . Fig. 2.3. Unfortunately, our experiment cannot access this high-speed regime due to limitations in the torque-speed characteristic of our motor. We also observe an intermediate scaling,  $M_m L/A \sim \chi^{1/2}$ . This scaling arises since in this sub-asymptotic regime the deflection  $y \sim L\chi^{-1/4}$ , but the scale for bending of the rod is still  $L$  and not  $\ell$ .

For large  $\theta$ , the deflection of the rod is significant even for small  $\chi$ , and the linear theory is inaccurate. However, the nonlinear equations (2.2–2.5) are readily solved with shooting methods [67]. The nonlinear theory gives a more accurate prediction for the speed-torque relationship in the high-speed regime where the linear and nonlinear theories differ (Fig. 2.3). As  $\theta$  increases, the general appearance of the torque-speed relationship remains unchanged although both the critical torque and the jump in speed at the transition increase (not shown here). Finally, for large  $\chi$ , the linear scaling analysis presented above remains valid, and the moment scales like  $\chi^{1/4}$  for  $\chi \gg 1$ .

Fig 2.4 shows the steady-state rod shapes for four different values of  $\chi$ , comparing experimental data (symbols) with the nonlinear theory (solid line). The agreement between theory and experi-

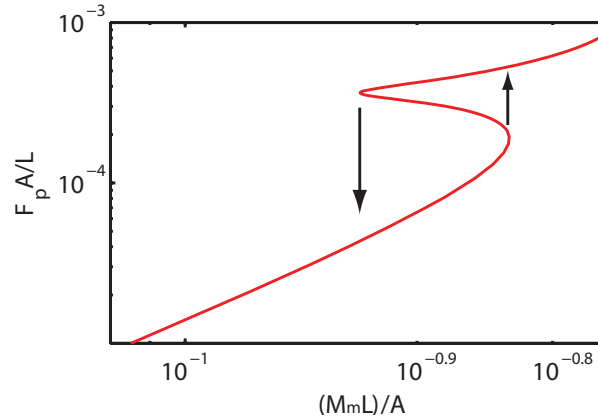


Figure 2.5: Theoretical calculation of the dimensionless propulsion force  $F_p$  as a function of dimensionless  $M_m$  for  $\theta = 20^\circ$ , using the nonlinear equations for the ideal case of zero gravity. The arrows denote the transition for ascending ( $\uparrow$ ) and descending torque ( $\downarrow$ ).

ment is good. Note that the  $y$ - $z$  projection shows how  $y(L)$  first increases with  $\chi$  and then decreases, in accord with our intuitive argument.

We can calculate the thrust, or axial force, from the shape of the rod using  $F_p = \hat{\mathbf{z}} \cdot \int \mathbf{f} ds = -\hat{\mathbf{z}} \cdot \mathbf{F}(0)$ . The kinematic reversibility of Stokes flow implies that a rigid rod rotating along the surface of a cone generates zero propulsive thrust. For small  $\chi$ , the elastic rod deforms slightly and generates little thrust. Above the critical torque, as the helical shape develops, the thrust increases abruptly (Fig. 2.5). Since the shape of an actuated elastic filament cannot be decoupled from swimming kinematics [68], it would be an interesting generalization of our work to build an artificial swimmer driven by a rotating elastic rod, tilted at the base to the rotation axis.

## Chapter 3

# Minimal model for synchronization induced by hydrodynamic interactions

Bian Qian, Hongyuan Jiang, David Gagnon, Kenneth S. Breuer  
and Thomas R. Powers. *Physical Review E*, 80(6), 061919,  
2009.

*Motivated by the observed coordination of nearby beating cilia, we use a scale model experiment to show that hydrodynamic interactions can cause synchronization between rotating paddles driven at constant torque in a very viscous fluid. Synchronization is only observed when the shafts supporting the paddles have some flexibility. The phase difference in the synchronized state depends on the symmetry of the paddles. We use the method of regularized stokeslets to model the paddles and find excellent agreement with the experimental observations. We also use a simple analytic theory based on far-field approximations to derive scaling laws for the synchronization time as a function*

of paddle separation.

### 3.1 INTRODUCTION

One of the central aims in the field of cell motility is to understand how a collection of beating cilia coordinates, or, on a larger scale, how a collection of swimming organisms form coherent patterns. For example, *Paramecium* swims by propagating waves of ciliary beating along its surface [20]. The alga *Chlamydomonas* beats its two flagella in synchrony to swim straight and asynchronously to change its orientation [17, 18]. At the level of a population of cells, sea urchin spermatozoa spontaneously form vortex patterns in the absence of cell signaling [69]. Coordination of cilia is also important in the transport of fluid. The coordination of nodal cilia in developing vertebrate embryos has been implicated in the determination of left-right asymmetry of the organism [22]. The cilia lining the human airway must beat in a coordinated manner to sweep foreign particles up the airway. Beating cilia may also play a role in the transport of sperm and egg during fertilization in mammals [21].

These examples are instances of the general tendency for the emergence of synchronization in a broad array of physical and biological systems [70]. In this article we investigate the long-standing hypothesis that the coordination observed in nearby beating cilia or swimmers is due to hydrodynamic interactions between these objects [71, 72]. In recent years there have been many computational and theoretical studies to support this hypothesis [73, 25, 74, 75, 29, 28, 76, 77, 27, 78]. The key physical fact underlying all of these studies is that at the small scale of the cell, where the Reynolds number  $\text{Re} \ll 1$ , the velocity field arising from a deforming body falls off slowly with distance, leading to significant hydrodynamic forces between nearby bodies. Furthermore, the development of a fixed phase difference between two bodies—phase-locking—requires some kind of compliance in which the deforming body can adjust its beat pattern in response to hydrodynamic forces from other nearby bodies.

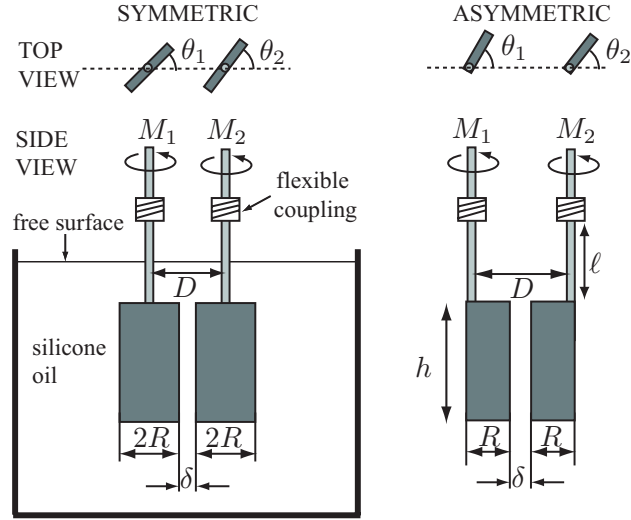


Figure 3.1: Schematic of the model system for hydrodynamic synchronization. Left: A pair of symmetric paddles in a fluid with viscosity  $\eta$  are rotated with constant torques  $M_1$  and  $M_2$ . The shafts are rigid but have flexible couplings that allow the paddles to tilt. Right: asymmetric paddles.

The nature of this compliance is subtle. In the case of two rotating rigid helices driven with fixed torques (the “deformation” here is rotation), the freedom of the phase of each helix to speed up or slow down to maintain the fixed torque for all phase differences does *not* lead to phase-locking [30]. Theoretical calculations suggest that additional degrees of freedom are required for phase-locking, or synchronization. For example, synchronization develops if the shafts of the rotating helices are connected to fixed points by stiff springs, allowing the axes of the helices to translate or tilt [29]. The directions of these small motions depend on whether the hydrodynamic forces are attractive or repulsive, which in turn depends in detail on the phase difference (cf. the case of nearby swimmers [79, 80]).

The complexities of designing experiments that include both hydrodynamic interactions and controlled elastic deformation at very low Reynolds numbers have hindered experimental studies of hydrodynamic synchronization; therefore, we built a scale model system that captures the essential physics, allows for detailed measurements, and is amenable to modeling. This article presents results from experiments (§3.2), numerical simulations (§3.3), and a theoretical model (§3.4 and

§3.5) that together outline a coherent framework for describing hydrodynamic synchronization.

## 3.2 EXPERIMENT

Figure 3.1 illustrates the experimental configuration. Two thin paddles are immersed in a large tank ( $60 \times 60 \times 60$  cm) filled with a viscous fluid ( $\eta = 110 \text{Ns/m}^2$ ), separated at their closest approach by a small gap,  $\delta = 3.6$  mm. We study two different paddle configurations: symmetric and asymmetric. The symmetric paddle has the axis of rotation through the paddle center and dimensions  $h = 60$  mm,  $w = 2R = 30$  mm, and thickness  $t = 6$  mm. The asymmetric paddle has the axis of rotation through one edge and dimensions of  $60 \times 20 \times 6$  mm. The paddles are small compared to the size of the tank. By repeating some of the experiments with the paddles at different positions within the tank, we confirmed that the side walls did not affect the results in any appreciable manner.

The paddles are supported by shafts that are hardened steel, of diameter 6.35 mm and length  $\ell = 120$  mm, connected to the motors via flexible couplings that allow the paddles to tilt. The shafts are so rigid that bending due to hydrodynamic forces is negligible, but the couplings act as torsional springs with spring constant  $k_T = 8000 \text{mN-m/rad}$ , leading to an equivalent spring constant for lateral shifts of the paddles of  $k = k_T/\ell^2$ . This flexibility allows the paddles to tilt slightly in response to hydrodynamic forces. We also tested shafts without an intermediate coupling, in which the ability of the paddles to tilt effectively vanished. The bearing assemblies are supported on separate stages to minimize any mechanical communication beyond hydrodynamic interactions [23], and to allow for precise control of the distance of closest approach,  $\delta$ . Since  $\delta/h \ll 1$ , the resultant flow is mostly two-dimensional, in the plane perpendicular to the axes of rotation.

The two paddles are driven at constant torque using a DC servo motor, digital encoder, load cell, and feedback controller. Each paddle is driven by a servo motor which is encased in a housing.

To measure the torque delivered by the motor, the housing is supported by bearings and prevented from rotating by a rigid,  $\approx 10$  cm-long torque arm. Due to the bearings, the entire reaction torque on the housing is transmitted by the torque arm to a precision load cell. The load cell output signal is used as a feedback to a PID controller that adjusts the voltage driving the servo motor, thus maintaining a defined torque. The PID controller updates at approximately 100 Hz—500 times faster than the typical rotational frequency of the paddles in the experiment (0.2 Hz). The position of the paddle is recorded from the output of the digital encoder at each update of the PID controller. Velocity is calculated from the position using high-order finite differences. The system was calibrated by measuring the rotational speed vs. voltage for an isolated paddle over a range of torques and using the theoretically-known torque-speed relationship to associate the measured load cell voltage with a specific torque. The accuracy and stability of the system was verified by measuring (i) the torque fluctuation for an isolated paddle rotating at constant speed, and (ii) the velocity fluctuation of an isolated paddle rotating at constant torque. In both configurations, we confirmed that the system was stable to better than 1.5% of the set point. Typical driving torques range from 4 mN-m to 25 mN-m, corresponding to rotation frequencies no more than 0.2 Hz.

At these conditions, the Reynolds number,  $\text{Re} = \rho\omega R^2/\eta \approx 10^{-3}$ , is small enough to justify the neglect of inertial forces. This was confirmed experimentally by noting that if the paddle rotation was initiated with a constant velocity, the time taken to reach constant torque was less than 250 ms. For these Stokes flows, the characteristic velocities scale linearly with the motor torques ( $M_1, M_2$ ), and the state of the system is determined by the angles of the two paddles ( $\theta_1, \theta_2$ ) (Fig. 3.1) and the small shifts of the paddles due to the flexible couplers. In the high-stiffness case, the paddles did not synchronize in any measurable time; instead, the phase of each paddle increased roughly linearly with driving torque,  $(\theta_1, \theta_2) \propto (tM_1, tM_2)$ , independent of the initial phase difference (Fig. 3.2a, b). However, paddles with flexible couplers and small distance of closest approach locked phases in 10–20 revolutions (Fig. 3.2c). Note that we measure time in units of  $T_0 = 6\pi\eta R^3/M$ , ( $M$  is the mean torque) which is roughly one tenth of a rotation period. The data we display in this article is

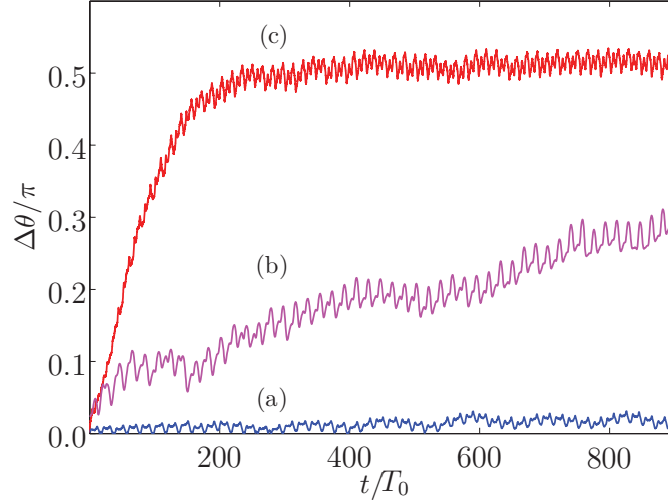


Figure 3.2: Phase difference  $\Delta\theta = \theta_2 - \theta_1$  vs. dimensionless time  $t/T_0$  ( $T_0 = 6\pi\eta R^3/M$ ) for symmetric paddles with (a)  $M_1 = M_2$  and stiff shafts, (b)  $(M_2 - M_1)/M_1 \approx 0.003$  and stiff shafts, and (c)  $M_1 = M_2$  and shafts with flexible couplers.

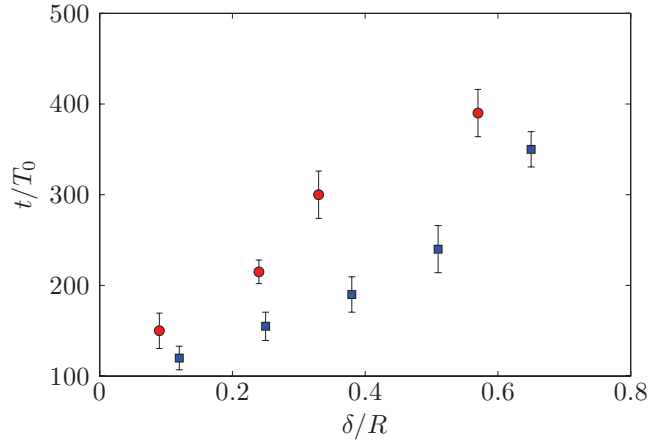


Figure 3.3: Dimensionless synchronization time vs. dimensionless gap size  $\delta/R$  for symmetric paddles (circles) and asymmetric paddles (squares). For symmetric paddles, the dimensionless synchronization time is measured from the moment of phase difference  $\Delta\theta = 0.1$  to the time of the first stable state  $\Delta\theta = \pi/2$ . For asymmetric paddles, the dimensionless synchronization time is defined as the time from  $\Delta\theta = 0.8$  to  $\Delta\theta = 0$ . The uncertainty comes from the low frequency fluctuation in  $\Delta\theta$  due to the system noise. Time is normalized by  $T_0 = 6\pi\eta R^3/M$ .

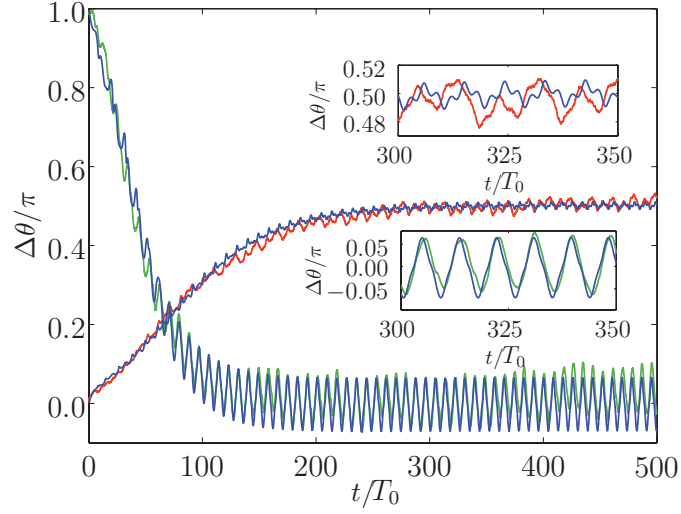


Figure 3.4: Phase difference vs. dimensionless time for symmetric (red line) and asymmetric paddles (green line), compared to simulation (blue lines). Time is measured in units of  $T_0 = 6\pi\eta R^3/M$ . The insets show the phase difference once phase-locking is achieved. In both cases, the normalized gap between the paddles is  $\delta/R = 0.24$ .

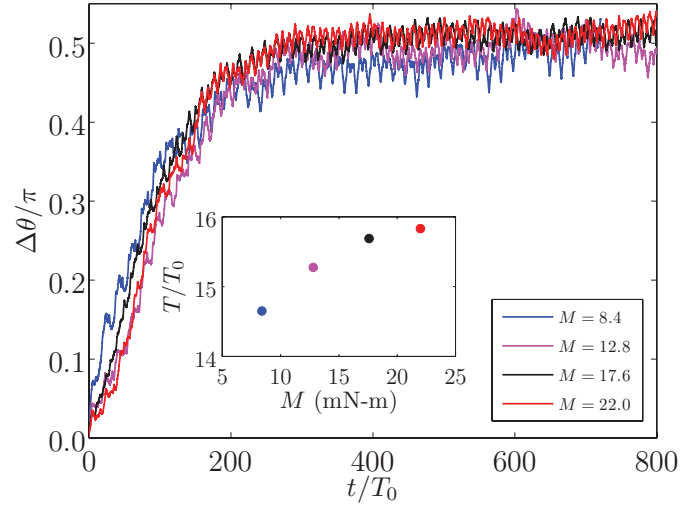


Figure 3.5: Phase difference vs. dimensionless time  $t/T_0$  for symmetric paddles driven at torques  $M_1 = M_2 = 8.4, 12.8, 17.5,$  and  $22$  mN-m, with  $\delta/R = 0.24$ . The collapse of the data shows that the time to synchronize scales with  $T_0 = 6\pi\eta R^3/M$ . The inset shows the dimensionless period  $T/T_0$  in the synchronized state.

for a dimensionless gap size  $\delta/R = 0.24$ . We also varied  $\delta/R$  for both kinds of paddles from  $\approx 0.1$  to  $\approx 0.6$ , and found that the time to synchronize increased with spacing, with longer times and a faster increase for the symmetric paddles (Fig. 3.3).

For  $M_1 = M_2$ , the symmetric paddles locked phases at  $\Delta\theta \equiv \theta_2 - \theta_1 = \pi/2$ , and the asymmetric paddles settled at  $\Delta\theta = 0$  (Fig. 3.4). These two states represent the conditions that roughly maximize the distance of closest approach of the two paddles. Since the paddles would minimize their distance of closest approach if they maintained their typical initial phase differences ( $\Delta\theta = 0$  for the symmetric paddles,  $\Delta\theta = \pi$  for the asymmetric paddles), the rotation speed of each paddle rises as the paddles synchronize. Denoting the rotation speed of an isolated paddle by  $\omega_0$ , we found that the speed of both symmetric paddles rises from  $0.72\omega_0$  to  $0.85\omega_0$  as synchronization develops, whereas the speed of both asymmetric paddles rises from  $0.75\omega_0$  to  $0.93\omega_0$ . While these synchronized states are stable, there is a consistent and repeatable phase fluctuation (Fig. 3.4-inset) corresponding to the variation in rotational speeds as the hydrodynamic interactions between the paddles wax and wane during a cycle. The fluctuation amplitude in the asymmetric case is larger than in the symmetric case because there is a larger variation in the distance between the asymmetric paddles during a period. These observations qualitatively agree with the results of numerical calculations on rotating rigid helices with flexible couplers [29]. In our experiments the phase fluctuations and rise in velocity as synchronization develops are more dramatic since the variation in the hydrodynamic interaction between paddles over a period is greater than in the case of helices.

The final state of synchronization was found to be independent of the initial orientation of the paddles. The time to synchronize scales with  $T_0$ , perhaps with a weak dependence on torque (Fig. 3.5). The number of paddle revolutions needed to synchronize is therefore roughly constant, 15 in the case of symmetric paddles, and 20 for asymmetric paddles. In the synchronized state, however, the dimensionless rotation period  $T/T_0$  increases slightly with torque (Fig. 3.5, inset). When the symmetric paddles are operated with a torque mismatch between the two motors, the

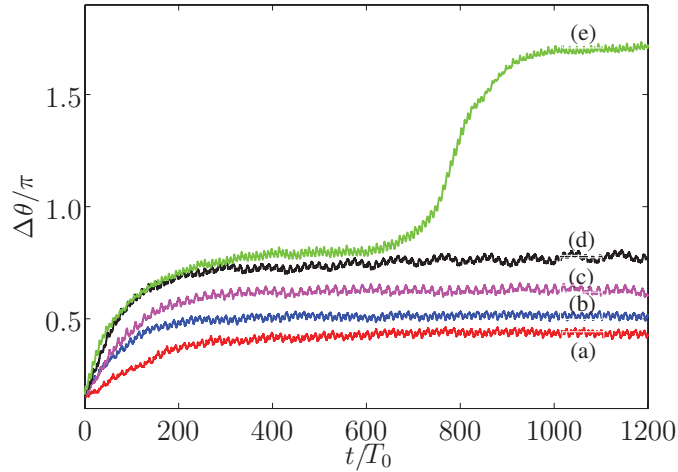


Figure 3.6: Phase difference vs. dimensionless time for symmetric paddles with  $\delta/R = 0.24$  and  $\Delta M/M_1 = (M_2 - M_1)/M_1 = -1\%$  (a),  $\Delta M/M_1 = 0\%$  (b),  $\Delta M/M_1 = 1\%$  (c), and  $\Delta M/M_1 = 2\%$  (d). When  $\Delta M/M_1 \approx 3\%$ , the synchronized states become unstable, and the system exhibits transition in which  $\Delta\theta$  jumps by  $\pi$ .

synchronized phase difference increases with  $\Delta M$ , although for a large mismatch,  $\Delta M/M_1 = 3\%$ , the synchronized state is only marginally stable and the phase difference can jump abruptly by  $\Delta\theta = \pi$  (Fig. 3.6).

### 3.3 NUMERICAL CALCULATION

These experiments give strong evidence that the phase-locking of the paddles is due to hydrodynamic interactions. We tested this hypothesis by using the method of regularized Stokeslets [81] to model the flows induced by the paddles. Each paddle is replaced by a rectangular array of regularized Stokeslets  $S_{\mu\nu}^b$  with strength  $f_\nu$ , where  $\mu$  and  $\nu$  label the Cartesian coordinates  $x$ ,  $y$ , and  $z$ . The flow from the Stokeslet at  $\mathbf{x}'$  is given by

$$v_\mu(\mathbf{x}) = \sum_\nu S_{\mu\nu}^b(\mathbf{x}, \mathbf{x}') f_\nu, \quad (3.1)$$

with associated pressure

$$p(\mathbf{x}) = \sum_{\nu} \frac{p_{\nu}^b(\mathbf{x}, \mathbf{x}') f_{\nu}}{8\pi}. \quad (3.2)$$

The Stokeslet  $S_{\mu\nu}^b$  satisfies

$$\sum_{\nu} \partial S_{\mu\nu}^b / \partial x_{\nu} = 0 \quad (3.3)$$

$$\nabla^2 S_{\mu\nu}^b(\mathbf{x}, \mathbf{x}') - \partial p_{\nu}^b / \partial x_{\mu} = -8\pi \delta_{\mu\nu} \phi_b(\mathbf{x} - \mathbf{x}'), \quad (3.4)$$

where  $\phi_b(\mathbf{x} - \mathbf{x}')$  is a smooth approximation to the Dirac delta function with spread  $b$ ,

$$\phi_b(\mathbf{x} - \mathbf{x}') = \frac{15b^4}{8\pi (r^2 + \epsilon^2)^{7/2}}, \quad (3.5)$$

and  $r = |\mathbf{x} - \mathbf{x}'|$ . The number of stokeslets and the spread  $b$  are chosen to give good agreement between the measured and simulated resistance coefficient for a single rotating paddle at the center of the tank. The spread  $b$  is large enough to make the regularized stokeslets overlap, which prevents fluid from leaking through the paddles. We model the flexibility of the couplers with springs of torsional spring constant  $k_T$ . For simplicity we suppose that the shafts are always vertical, but can undergo slight shifts in the horizontal plane. With the assumption that the paddles are rigid, the degrees of freedom are the angles  $(\theta_1, \theta_2)$  of the paddles and the positions of the shafts. Balancing forces and torques leads to coupled nonlinear differential equations which we solve numerically. Figure 3.4 shows the excellent agreement between the experiments and the simulations for both the asymmetric and the symmetric paddles. The simulation accurately captures the frequency and amplitude of the oscillations associated with the rotation of the motors, as well as the slower evolution of the phase-locking. When the driving torque is varied over the range used in the experiment, the simulations yield that the dimensionless time to synchronize  $T_s/T_0$  remains approximately constant, with a weak dependence on torque, in accord with Fig. 3.5. Simulations with infinite spring constant  $k_T$  show no phase-locking. Since the paddles in the simulation are

coupled only through the hydrodynamic interaction, we conclude that the cause of the phase-locking is the hydrodynamic interaction and not any stray mechanical coupling that might be present in the experimental apparatus.

## 3.4 SIMPLE MODEL FOR ASYMMETRIC PADDLES

### 3.4.1 Oseen tensor model

We can gain more insight into the mechanism of phase-locking by developing a simple theory along the lines of reference [27]. A minimal model for the asymmetric paddles is to replace each paddle with a sphere of radius  $a$  attached to one end of a rod of length  $R$  (Fig. 3.7). The rod is rigid and does not disturb the fluid. The other end of the rod is attached to a stationary point by a spring with spring constant  $k$ . The rods are rotated by moments  $M_1$  and  $M_2$  which are applied at the ends of the rods attached to the springs, where we can imagine shafts perpendicular to the plane of the page. The spring is stiff, with  $k \gg M_1/R^2$ . Denote the positions of the balls by  $\mathbf{r}_i = \mp(D/2)\hat{\mathbf{x}} + \mathbf{x}_i + R\hat{\boldsymbol{\rho}}_i$ , where the minus sign applies for  $i = 1$ , the plus sign applies for  $i = 2$ , and  $\hat{\boldsymbol{\rho}}_i = (\cos \theta_i, \sin \theta_i)$ . Note that  $\theta_i$  is defined as the angle the rod makes with the  $x$ -axis, not the angle  $\mathbf{r}_i$  makes with the  $x$ -axis. The vectors  $\mathbf{x}_1 = (x_1, y_1)$  and  $\mathbf{x}_2 = (x_2, y_2)$  are the displacements of the shafts from the stationary points  $(-D/2, 0)$  and  $(D/2, 0)$ , respectively. If we suppose the balls are far apart, with  $D \gg a$ , then the leading-order interaction between the two balls is given by the Oseen tensor [82]:

$$\mathbf{v}_1 = \frac{\mathbf{f}_1}{6\pi\eta a} + \frac{1}{8\pi\eta} \left[ \frac{\mathbf{f}_2}{|\mathbf{r}_{12}|} + \frac{(\mathbf{f}_2 \cdot \mathbf{r}_{12})\mathbf{r}_{12}}{|\mathbf{r}_{12}|^3} \right] \quad (3.6)$$

$$\mathbf{v}_2 = \frac{\mathbf{f}_2}{6\pi\eta a} + \frac{1}{8\pi\eta} \left[ \frac{\mathbf{f}_1}{|\mathbf{r}_{12}|} + \frac{(\mathbf{f}_1 \cdot \mathbf{r}_{12})\mathbf{r}_{12}}{|\mathbf{r}_{12}|^3} \right], \quad (3.7)$$

where  $\mathbf{v}_i = d\mathbf{r}_i/dt = \dot{\mathbf{r}}_i$  is the velocity of the  $i$ th ball,  $\mathbf{f}_1$  and  $\mathbf{f}_2$  are the forces exerted by the balls on the fluid, and  $\mathbf{r}_{12} = \mathbf{r}_1 - \mathbf{r}_2$ .

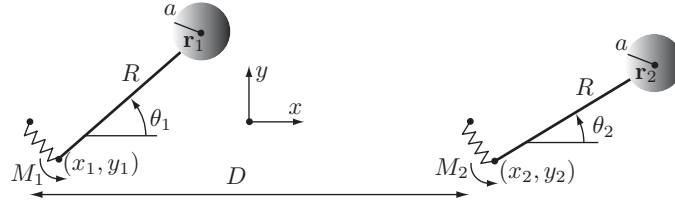


Figure 3.7: Model for asymmetric paddles. The figure is not to scale; note that  $a \ll R \ll D$ .

Since the spring is assumed linear and the motion of the rod incurs no drag force, the balance of forces on each paddle is  $-\mathbf{f}_i - k\mathbf{x}_i = \mathbf{0}$ . We must also enforce moment balance. Since inertia is unimportant at  $\text{Re} = 0$ , we may compute moments about the points  $\mathbf{x}_i$  for each paddle:

$$M_i + \hat{\mathbf{z}} \cdot (R\hat{\boldsymbol{\rho}}_i) \times (-\mathbf{f}_i) = 0. \quad (3.8)$$

### 3.4.2 Separation of time scales

The analysis of the equations of motion is simplified by the recognition that our problem has three well-separated time scales: (i) a short time scale  $T_k = \eta a/k$  (recall  $k = k_T/\ell^2$ ) that controls the rate of relaxation of the springs, (ii) an intermediate time scale  $T_1 = 6\pi\eta a R^2/M_1$ <sup>1</sup> that controls the period of an isolated ball driven by torque  $M_1$ , and (iii) a long time scale  $T_s$  that characterizes the time for phase-locking to develop. Since the springs are stiff,  $T_k \ll T_1$ . Since the interaction between the paddles is weak,  $T_1 \ll T_s$ . The goal of the simple model is to give a clear derivation of how  $T_s$  depends on the parameters of the problem. Since the phase-locking arises from hydrodynamic interactions, which vanish when  $a/D \rightarrow 0$ , we expect  $T_s$  to scale as some power of  $D/a$  for large  $D/a$ .

<sup>1</sup>Note that the period of an isolated paddle of width  $R$  (as in Fig. 3.1) scales as  $T_0 = 6\pi\eta R^3/M_1$ , whereas  $T_1 = 6\pi\eta a R^2/M_1$  is a more appropriate scale for the period of a ball of radius  $a$  moving on an orbit of approximate radius  $R$  and driven by torque  $M_1$ .

### 3.4.3 Dimensionless far-field equations of motion for $\theta_i$ and $\mathbf{x}_i$

Since the balls are far apart, we expand the equations of motion in powers of  $1/D$ , assuming that  $a \ll D$  and  $R \ll D$ . Measuring length in units of  $R$ , time in units of  $T_1$ , and using force balance to eliminate  $\mathbf{f}_i$  leads to the dimensionless equations of motion,

$$(\dot{\mathbf{X}} + \dot{\Theta}) = -\mathbf{H}\mathbf{X}/\epsilon. \quad (3.9)$$

In Eq. (3.9),  $\epsilon = M_1/(kR^2) \ll 1$ ,  $\mathbf{X}$  and  $\dot{\Theta}$  are  $4 \times 1$  vectors with

$$\mathbf{X} = \begin{pmatrix} \mathbf{x}_1 \\ \mathbf{x}_2 \end{pmatrix}, \quad \dot{\Theta} = \begin{pmatrix} \dot{\theta}_1 \hat{\theta}_1 \\ \dot{\theta}_2 \hat{\theta}_2 \end{pmatrix}, \quad (3.10)$$

where  $\hat{\theta}_i = (-\sin \theta_i, \cos \theta_i)$ . The  $4 \times 4$  matrix  $\mathbf{H}$  is the Oseen tensor to leading order in  $a/D$ ,

$$\mathbf{H} = \begin{bmatrix} \mathbf{I} & \frac{3}{4} \frac{a}{D} (1 + \hat{\mathbf{x}}\hat{\mathbf{x}}) \\ \frac{3}{4} \frac{a}{D} (1 + \hat{\mathbf{x}}\hat{\mathbf{x}}) & \mathbf{I} \end{bmatrix}, \quad (3.11)$$

where  $\mathbf{I}$  is the  $2 \times 2$  identity matrix and  $\hat{\mathbf{x}}\hat{\mathbf{x}}$  is the  $2 \times 2$  matrix with unity in the upper left-hand corner and zeros elsewhere.

Using  $M_1$  as the unit for torque, the moment balance equations (3.8) take the form

$$1 + (\mathbf{x}_1/\epsilon) \cdot \hat{\theta}_1 = 0 \quad (3.12)$$

$$1 + \frac{\Delta M}{M_1} + (\mathbf{x}_2/\epsilon) \cdot \hat{\theta}_2 = 0, \quad (3.13)$$

where  $\Delta M = M_2 - M_1$ . From these equations we conclude that  $\mathbf{x}_i$  is  $\mathcal{O}(\epsilon)$ . Note that the shafts have a nonzero displacement  $\mathbf{x}_i$  even when the paddles are isolated.

### 3.4.4 Far-field equations of motion for average angular speed and phase difference

To understand phase-locking, it is not necessary to resolve the motion of the paddles on the short time scale  $T_k$ . In dimensionless variables, these short-scale motions are characterized by transients of the form  $\exp(-t/\epsilon)$ . By considering dimensionless times  $t \gg \epsilon$  we may neglect these transients and treat  $\epsilon \dot{\mathbf{X}}$  as small. Physically, this approximation reflects the fact that once the transients have decayed, the drag forces incurred by the small motions  $\mathbf{X}$  arising from the extension of the springs are small, but not negligible, compared to the drag forces due to the rotation  $\dot{\Theta}$  of the balls about the shafts. Therefore, we solve Eq. (3.9) for  $\mathbf{X}$  using iteration, finding

$$\mathbf{X} \approx -\epsilon \mathbf{H}^{-1} \dot{\Theta} + \epsilon^2 \mathbf{H}^{-1} \frac{d}{dt} \left( \mathbf{H}^{-1} \dot{\Theta} \right). \quad (3.14)$$

In terms of  $\theta_i$ , we have

$$\mathbf{X} \approx \epsilon \begin{pmatrix} -\dot{\theta}_1 \hat{\theta}_1 + \frac{3}{2} \frac{a}{D} \dot{\theta}_2 \hat{\theta}_2 \\ -\dot{\theta}_2 \hat{\theta}_2 + \frac{3}{2} \frac{a}{D} \dot{\theta}_1 \hat{\theta}_1 \end{pmatrix} + \epsilon^2 \begin{pmatrix} -\dot{\theta}_1^2 \hat{\rho}_1 + \frac{3}{2} \frac{a}{D} \dot{\theta}_2^2 \hat{\rho}_2 \\ -\dot{\theta}_2^2 \hat{\rho}_2 + \frac{3}{2} \frac{a}{D} \dot{\theta}_1^2 \hat{\rho}_1 \end{pmatrix}, \quad (3.15)$$

where we have only retained terms of  $\mathcal{O}(a/D)$ .

In Eq. (3.15), we have discarded terms of the form  $\ddot{\theta}_i$ , since they are  $\mathcal{O}(a^2/D^2)$ . To see why, observe that for time scales longer than  $T_k$ , the motion is characterized by two well-separated time scales,  $T_1$  and  $T_s$ . The form of the interaction suggests that  $T_s \propto D/a$ . To explicitly account for the multiple scales  $T_1$  and  $T_s$ , write [83]

$$\theta_{1,2} = \omega(\tau)t \mp \Delta\theta(\tau)/2, \quad (3.16)$$

where  $\tau = at/D$  describes the slowly-varying time dependence of the rotational frequency and the phase difference. Note that  $\omega(\tau)$  is the average angular speed, and  $\Delta\theta$  is the average phase differ-

ence. The angular speed and phase difference also have rapidly vary parts with zero average, but these are lower order in  $a/D$  [83]. Equation (3.16) shows that the leading term of  $\ddot{\theta}_i$  is  $(a/D)\omega'(\tau)$ . But since the average rotation speed  $\omega$  is constant in the absence of interactions,  $\omega'(\tau)$  must be at least  $\mathcal{O}(a/D)$ . Thus,  $\ddot{\theta}_i$  is at least  $\mathcal{O}(a^2/D^2)$ .

To find the governing equations for angular speed  $\omega$  and phase difference  $\Delta\theta$ , substitute the shaft displacements  $\mathbf{x}_i$  from Eq. (3.15) into moment balance, Eqs. (3.12–3.13). Finally, average the resulting equations over a period, treating the slowly-varying variables  $\omega$  and  $\Delta\theta$  as constants under the average. We find that the average dimensionless speed is given by

$$\omega = 1 + \frac{\Delta M}{M_1} + \frac{9}{8} \frac{a}{D} \cos \Delta\theta. \quad (3.17)$$

The interacting paddles turn faster than they would in isolation. This result is in contrast with our paddle experiments, where we saw in §3.2 that the asymmetric paddles rotated more slowly compared to an isolated paddle. It is too much to demand that our far-field theory captures every aspect of the paddle experiments, since the paddles are close to each other in the experiment and the theory is valid when they are far apart.

The dimensionless phase difference obeys

$$\frac{d\Delta\theta}{dt} = -\frac{9}{2} \epsilon \frac{a}{D} \sin \Delta\theta + \frac{\Delta M}{M_1}. \quad (3.18)$$

These results (3.17–3.18) are equivalent to the results of reference [27]. For equal driving torques,  $\Delta M = 0$ , Eq. (3.18) shows that the paddles synchronize to  $\Delta\theta = 0$ , independent of the initial value of  $\Delta\theta$ , in (dimensional) time  $T_s \sim (D/a)(kR^2/M_1)T_1$ , or

$$T_s \sim \frac{D}{a} \frac{kR^2}{M_1} \frac{6\pi\eta a R^2}{M_1}. \quad (3.19)$$

When  $M_1 \neq M_2$ , the paddles phase-lock with a nonzero phase difference, which increases to  $\pi/2$

in the steady state as the torque difference increases to the critical value given by  $\Delta M/M_1 = (9/4)(a/D)M_1/(kR^2)$ . Note that the factor of  $a/D$  and the smallness of  $\epsilon = M_1/(kR^2)$  mean that  $M_2$  must be very close to  $M_1$  for the phase difference  $\Delta\theta$  to have a fixed point. Thus, in the derivation of Eqs. (3.17–3.18) we considered  $\Delta M/M_1$  and  $T_1\Delta\dot{\theta}$  to be  $\mathcal{O}(\epsilon a/D)$ .

This simple theory predicts that  $T_s/T_1$  varies inversely with torque, whereas the experiments show that  $T_s/T_1$  depends at most weakly on torque (Fig. 3.5). Again, the resolution of this discrepancy is that the simple theory is valid in the far-field limit with  $D \gg a$ , whereas the experiments are carried out in the near-field regime where  $T_s/T_1$  is independent of torque.

### 3.4.5 Physical explanation for phase locking

Each of the terms of Eq. (3.15) has a simple interpretation. First consider the limit of an isolated paddle,  $a/D = 0$ . To leading order in  $\epsilon$ , the ball on the end of the rod undergoes circular motion. This motion leads to a drag in the  $-\hat{\theta}_i$  direction, which stretches the spring along  $-\hat{\theta}_i$ , which in turn leads to an  $\mathcal{O}(\epsilon)$  component of the ball's velocity parallel to the rod, along the  $\hat{\rho}_i$  direction (see the left ball in Fig. 3.8a). In our dimensionless units, the ball exerts an  $\mathcal{O}(1)$  force on the liquid in the  $\hat{\theta}_i$  direction, and an  $\mathcal{O}(\epsilon)$  force on the liquid in the  $\hat{\rho}_i$  direction. To get the displacement  $\mathbf{X}$ , we multiply these forces by  $\epsilon$ , and thus get the  $\mathcal{O}[(a/D)^0]$  terms of Eq. (3.15). Now consider the hydrodynamic interactions. For a given paddle, each of the forces just described induces a Stokeslet flow, falling off inversely with distance, and leading to the  $\mathcal{O}(a/D)$  terms in Eq. (3.15).

The drag forces on each paddle induced by the motion of the other are shown in Fig. 3.8. From this figure we can see why the paddles synchronize. Suppose that the second paddle slightly lags the first. Since the spring is flexible, the ball of the paddle on the left has a velocity component of  $\epsilon\dot{\theta}_1$  along the rod as well as the component  $\dot{\theta}_1$  perpendicular to the rod (blue arrows, Fig. 3.8a, left). This motion induces drag forces on the ball on the right (red dotted arrows, Fig. 3.8a, right), which in our dimensionless units are down by a factor of  $a/D$  from the velocities. The components of these forces perpendicular to the rod (green arrows, Fig. 3.8a, right) contribute to the hydrodynamic

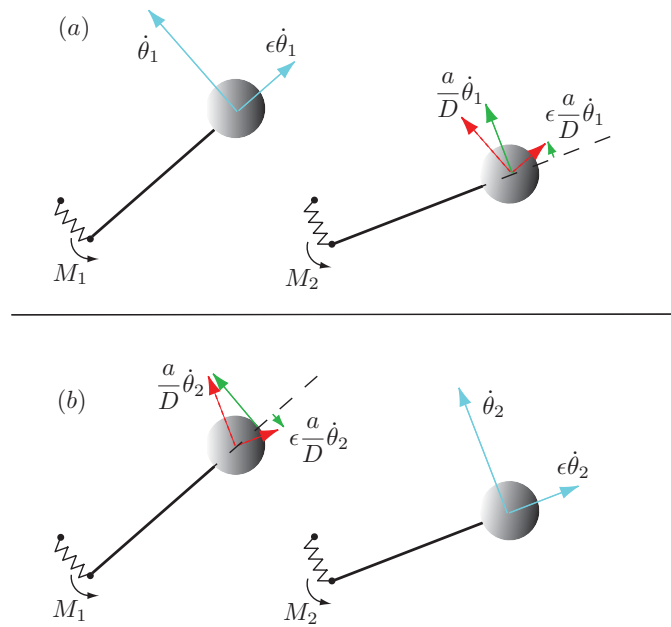


Figure 3.8: Physical explanation for synchronization. The figure is not to scale and the paddles have been moved artificially close. (a) On the left we show the components of velocity of the first ball (blue arrows). On the right, we show the components of the drag induced on the second ball by the motion of the first ball (red dotted arrows), and the components that contribute to the hydrodynamic torque on the second paddle (green arrows). (b) The same situation as (a), but showing the velocity components of the second ball and the induced forces on the first. The difference in the hydrodynamic torques tends to make  $\Delta\theta = 0$ .

torque on the paddle. Likewise the motion of the paddle on the right (blue arrows, Fig. 3.8b, left) induces forces that lead to hydrodynamic torques on the left paddle. The phase difference  $\Delta\theta$  is governed by the difference of the torques, which for small  $\Delta\theta$  is given by the difference of the small (green) arrows in Figs. 3.8a and b. The torque difference makes  $\Delta\theta = 0$  a stable fixed point (for  $\Delta M = 0$ ).

### 3.4.6 Power dissipation

We may readily examine the question of power dissipation using our simple model. First note that for fixed driving torques, the power dissipated decreases when the hydrodynamic resistance of the paddles increases. Therefore, when  $\Delta\theta = 0$ , the drag is minimized and the dissipation rate is maximized. As  $\Delta M$  increases, the increase in  $\Delta\theta$  leads to greater resistance and therefore lower dissipation rate. To leading order in  $\epsilon$ , we may use Eq. (3.17) to show that the dimensionless power averaged over one period,  $P = M_1\dot{\theta}_1 + M_2\dot{\theta}_2$ , takes the form

$$\frac{P}{M_1} = 2 + \frac{9}{4} \frac{a}{D} \cos \Delta\theta. \quad (3.20)$$

In general, the phase difference chosen by the system does not minimize the power dissipated. The same conclusion has been reached for the hydrodynamic phase-locking of nearby swimming sheets [78].

## 3.5 SIMPLE MODEL FOR SYMMETRIC PADDLES

### 3.5.1 Oseen model and nondimensionalization

To understand why the symmetric paddles lock phases with  $\Delta\theta = \pi/2$  when  $\Delta M = 0$ , we model the paddles as dumbbells (Fig. 3.9). Each dumbbell consists of two balls connected by a rod that does not disturb the fluid as it moves. The midpoint of each rod is attached to a fixed point by a stiff

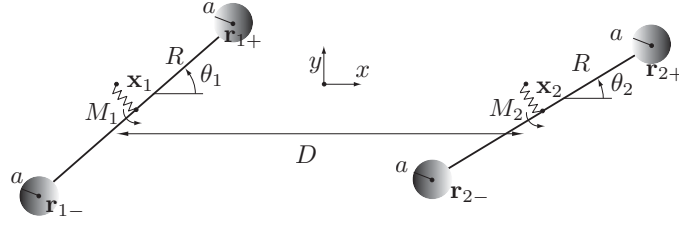


Figure 3.9: Model for symmetric paddles. The figure is not to scale; note that  $a \ll R \ll D$ .

spring, and the balls at the ends of the rods have positions

$$\mathbf{r}_{1\pm} = -(D/2)\hat{\mathbf{x}} + \mathbf{x}_1 \pm R\hat{\boldsymbol{\rho}}_1 \quad (3.21)$$

$$\mathbf{r}_{2\pm} = (D/2)\hat{\mathbf{x}} + \mathbf{x}_2 \pm R\hat{\boldsymbol{\rho}}_2, \quad (3.22)$$

where  $\mathbf{x}_i$  is the displacement of the midpoint of the  $i$ th rod from the corresponding fixed point. Denoting by  $\mathbf{f}_{i\pm}$  the forces that the balls on the  $i$ th dumbbell exert on the fluid, the balance of forces on each dumbbell implies

$$-\mathbf{f}_{i+} - \mathbf{f}_{i-} - k\mathbf{x}_i = \mathbf{0}, \quad (3.23)$$

and the balance of torques implies

$$M_i + \hat{\mathbf{z}} \cdot (R\hat{\boldsymbol{\rho}}_i) \times (-\mathbf{f}_{i+}) + \hat{\mathbf{z}} \cdot (-R\hat{\boldsymbol{\rho}}_i) \times (-\mathbf{f}_{i-}) = 0. \quad (3.24)$$

Assuming all balls are far apart, we again use the Oseen model, Eq. (3.7), this time extended to the four balls labeled  $\alpha = 1-, 1+, 2-, 2+$ :

$$\mathbf{v}_\alpha = \frac{\mathbf{f}_\alpha}{6\pi\eta a} + \frac{1}{8\pi\eta} \sum_{\beta \neq \alpha} \left[ \frac{\mathbf{f}_\beta}{|\mathbf{r}_{\alpha\beta}|} + \frac{(\mathbf{f}_\beta \cdot \mathbf{r}_{\alpha\beta})\mathbf{r}_{\alpha\beta}}{|\mathbf{r}_{\alpha\beta}|^3} \right], \quad (3.25)$$

where  $\mathbf{r}_{\alpha\beta} = \mathbf{r}_\alpha - \mathbf{r}_\beta$ . This is valid when  $R \gg a$  and  $D \gg a$ , but we will also assume  $D \gg R$ .

The  $\theta_i \mapsto \theta_i + \pi$  symmetry of the dumbbells makes the hydrodynamic interaction between the

dumbbells more subtle than the asymmetric case. First observe that the spring of an isolated rotating dumbbell does not stretch since the net hydrodynamic force on the balls vanishes. Thus,  $\mathbf{x}_i = \mathbf{0}$  when  $D \rightarrow \infty$ . However, for finite  $D/R$ , the flow induced by the rotation of one dumbbell causes the spring of the other dumbbell to stretch. To estimate the amount of stretch, consider the flow induced by dumbbell 1 at dumbbell 2. The far-field flow is an asymmetric force dipole, also known as a rotlet, falling off inversely with the square of distance [84]. Thus, the flow  $v_{21}$  induced at dumbbell 2 is approximately  $v_{21} \sim f_1 R / (\eta D^2)$ , leading to drag on dumbbell 2 of about  $\eta a v_{21} \sim a f_1 R / D^2 \sim a M_1 / D^2$ . This drag causes the spring of dumbell to stretch, with a displacement

$$\frac{|\mathbf{x}_2|}{R} \sim \frac{a}{R} \frac{R^2}{D^2} \frac{M_1}{k R^2}. \quad (3.26)$$

As in the previous section, it is convenient to measure length in units of  $R$  and time in units of  $T_1 = 6\pi\eta R^2 a / M_1$ . Thus, the dimensionless displacement is  $|x_2| \sim \epsilon a / D^2$ .

### 3.5.2 Far-field equations of motion

For each spring of a pair of rotating dumbbells, the leading order stretch of the spring is second order in  $D^{-1}$ . However, to derive equations describing phase-locking of symmetric dumbbells, we will see that we must expand the displacements  $\mathbf{x}_i$  to  $\mathcal{O}(D^{-3})$ . These third order displacements arise from reflections of the dipole force. For example, the  $\mathcal{O}(D^{-2})$  deflection of spring 2 from the dipole originating at dumbell 1 induces a point force at dumbell 2. This point force causes an  $\mathcal{O}(D^{-3})$  displacement at dumbell 1. As we will see, to find  $\mathbf{x}_i$  to  $\mathcal{O}(D^{-3})$  we need only expand the

Oseen tensor to second order in  $D^{-1}$ . Thus, to second order in  $D^{-1}$ , Eq. (3.25) becomes

$$\begin{pmatrix} \dot{\mathbf{x}}_1 + \dot{\theta}_1 \hat{\boldsymbol{\theta}}_1 \\ \dot{\mathbf{x}}_1 - \dot{\theta}_1 \hat{\boldsymbol{\theta}}_1 \\ \dot{\mathbf{x}}_2 + \dot{\theta}_2 \hat{\boldsymbol{\theta}}_2 \\ \dot{\mathbf{x}}_2 - \dot{\theta}_2 \hat{\boldsymbol{\theta}}_2 \end{pmatrix} = \mathbf{H} \begin{pmatrix} \mathbf{f}_{1+} \\ \mathbf{f}_{1-} \\ \mathbf{f}_{2+} \\ \mathbf{f}_{2-} \end{pmatrix}, \quad (3.27)$$

where  $\mathbf{H}$  is the  $8 \times 8$  Oseen tensor evaluated at  $\mathbf{x}_1 = \mathbf{x}_2 = \mathbf{0}$  and expanded to  $\mathcal{O}(D^{-2})$ .

Before describing  $\mathbf{H}$ , it is convenient to re-express Eq. (3.27) in terms of the sums and differences of forces on each paddle,  $\mathbf{f}_i = \mathbf{f}_{i+} + \mathbf{f}_{i-}$  and  $\Delta \mathbf{f}_i = \mathbf{f}_{i+} - \mathbf{f}_{i-}$ , respectively. Note that in terms of these variables, the dimensionless force-balance equation (3.23) becomes

$$-\mathbf{f}_i - \mathbf{x}_i/\epsilon = \mathbf{0}, \quad (3.28)$$

and the dimensionless moment-balance equations become

$$1 - \Delta \mathbf{f}_1 \cdot \hat{\boldsymbol{\theta}}_1 = 0 \quad (3.29)$$

$$1 + \frac{\Delta M}{M_1} - \Delta \mathbf{f}_2 \cdot \hat{\boldsymbol{\theta}}_2 = 0, \quad (3.30)$$

where  $M_1$  is the unit for torque. Returning to Eq. (3.27), we add and subtract the appropriate rows of Eq. (3.27) and rearrange to find

$$\dot{\mathbf{X}} = \frac{1}{\epsilon} \mathbf{A} \mathbf{X} + \mathbf{B} \Delta \mathbf{F} \quad (3.31)$$

$$\dot{\boldsymbol{\Theta}} = \frac{1}{\epsilon} \mathbf{C} \mathbf{X} + \mathbf{D} \Delta \mathbf{F}. \quad (3.32)$$

where  $\mathbf{X}$  and  $\boldsymbol{\Theta}$  are defined as before in Eq. (3.10); the  $4 \times 4$  matrices  $\mathbf{A}$ ,  $\mathbf{B}$ ,  $\mathbf{C}$ , and  $\mathbf{D}$  are given in

the appendix; and

$$\Delta \mathbf{F} = \begin{pmatrix} \Delta \mathbf{f}_1 \\ \Delta \mathbf{f}_2 \end{pmatrix}. \quad (3.33)$$

Expanding in powers of  $D^{-1}$ , we find (see Appendix)

$$\mathbf{A} = \mathbf{A}^{(0)} + D^{-1}\mathbf{A}^{(1)} + \mathcal{O}(D^{-3}) \quad (3.34)$$

$$\mathbf{B} = D^{-2}\mathbf{B}^{(2)} + \mathcal{O}(D^{-3}) \quad (3.35)$$

$$\mathbf{C} = D^{-2}\mathbf{C}^{(2)} + \mathcal{O}(D^{-3}) \quad (3.36)$$

$$\mathbf{D} = \mathbf{D}^{(0)} + \mathcal{O}(D^{-3}). \quad (3.37)$$

Likewise, we expand  $\mathbf{X}$  and  $\Delta \mathbf{F}$  in powers of  $D^{-1}$ :

$$\mathbf{X} = \mathbf{X}^{(0)} + D^{-1}\mathbf{X}^{(1)} + D^{-2}\mathbf{X}^{(2)} + \dots \quad (3.38)$$

$$\Delta \mathbf{F} = \Delta \mathbf{F}^{(0)} + D^{-1}\Delta \mathbf{F}^{(1)} + D^{-2}\Delta \mathbf{F}^{(2)} + \dots \quad (3.39)$$

Since  $\mathbf{B}$  and  $\mathbf{C}$  are  $\mathcal{O}(D^{-2})$  at leading order, our order of expansion is sufficient for determining  $\mathbf{X}$  to  $\mathcal{O}(D^{-3})$  and  $\Delta \mathbf{F}$  to  $\mathcal{O}(D^{-5})$ . At zeroth order, we find  $\mathbf{X}^{(0)} = \mathbf{0}$ , as expected, and  $\Delta \mathbf{F}^{(0)} = [\mathbf{D}^{(0)}]^{-1}\dot{\hat{\Theta}}$ , with

$$\Delta \mathbf{f}_i^{(0)} = \frac{2\dot{\hat{\theta}}_i \hat{\theta}_i}{1 - 3a/8}. \quad (3.40)$$

Substituting  $\Delta \mathbf{f}^{(0)}$  into the moment balance equations (3.29–3.30), taking their sum and difference, using Eq. (3.16) to eliminate  $\theta_1$  and  $\theta_2$  in favor of  $\omega$  and  $\Delta\theta$ , and integrating over one period yields the dimensionless average speed and phase difference,

$$\omega^{(0)} = 1/2(1 - 3a/8) \quad (3.41)$$

$$\Delta \dot{\hat{\theta}}^{(0)} = (1 - 3a/8) \Delta M/M_1. \quad (3.42)$$

Since  $\omega^{(0)}$  and  $\Delta\dot{\theta}^{(0)}$  are independent of  $D$ , they are the average speed and phase-difference, respectively, for non-interacting dumbbells. There is no phase-locking if there is no interaction, and the phase difference increases in proportion to the difference in driving torques,  $\Delta M$ .

Note that the factors of  $3a/8$  in Eq. (3.40) are due to the interaction between the two balls of a given dumbbell: one ball induces a disturbance flow of magnitude  $(6\pi\eta a\dot{\theta})/(8\pi\eta 2) = 3a\dot{\theta}/8$  at the other ball. This disturbance flow hinders the motion of the other ball.

The leading order displacements of the shafts are given by

$$\dot{\mathbf{X}}^{(2)} = \frac{1}{\epsilon} \mathbf{A}^{(0)} \mathbf{X}^{(2)} + \mathbf{B}^{(2)} \Delta \mathbf{F}^{(0)}. \quad (3.43)$$

As in the case of the asymmetric paddles, this equation is readily solved to  $\mathcal{O}(\epsilon^2)$ ; however, the full expression is so cumbersome that we only report the result to leading order in  $\epsilon$  and  $a$  in the appendix. The next order contribution to the force difference is given by

$$0 = \frac{1}{\epsilon} \mathbf{C}^{(2)} \mathbf{X}^{(2)} + \mathbf{D}^{(0)} \Delta \mathbf{F}^{(4)}. \quad (3.44)$$

Again, the full expression for  $\Delta \mathbf{F}^{(4)}$  is so cumbersome that we only report the leading order terms in the appendix. Using  $\Delta \mathbf{F}^{(4)}$  in the difference of the moment equations and averaging yields terms proportional to  $\Delta\dot{\theta}$ , which do not lead to phase-locking. The average of the sum of the moment equations leads to a decrease in the average rotation speed, which together with Eqn. (3.41) yields

$$\omega = \frac{1}{2} - \frac{3a}{16} - \frac{153}{16} \frac{a^2}{D^4}. \quad (3.45)$$

The interacting paddle turn more slowly than they would in isolation.

The third-order displacement of the shafts is determined by

$$\dot{\mathbf{X}}^{(3)} = \frac{1}{\epsilon} \mathbf{A}^{(1)} \mathbf{X}^{(2)} + \frac{1}{\epsilon} \mathbf{A}^{(0)} \mathbf{X}^{(3)}. \quad (3.46)$$

Solving for  $\mathbf{X}^{(3)}$  (see Appendix for leading terms), and substituting into

$$0 = \frac{1}{\epsilon} \mathbf{C}^{(2)} \mathbf{X}^{(3)} + \mathbf{D}^{(0)} \Delta \mathbf{F}^{(5)} \quad (3.47)$$

yields  $\Delta \mathbf{F}^{(5)}$  (see Appendix for leading terms), which has terms that lead to phase-locking. Using moment balance Eqs. (3.29–3.30) and averaging, together with the leading order result (3.40), yields

$$\Delta \dot{\theta} = \frac{1}{2} \Delta M + \frac{243}{8} \epsilon \frac{a^3}{D^5} \sin 2\Delta\theta \quad (3.48)$$

Equation (3.48) is the main result of this section. The (dimensional) synchronization time for the symmetric paddles scales as

$$T_s \sim \frac{D^5}{a^3 R^2} \frac{k R^2}{M_1} \frac{6\pi\eta a R^2}{M_1}. \quad (3.49)$$

When  $\Delta M = 0$ , Eq. (3.48) has a stable fixed point at  $\Delta\theta = \pi/2$ , in accord with our experiments and the more accurate regularized stokeslet simulation of §3.3. As in the case of the asymmetric paddles, the torque difference must be small for phase-locking to occur. The critical torque difference, above which phase-locking cannot occur, is  $\Delta M_{\text{crit}} = (243/4)\epsilon a^3/D^5$ . Note that the average phase-difference in the phase-locked state depends on  $\Delta M$ . Note also that the time for phase-locking depends more strongly on separation for the symmetric paddles compared to the asymmetric paddles. It is not easy to give a simple physical picture for why the paddle separation  $D$  enters the synchronization time with a fifth power. We simply note two effects: (1) the flow induced by the force dipole of one paddle reflects off the other paddle, and then again off the first paddle, leading to four powers of  $D^{-1}$ , and (2) the torque exerted by a flow on the paddle arises from the difference in the flow at the two ends of the paddle, leading to another factor of  $D^{-1}$ . Our case is reminiscent of the fifth power that appears in the reorientation of oscillating dumbbells [79]. Although our experiments were not carried out in the far-field regime, we found that the synchronization time depends more strongly on separation in the symmetric case compared to the

asymmetric case (Fig. 3.3). Finally, we note that to leading order in  $D^{-1}$ , the power dissipated in the synchronized state is independent of  $\Delta\theta$ , since the average rotation speed  $\omega$  in the synchronized state is independent of  $\Delta\theta$  (Eqn. 3.45).

### 3.6 CONCLUSION

To summarize, we have presented perhaps the simplest experimental realization of the phenomenon of hydrodynamic synchronization at low Reynolds number. The requirements for synchronization are subtle: the system must have a slight flexibility to allow small shifts in the positions of the paddles. Since this flexibility is generic, we expect that conditions allowing hydrodynamic synchronization will commonly arise in a wide range of systems at low Reynolds number. On the other hand, our work indicates that hydrodynamic synchronization is not robust, since it requires that the driving moments be fine-tuned to be close to each other.

## Chapter 4

# Micron-scale droplet deposition on a hydrophobic surface using a retreating syringe

Bian Qian, Melissa Loureiro, David Gagnon, Anubhav Tripathi and Kenneth S. Breuer. *Physical Review Letters*, 102, 164502, 2009.

*Droplet deposition onto a hydrophobic surface is studied experimentally and numerically. A wide range of droplet sizes can result from the same syringe, depending strongly on the needle retraction speed. Three regimes are identified according to the motion of the contact line. In Region I, at slow retraction speeds, the contact line expands and large droplets can be achieved. In Region II, at moderate needle speeds, a quasi-cylindrical liquid bridge forms resulting in drops approximately the size of the needle. Finally, at high speeds (Region III), the contact line retracts and droplets much smaller than the syringe diameter are observed. Scaling arguments are presented identifying*

*the dominant mechanisms in each regime. Results from nonlinear numerical simulations agree well with the experiments, although the accuracy of the predictions is limited by inadequate models for the behavior of the dynamic contact angle.*

## 4.1 INTRODUCTION

Contact dispensing methods of fluids are widely used in a variety of applications including direct scanning probe lithography [32], micromachined fountain-pen techniques [33, 85], electrowetting-assisted drop deposition [86] and biofluid dispensing applications [87, 88]. The process is, at first glance, straightforward and is initiated by the formation of a liquid bridge between the substrate and a dispensing syringe. As the syringe retreats, the liquid bridge stretches, grows and breaks, leaving a drop on the substrate. A seemingly simple question can be asked - how does the drop size depend on the syringe geometry, speed and the fluid properties? A comprehensive answer must consider the stability of the liquid bridge and the physics of the moving contact line at the liquid-air-solid interface - both difficult problems. Theoretical studies of liquid bridge stability date back to Rayleigh [36], and have been extended to include gravity and non-cylindrical geometries [89, 41]. In addition, the nonlinear dynamics have been solved numerically, using both 2-D (axisymmetric) [51] and 1-D (slender-jet) [90, 48] models. Previous work has concentrated on geometries in which the contact line is *pinned* at both ends of the liquid bridge [91, 48], and there are only a few results that couple the liquid bridge with a moving contact line [92, 52]. A possible reason for this is the difficulty in solving the flow near the contact line where the continuum equations are invalid [93, 94] and a microscopic description must be imposed (e.g. [95]). In this letter, we focus on the physics of drop dispensing on a flat, smooth, hydrophobic substrate in which the contact line is free to move and is inherently coupled with the liquid bridge stability. Experiments and numerical simulations are used to identify a range of complex flow phenomena which enable the deposited drop size to vary by two orders of magnitude as the syringe retraction speed is changed.

## 4.2 EXPERIMENT

In our experiment, a stainless steel syringe (typical radius,  $R = 200\mu\text{m}$ ) is mounted vertically on a computer-controlled stage. The syringe is connected by a small tube to a 10cc barrel mounted on the same stage. This configuration maintains a constant hydrostatic head,  $H$ , at the syringe tip ( $H \sim 4\text{cm}$ ). The fluid (a 85-15 mixture by volume of glycerol and water) has viscosity  $\mu = 84\text{cP}$  and surface tension  $\gamma = 0.063\text{N/m}$ . The fluid exhibits a static contact angle of  $\sim 90^\circ$  with the substrate, a smooth glass slide coated with a monolayer of octadecyltrichlorosilane (OTS). The syringe is brought down towards the substrate, stopping  $\sim 40\mu\text{m}$  above the surface so that the meniscus touches the substrate and spreads, partially wetting the surface to form a stable drum-shaped liquid bridge (Fig. 4.1). As the syringe retracts at a constant speed,  $U$ , the liquid bridge elongates and evolves due to the changing height,  $h$ , fluid flowing into the bridge through the syringe, (characterized by an inflow velocity,  $u_f$ , and the motion of the contact line between the bridge and the substrate (characterized by a contact line position,  $r$ , and speed,  $u_c$ ). At a critical height,  $h_p$ , the liquid bridge becomes unstable and pinches off rapidly, leaving a drop on the surface. A high speed camera (Photron APX) equipped with a 5X Mitutuyo lens was used to capture the motion of drop dispensing at frames rates up to 10kfps, with a resolution of  $3.33\mu\text{m}/\text{pixel}$ . The experiment was carried out using several syringe diameters, hydrostatic pressures and retraction speeds, and conducted multiple times to ensure repeatability.

Given the simplicity of the experiment, the resulting drop size,  $r_d$ , shows a surprisingly complex dependence on the syringe speed (Fig. 4.1). The data can be divided into three regions, categorized according to the motion of the contact line. At low retraction speeds (Fig. 4.1-I), the flow from the syringe into the liquid column is relatively high, and a bulging liquid bridge forms. The contact angle on the surface exceeds its equilibrium value, and the contact line expands outwards. In this regime, arbitrarily large drops can be formed, with the drop radius scaling with  $U^{-1/2}$ . As one increases the syringe speed (Fig. 4.1-II), the bridge elongation balances the incoming flow and the

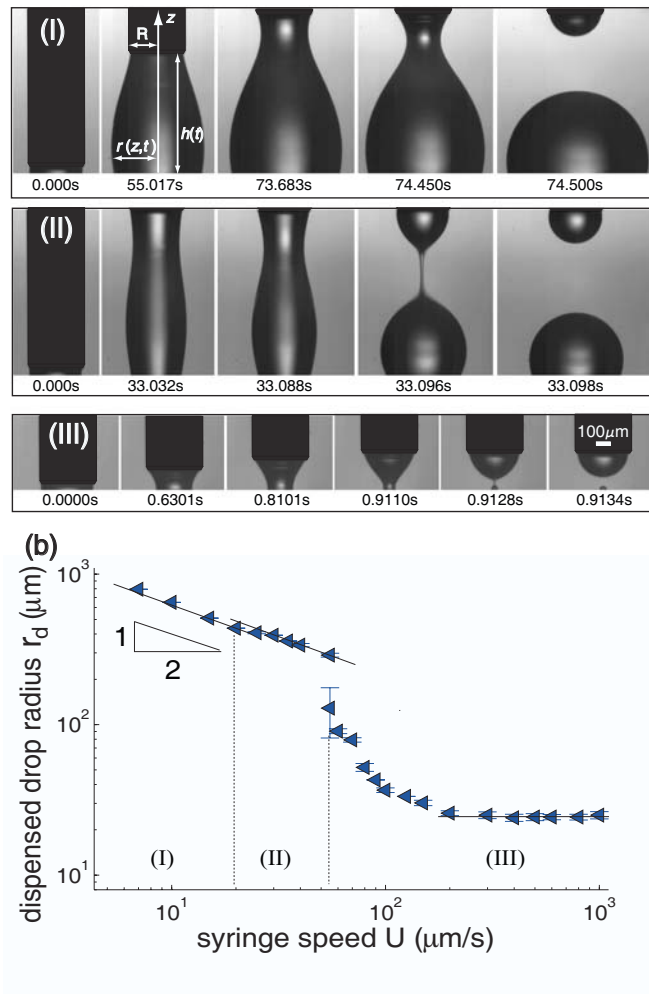


Figure 4.1: Typical sequence of images of drop dispensing at syringe speeds of (I)  $15 \mu\text{m/s}$ , (II)  $35 \mu\text{m/s}$  and (III)  $400 \mu\text{m/s}$ . The syringe radius is  $205 \mu\text{m}$ . (b) Dispersed drop radius,  $r_d$  vs. syringe speed,  $U$ , illustrating the three regions: expanding contact line (I), pinned contact line (II) and retreating contact line (III).

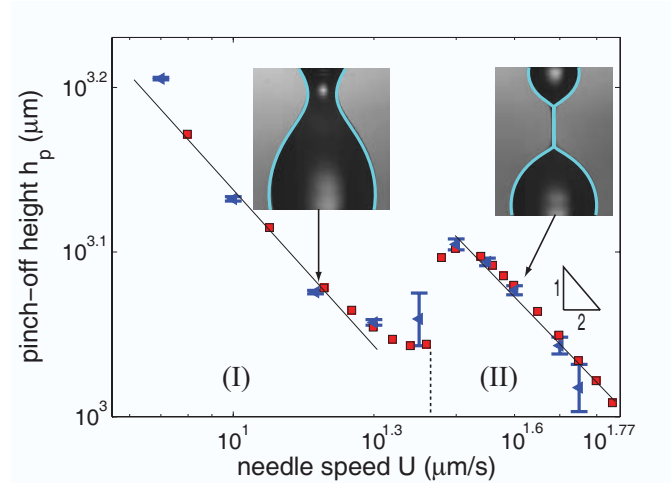


Figure 4.2: Pinch-off height,  $h_p$ , in regions of expanding (I) and fixed (II) contact line. Numerical simulations ( $\square$ ) and experimental measurements ( $\triangleleft$ ) are shown. For this case,  $R = 205\mu m$ ,  $Oh = 0.087$ ,  $Bo = 0.0079$ . The insets show measured and computed shapes of the liquid bridge prior to pinch-off (numerical solution: cyan line).

contact line becomes stationary. In this regime, a quasi-cylindrical liquid bridge forms, finally pinching off as it becomes unstable. The resultant drop size still scales with  $U^{-1/2}$ . However, there is a jump in the drop size between the fixed and expanding contact line regimes due to a jump in the pinch-off height,  $h_p$ , (Fig. 4.2). A third regime is achieved by increasing the syringe speed further (Fig. 4.1-III) The liquid bridge initially adopts a catenoidal shape, but as its contact angle falls below the equilibrium value, the contact line retreats *inward* until, at some critical point, the liquid bridge become unstable and pinches off. The rapid pinching motion drags the contact line inwards at a very high speed ( $\sim 100$  times the syringe speed), and due to this rapid retreating motion, a small drop is deposited, with a diameter that continues to decrease until a minimum drop size is reached, independent of retraction speed, with a diameter approximately one tenth that of the dispensing syringe.

### 4.3 SCALING ARGUMENT

We focus first on region II where the contact line is stationary, and the bridge near-cylindrical. In this region the syringe speed is much smaller than the capillary wave speed,  $U/\sqrt{\gamma/\rho R} = \mathcal{O}(10^{-4})$ , viscous and inertial forces are small, and the liquid bridge can be considered as quasi-static. Since the Bond number,  $\text{Bo} \equiv g\rho R^2/\gamma$ , is small ( $\mathcal{O}(10^{-2})$ ), the hydrostatic pressure in the column is approximately constant, dominated by the Laplace pressure set by the needle curvature,  $\gamma/R$ . This state is amenable to the classical Rayleigh stability analysis, which predicts that the height-to-radius,  $\Lambda = h_p/R$ , must be less than  $2\pi$  to maintain stability [36]. Furthermore, for a marginally-stable liquid bridge (i.e.  $\Lambda/2\pi = 1 + \epsilon$ ), the dimensionless volume,  $V \equiv v_p/\pi R^2 h_p$ , is given by  $V = 1 + 2\epsilon + 5\epsilon^2/2 + \mathcal{O}(\epsilon^3)$  [89]. Rearranging this equation gives  $V = (\Lambda/2\pi)^2 + \mathcal{O}(\epsilon^2)$ , from which we find that  $v_p \sim h_p^3$ . Assuming that the liquid flow from the syringe into the liquid bridge,  $u_f$ , is constant (driven by the net pressure difference,  $\rho g H - \gamma/R$ ), both the volume and the height increase linearly with time:  $v \sim u_f t$ ;  $h \sim Ut$ , from which it is easily derived that the pinch-off height at which the bridge becomes unstable,  $h_p$ , scales like  $U^{-1/2}$ , that the breaking time,  $t_p$ , scales like  $U^{-3/2}$ , and that the drop radius,  $r_d$ , scales like  $U^{-1/2}$ . The experiments support this scaling argument very well (Figs. 4.1-b, 4.2, and 4.3).

### 4.4 NUMERICAL MODEL

In region I, where the contact line expands, the bridge is no longer cylindrical and the Rayleigh stability criteria can be modified by a small parameter,  $\delta = (1 - w^2)/(1 + w^2)$ , where  $w = r(h)/r(0)$  is ratio of the upper and lower contact line radii [41]. In agreement with the theory, we do see a decrease in the pinch-off height,  $\Lambda$ , just as the contact line begins to expand ( $w < 1$ ), although  $\delta$  quickly becomes too large for the perturbation analysis to remain valid. To address this, we employ a numerical model, previously used in studying jet breakup and the stretching of a pinned liquid bridge [90, 48] with modified boundary conditions to include moving contact lines. The

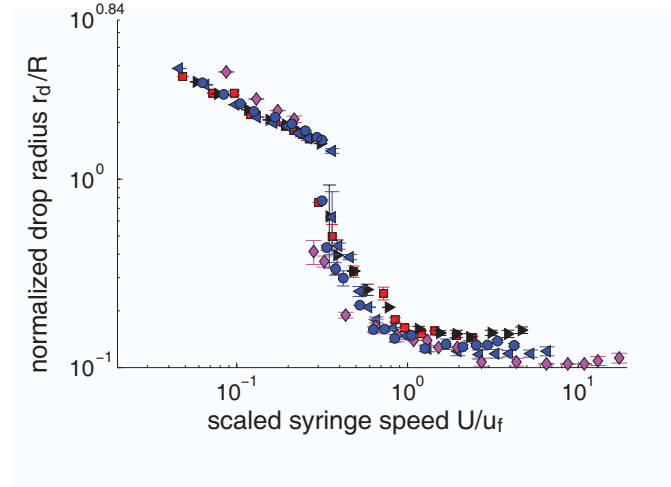


Figure 4.3: Normalized drop sizes,  $r_d/R$ , at different scaled syringe speeds  $U/u_f$  for three syringe radii:  $205\ \mu\text{m}$  ( $\triangleleft$ ),  $255\ \mu\text{m}$  ( $\circ$ ) and  $320\ \mu\text{m}$  ( $\square$ ). The driving pressure,  $\Delta p = \rho g H - (\gamma/R)$  is  $172\text{ (Pa)}$ . Also shown are drop sizes obtained using an  $R = 205\ \mu\text{m}$  syringe and two effective driving pressures:  $\Delta p = 52.0\text{ Pa}$  ( $\diamond$ ) and  $291\text{ Pa}$  ( $\triangleright$ ). The syringe speed is scaled by the flow speed,  $u_f = (R^2/8\mu L)(\rho g H - \gamma/R)$ .

non-dimensionalized equations for conservation of mass and momentum are given by:

$$\partial_t r + ur' = -ru'/2, \quad (4.1)$$

$$(\partial_t u + uu') = -\kappa' + \frac{3\text{Oh}}{r^2}[(r^2 u)'] - \text{Bo}, \quad (4.2)$$

while the evolution of the mean curvature,  $\kappa$ , (included to accurately predict the breakup beyond the validity of slender-jet approximation [90, 50]) is described by:

$$\kappa = \frac{1}{r(1+r'^2)^{1/2}} - \frac{r''}{(1+r'^2)^{3/2}}. \quad (4.3)$$

Here,  $u(z, t)$  and  $r(z, t)$  are the axial flow speed and column radius, normalized by the capillary wave speed,  $u_{cp} = \sqrt{\gamma/\rho R}$  and the syringe radius,  $R$  respectively. Time,  $t$ , is normalized by the capillary time,  $\sqrt{\rho R^3/\gamma}$ . A prime denotes the partial derivative with respect to the axial coordinate,  $z$ . For our experiments, Ohnesorge number  $\text{Oh} \equiv \mu/\sqrt{\rho R \gamma} \approx \mathcal{O}(1)$ . Note that the Weber number,

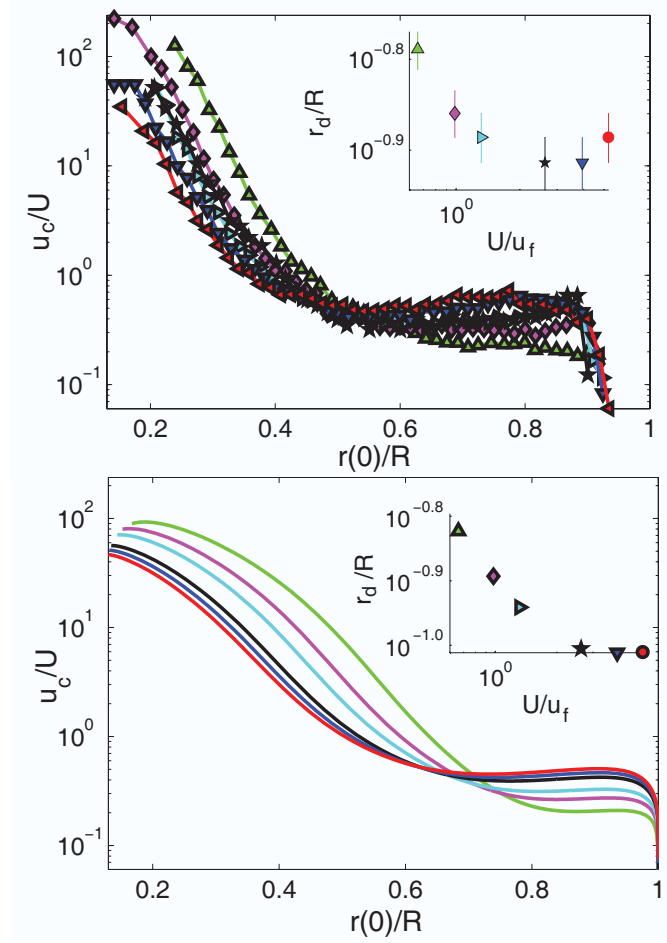


Figure 4.4: (a) Contact line speed,  $u_c/U$ , vs. contact line location,  $r(0, t)/R$ , for various scaled syringe speeds:  $U/u_f = 0.66(\triangle)$ ,  $0.99(\diamond)$ ,  $1.31(\triangleright)$ ,  $2.63(\star)$ ,  $3.94(\nabla)$  and  $5.25(\circ)$ . The inset shows the corresponding final drop size. (b) Corresponding numerical solution.

$We = U/u_{cp}^2$ , should be small for the equations to remain valid [50].

The boundary conditions require that at the top of the liquid bridge,  $h = Ut$ , and that the contact line is pinned,  $r(h) = R$ . The pressure here is the hydrostatic head minus the pressure drop due to the flow:  $p(h) = \rho g H - 8\mu u_f L/R^2$  ( $L$  is the length of the syringe), where the inflow velocity,  $u_f$ , is evaluated as  $u_f = u(h)$ . At the substrate,  $z = 0$ , a solid-wall boundary condition is imposed,  $u(0) = 0$ . This last boundary condition is quite subtle, since the contact line may move with time, and this must be consistent with the solution of the model equations. For a fixed contact

line,  $r(0)$  is a constant and the apparent contact angle varies between  $(\theta_a, \theta_r)$  - the advancing and receding equilibrium contact angles. For a moving contact line, the contact angle deviates from the equilibrium contact angle in order to balance the viscous drag. In general this is a function of the contact line speed,  $u_c = \partial_t r$ . Predicting the contact line behavior and the dynamic contact angle is an area of active research (e.g. [95]). For simplicity, we use constant values for  $(\theta_a, \theta_r)$  of  $100^\circ$  and  $80^\circ$  respectively. The equations (4.1)-(4.3) were solved numerically [90]. Fig. 4.2 indicates excellent agreement achieved between the numerical solutions and the experimental measurements of the pinch-off height, bridge shape, and dependence on the syringe speed.

## 4.5 RESULTS AND DISCUSSIONS

### 4.5.1 Scaling velocity for dispensing speed

The speed at which liquid flows into the bridge,  $u_f$ , is a critical scaling velocity, affecting the pressure boundary condition at the top of the bridge and the rate at which the bridge volume grows (which in turn plays a central role in the bridge stability and subsequent pinch-off). We can estimate  $u_f$  assuming Poiseuille flow through a syringe of length  $L$ , radius  $R$ , and driven by the net pressure difference,  $\Delta p = \rho g H - \gamma/R$ . This estimate differs by only a few percent from the value predicted by the 1-D equations, The appropriateness of this scaling is confirmed in Fig. 4.3 which shows the resultant drop size  $r_d/R$ , versus the scaled retraction speed,  $U/u_f$ , for a series of experiments obtained using three syringe sizes and three hydrostatic pressures (yielding values of  $u_f$  that ranged from 46-414  $\mu\text{m/s}$ ).

### 4.5.2 Contact line speeds for retreating contact lines

The physics of the drop deposition changes abruptly in region III where the contact line begins to retreat. High speed imaging was used to measure the contact line position  $r(0, t)$  from which its speed,  $u_c$ , was calculated (Fig. 4.4(a)). Initially, the contact line is at its maximum ( $r(0)/R \approx 1$ ),

and has zero speed. As the syringe begins to retreat, there is a short period of acceleration, after which time the contact line moves inward with approximately constant speed. However, at a critical radius, approximately  $r(0)/R \sim 0.5$ , we see a dramatic acceleration with  $u_c/U$  reaching  $\mathcal{O}(100)$  immediately prior to pinch-off. In the constant speed region,  $u_c/u_{cp} \ll 1$ , inertial and viscous forces are negligible and the contact line speed is thus determined solely from the mass balance and pressure equilibrium in the bridge. Applying this balance, and the fact that our estimate for  $u_f$  does not depend on  $U$ , it is easy to show geometrically that  $u_c/U \sim 1 - u_f/U$ , a trend confirmed in both the experiments and simulations (Fig. 4.4).

The high-speed contact line phase is driven by the pinch-off instability, during which time a strong capillary force pulls the contact line inward at increasing speed. As  $u_c/u_{cp}$  approaches unity, the viscous forces become significant, and the contact line acceleration decreases immediately prior to pinch-off. We also see that the radial location at which the pinch-off instability initiates moves inward as  $U$  increases, and that this affects the final drop size (Fig 4.4a-inset). A detailed stability analysis of the asymmetric liquid bridge with a moving contact line explains that the smaller bridge volume corresponding to the higher syringe speed postpones the pinch-off instability, resulting in a smaller drop [96]. However, as the syringe speed increases further, the location at which the contact line begins its rapid acceleration moves back out, and the drop size increases (Fig. 4.4(a) inset). A possible reason for this may be that the dynamic contact angle decreases, which destabilizes the liquid bridge earlier [96]. The numerical model yields good comparisons with the experimental results (Fig. 4.4b), capturing the general behavior in the constant speed region (including the increase in  $u_c/U$  with  $U$ ) as well as the onset of rapid acceleration prior to pinch-off. However, the model predicts the critical radius to be larger than that seen in the experiment. We believe that the reason for this discrepancy is that the numerical simulation uses a static retreating contact angle,  $\theta = 80^\circ$ , while the contact angle observed in the experiment varies, from a value larger than  $85^\circ$  prior to the critical point, to a value as low as  $60^\circ$  during the acceleration phase. Furthermore, these angles appear to depend on the syringe speed,  $U$ , and have a strong effect on the resultant

dynamics [96]. A second reason for the degraded agreement between experiment and simulation may be due to high radial velocities observed which violate the assumptions in the the one-dimensional numerical approach considered here, although despite this, the numerical predictions are suprisingly faithful.

## 4.6 CONCLUSION

In summary, the retraction speed of the syringe can exert a huge influence on the size of the resulting droplet that remains on the substrate, with the transition between the three regimes identified being determined by the balance between the flow into the liquid bridge and the onset of the pinch-off instability. At the highest retraction speeds, the small droplet size appears to be determined by the contact line speed, raising the possibility that even smaller droplets might be achieved on surfaces that are smoother and/or exhibit higher contact angles. The numerical model provides surprisingly accurate predictions of the dynamics, even in the regimes where the contact line motion and the presence of viscous and inertial forces make the one-dimensional assumptions questionable.

## Chapter 5

# The motion, stability and breakup of a stretching liquid bridge with a receding contact line

Bian Qian, and Kenneth S. Breuer. *submitted to Journal of Fluid Mechanics, 2010.*

*The complex behavior of drop deposition on a hydrophobic surface is considered by looking at a model problem in which the evolution of a constant-volume liquid bridge is studied as the bridge is stretched. The bridge is pinned with a fixed diameter at the upper contact point, but the contact line at the lower attachment point is free to move on a smooth substrate. Experiments indicate that initially, as the bridge is stretched, the lower contact line slowly retreats inwards. However at a critical radius, the bridge becomes unstable, and the contact line accelerates dramatically, moving inwards very quickly. The bridge subsequently pinches off, and a small droplet is left on the substrate. A quasi-static analysis, using the Young-Laplace equation, is used to accurately predict the shape*

*of the bridge during the initial bridge evolution, including the initial onset of the slow contact line retraction. A stability analysis is used to predict the onset of pinch-off, and a one-dimensional dynamical equation, coupled with a Tanner-law for the dynamic contact angle, is used to model the rapid pinch-off behavior. Excellent agreement between numerical predictions and experiments is found throughout the bridge evolution, and the importance of the dynamic contact line model is demonstrated.*

## 5.1 INTRODUCTION

Contact drop dispensing is the process by which a liquid drop may be deposited on a substrate by touching the surface with a wetted tip, such as a needle or a syringe. Although there are a variety of approaches, the basic dispensing process is initiated by bringing a tip close to a flat substrate so that a liquid bridge is formed between the substrate and the dispensing syringe, as sketched in Fig. 5.1. As the syringe retreats, the liquid bridge stretches, grows, and breaks, leaving a drop on the substrate. The technique has many industrial applications, including the printing industry and dispensing of glue for packaging. Most recently, it has been adapted for a variety of novel uses at small scales, such as direct scanning probe lithography [32], micromachined fountain-pen techniques [33, 85] and in the formation of micro-arrays of biological materials [31]. Despite the simplicity of the operation, the exact control of the dispensing drop size is complicated by several factors, such as the syringe geometry, the dispensing speed, the liquid properties and the surface wettability. For the accurate prediction of drop sizes, precise knowledge of how these factors affect the dispensing process is required. In particular, an accurate prediction of the stability and the breakup of the liquid bridge is needed.

The study of liquid bridges was pioneered over one hundred years ago by Plateau who experimentally investigating the stability of an infinite vertical falling water jet [35], in which he observed that the maximum ratio of the stable length to the jet diameter is about a constant  $\pi$ . The theo-

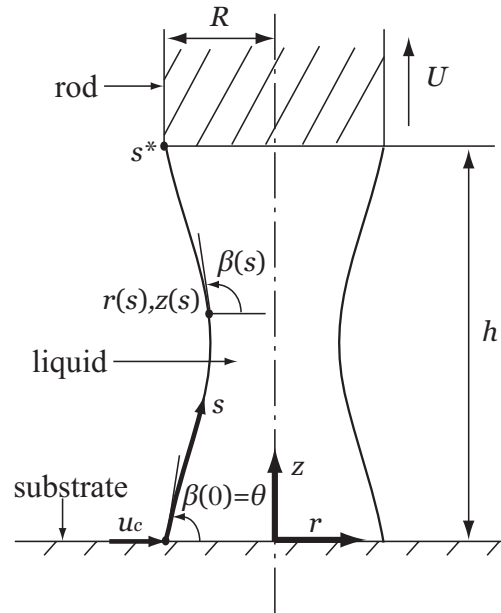


Figure 5.1: Geometry and coordinate system for an axisymmetric liquid bridge with a free moving contact line on the substrate.

retical derivation of the observed stable length limit was given by Rayleigh with a linear stability analysis [36], which is known as Rayleigh-Plateau limit. Later broad applications of liquid bridges in industry inspired intensive studies of the stability of a static weightless axisymmetric liquid bridge confined between two circular disks, in which the critical height of the bridge as a function of the bridge volume was theoretically calculated and experimentally tested [97, 98, 99, 100, 43]. The influences of gravity and supporting disks unequalness on the stable limit were also investigated during the past two decades [46, 44, 43, 41, 44, 45]. Although the study of static liquid bridges has reached a level of maturity, the investigation of the dynamic stretching of a liquid bridge has to wait until quite recently, due to the difficulties in experimentally recording the rapid bridge breakup as well as the complexities associated with the mathematical treatments in theory [46, 101, 102]. The representative work by Zhang *et al.* [48] exhaustively investigated the dependence of breakup features on the stretching speed and the liquid properties with both experimental and numerical methods, and directly compared experiments with theory, finding quantitative agreement, despite the fact that the the calculations were restricted to moderate stretching speeds due to the limitation

of the 1D approximate model [47]. More recently, the numerical calculations have been extended using two-dimensional models and used to investigate, among other things, the effects of different supporting geometries [50] and the effects of surfactants [51, 52] on the breakup of a dynamically stretching liquid bridge. All these previous studies, however, concentrated on geometries in which both the upper and lower contact lines are pinned. In contrast, the contact drop dispensing problem is characterized by the fact that the lower contact line is free to move. This modification to the liquid bridge breakup has not been addressed, perhaps due to the lack of accurate models for the dynamic contact line behavior. However, this frontier too has seen recent progress, including numerical simulations using a diffusive interface model [92], Navier slip boundary condition while maintaining a constant contact angle [103], and an approach using an empirical, velocity-dependent, dynamic contact angle model [52]. These studies have shown that the dynamic contact line is crucial for the breakup dynamics of a stretching liquid bridge and for these reasons, we assume that it has a strong effect on the drop size in the contact dispensing problem.

Previous experiments by our group concerning drop generation on a hydrophobic surface have shown that, by changing the speed of the retracting needle, one can control the contact line motion, and through these means, one can generate a broad range of drop sizes using a single syringe [49]. The drop dispensing physics can be divided into three regions: expanding contact line, fixed contact line and receding contact line. For low syringe retraction speeds,  $U$ , the contact line slowly expands, and arbitrarily large drops can be generated. In these regions, the drop sizes,  $r_d$ , were shown to vary as  $U^{-1/2}$ , and due to the low syringe speed and the slow contact line motion, the bridge evolution and breakup was well-predicted by quasi-static theory using Rayleigh-Plateau instability theory, and its extensions for non-cylindrical bridges [41, 89, 45]. However, for higher values of  $U$ , the contact line recedes, and the process is more complex, and was observed to be comprised of two phases [49]: an initial phase characterized by a slow (quasi-static) contact line retraction, followed by a *very* rapid phase in which the contact line speed is comparable to the capillary wave speed, and during which the contact line angle is seen to depend on the speed, and to be significantly

lower than its quasi-static value.

The retreating contact line mode of droplet deposition is of great technical interest, since it allows micron-scale droplets to be deposited using millimeter-scale hardware. However, the complexities of the governing physics are considerable and several questions were left unanswered by the original experiments of Qian *et al.* [49]. These questions include determining when the contact line starts to move, at what point does the bridge become unstable and begins to pinchoff, and lastly how the final drop size depends on the liquid-surface interaction. In this article, we address these questions by studying in detail the drop dispensing in the receding contact line region using both experimental and numerical tools. To facilitate the study, we have simplified the drop dispensing problem in one aspect, and we consider drops dispensing from a constant-volume liquid bridge, instead of a bridge defined by a constant pressure at the upper boundary (fed by the flow from a reservoir through a syringe). In our experiment, the dispensing drop sizes and the contact line motions were measured for different dispensing speeds and liquid volumes. Our theoretical analysis is divided into three components: (a) a quasi-static analysis using the Young-Laplace equation to describe the initial bridge evolution (although, still allowing for slow contact line motion); (b) a stability analysis to predict the onset of the bridge pinchoff process and finally (c) a quasi-one dimensional dynamic analysis to model the rapid contact line motion and pinchoff process. In this last stage, we employ a moving contact line model with a dynamic contact angle.

The article is organized as follows: the experimental setup is depicted in Sec. 5.2. The equilibrium (quasi-static) and accompanying stability analysis is stated in Sec. 5.3.1, while the dynamic model and relevant boundary conditions are described in Sec. 5.3.2. Experimental results present in Sec. 5.4.1. The stable state of the liquid bridge with a moving contact line is determined in Sec. 5.4.2. Numerical calculations are shown and discussed in Sec. 5.4.3.

## 5.2 EXPERIMENTAL SETUP

The experiment setup (Fig. 5.1) is similar to the one in our previous study [49], but modified for constant volume dispensing. A cylindrical rod (diameter  $510\mu\text{m}$ ) is mounted to a 3D motorized stage which is capable of moving at speeds  $U = 10 - 1000\mu\text{m/s}$  with sub-micron accuracy. The liquid used is 85/15 (volume) glycerin/water mixture which has density  $\rho = 1.222 \times 10^6 \text{ (g/m}^3\text{)}$ , viscosity  $\mu = 84\text{cp}$  and surface tension  $\gamma = 63 \text{ (g/s}^2\text{)}$ . The substrate is a piece of smooth glass slide coated with a monolayer of OTS, on which the liquid exhibits a contact angle  $\sim 90^\circ \pm 5^\circ$ . Limited experiments were conducted on a less hydrophobic substrate. The small volume of liquid (typical volume  $0.2\mu\text{L}$ ) is loaded on the substrate with constant pressure dispensing [49]. The loaded liquid drop is vertically aligned with the dispensing rod which is moved horizontally by a motorized stage. As the rod approaches to the liquid drop, a small constant volume liquid bridge is formed. For measurements at one volume value, multiple dispensing are taken on the same spot of the substrate so that the liquid only needs to be loaded once, which reduces the effect of potential volume variations induced by liquid loading. The size of the liquid bridge is monitored during the data acquisition and it was confirmed that the maximum volume variation due to evaporation is less than 1%. A high-speed camera (Photron APX) equipped with a 5X Mitutuyo lens was used to capture the evolution of liquid bridges at frames rates up to 10 kfps, with a resolution of  $3.33\mu\text{m/pixel}$ . The recorded images analyzed using MATLAB.

In our experimental system, there are three governing dimensionless numbers: Weber number  $We \equiv \rho U^2 R / \gamma \sim \mathcal{O}(10^{-6})$ , Bond number  $Bo \equiv g \rho R^2 / \gamma \sim \mathcal{O}(10^{-2})$ , and Ohnesorge number  $Oh \equiv \mu / \sqrt{\rho R \gamma} \sim \mathcal{O}(1)$ . These three dimensionless groups represent the relative importance of inertial force/surface tension, gravity/surface tension and viscous force/surface tension respectively. The Ohnesorge number can be view as a Capillary number  $Ca \equiv \mu u_{cp} / \gamma$  based on the capillary wave speed  $u_{cp} = \sqrt{\gamma / \rho R}$  and it is used to compare viscous force/surface tension for liquid bridge breaking. However, before the bridge breaking, the flow speed inside the stretching bridge has

the order of the rod speed  $U$  and therefore the capillary number  $\text{Ca} \equiv \mu U / \gamma$  based on the the rod speed is a more appropriate measure of the relative importance of viscous force/surface tension. For our setup, the Weber number  $\text{We} \sim \mathcal{O}(10^{-6})$  and the Capillary number  $\text{Ca} \sim \mathcal{O}(10^{-3})$  are small so that the inertial and the viscous force in this phase are negligible compared to the surface force. Therefore, the bridge shape is considered to be in equilibrium at each instant of time and the stretching can be treated quasi-statically.

## 5.3 THEORETICAL CONSIDERATIONS

### 5.3.1 Stability of an equilibrium static liquid bridge

Based on the coordinate system defined in Fig. 5.1, the static equilibrium profile of an axisymmetric liquid bridge is described by the Young-Laplace equations,

$$r''(s) = -z'(s)\beta'(s), \quad (5.1a)$$

$$z''(s) = r'(s)\beta'(s), \quad (5.1b)$$

$$\beta'(s) = -z(s) + \frac{P-P_0}{\sqrt{\rho g \gamma}} - \frac{z'(s)}{r(s)} \quad (5.1c)$$

with appropriate initial conditions  $r(0), r'(0) = \cos(\theta), z(0) = 0, z'(0) = \sin(\theta), \beta(0) = \theta$ . Here  $s$  is the arc length of the free surface with its origin on the substrate and a prime denotes differentiation with respect to the arc length.  $r(s)$  is the radius of the liquid bridge,  $z(s)$  is the vertical distance from the substrate, and  $\beta(s)$  is the angle between the radial axis and the tangent to the interface.  $\rho$  and  $\gamma$  is the liquid density and surface tension.  $g$  is the standard gravity constant. The pressure difference  $(P - P_0)$  across the liquid interface at the coordinate origin is adjustable to make the solution satisfy the boundary condition of  $r(s^*) = R$ , in which  $s^*$  is the point at the rod ( $z = h$ ). For a liquid bridge having a volume  $v$  and a height  $z(s^*) = h$ , only one of the two initial conditions: the contact line radius  $r(0)$  and the contact angle  $\theta$  should be specified to determine the shape and

the other is a free parameter to fulfill the volume constraint:  $\int_0^h r^2 dz = v$ . Which initial condition is to be specified depends on the motion state of the contact line: pinned or receding.

The stability of an equilibrium liquid bridge can be determined according to the method introduced by [42], which is an eigenvalue problem

$$L\varphi_0 + \nu = \alpha\varphi_0 \quad (0 \leq s \leq s^*) \quad (5.2a)$$

$$\varphi_0(0) = 0, \varphi_0(s^*) = 0, \int_0^{s^*} r\varphi_0 ds = 0, \quad (5.2b)$$

$$L\varphi_1 + \frac{1}{r^2} = \alpha\varphi_1 \quad (0 \leq s \leq s^*), \quad (5.2c)$$

$$\varphi_1(0) = 0, \varphi_1(s^*) = 0. \quad (5.2d)$$

Here

$$L\varphi \equiv -\varphi'' - \frac{r'}{r}\varphi' - a(s)\varphi, \quad (5.3a)$$

$$a(s) = -r'(s) - \beta'^2(s) - \left(\frac{z'(s)}{r(s)}\right)^2. \quad (5.3b)$$

$\nu$  is an unknown constant beforehand, and primes denote derivatives with respect to  $s$ .  $\varphi_0$  and  $\varphi_1$  correspond to the axisymmetric perturbations and the most dangerous nonaxisymmetric perturbation to the liquid bridge respectively.  $\alpha$  is the eigenvalues of Eq. 5.3. A positive sign of the smallest eigenvalue signifies a stable equilibrium liquid bridge and a vanishing smallest eigenvalue represents the critical state of a liquid bridge. The stability boundary for a bridge with given contact line radius,  $r(0)$ , can be computed following the numerical algorithm described in [43] and then the stability of the calculated liquid bridge is known.

The liquid bridge is assumed to stretch through a sequence of quasi-static states. At each state, the bridge height is specified and the stable equilibrium bridge profile can be solved. Successively applying the calculation for varying heights by a small step, we can track the evolution of the bridge. This tracking process is terminated when the bridge stretches to a critical height at which no

equilibrium solution exists or the solution becomes unstable. The critical height can be pinpointed by iterating with a refined height step.

### 5.3.2 Numerical model of a dynamic stretching liquid bridge

Beyond the critical equilibrium state, the bridge starts breaking and its shape deforms quickly. This is no longer on a quasi-static condition. To simulate the dynamic breakup, 2D Navier-Stokes equations need to be solved with appropriate kinematic and traction boundary conditions [50]. To simplify the mathematical treatment, Eggers used the slender-jet approximation to truncated the high order terms in the 2D governing equations to arrive a set of 1D model equations [90],

$$\partial_t r + ur_z = -ru_z/2, \quad (5.4a)$$

$$(\partial_t u + uu_z) = -\frac{\gamma}{\rho}\kappa_z + \frac{3\mu}{r^2}[(r^2u_z)_z] - g. \quad (5.4b)$$

Here  $u(z, t)$  and  $r(z, t)$  are the axial flow speed and column radius.  $g$  is the gravity constant. The full mean curvature,  $\kappa$ ,

$$\kappa = \frac{1}{r(1+r_z^2)^{1/2}} - \frac{r_{zz}}{(1+r_z^2)^{3/2}}, \quad (5.5)$$

is maintained to precisely predict the bridge shapes. This model has been successfully applied to studying jet breaking [90] and liquid bridge stretching [48, 49]. Comparisons in the numerical results for stretching bridges with fixed contact lines,  $r(0)/R = 1$ , between the exact 2D model and the approximated 1D model showed that the 1D model gives an accurate prediction of the macroscopic features of the bridge breakup as long as the ratio of the stretching speed,  $U$ , to the capillary wave speed,  $u_{cp} = \sqrt{\gamma/\rho R}$ , is much less than one [50]. In our experiment, a typical capillary wave speed is 10 cm/s, which is much larger than the used stretching speeds. Although close to the bridge pinch-off the high radial speed violates the assumption of the 1D model, we nevertheless use this model to simulate the dispensing process, and will discuss its accuracy and

limitations.

To solve the 1D equations (5.4 - 5.5), boundary conditions at both ends of the bridge should be specified. At the top of the liquid bridge, the contact line is pinned,  $r(h) = R$ , and no flow penetrates the rod surface,  $u(h) = 0$ . On the substrate, the axial flow speed is zero,  $u(0) = 0$ . Since the contact line allows to move freely,  $r(0, t)$  is unknown and the contact angle  $r_z(0, t) = \cot(\theta)$  must be prescribed. The simplest way to model the contact angle is to define  $\theta(t)$  as a constant. However, the fixed contact angle model is not able to capture the contact angle dependence on the contact line speed,  $u_c = r_t(0, t)$ , [104, 95]. An improvement, thus, is to relate the contact angle to the contact line speed using an empirical equation [105, 106]

$$u_c = \lambda(\theta - \theta_r)^n. \quad (5.6)$$

Here  $(\theta - \theta_r)$  is the deviation of the dynamic contact angle from the static receding angle.  $\lambda$  is an empirically determined constant that is a measure of the contact line speed.  $n$  is another empirical constant which was experimentally observed to be between 1 and 3 [106]. This dynamic contact angle model has been successfully applied to simulate the spin coating [107] and pin-tool printing [52]. In this paper, we adopted this model as a boundary condition into the numerical calculation.

## 5.4 RESULTS AND DISCUSSIONS

### 5.4.1 Overall behavior of constant volume deposition

The general behavior of the drop deposition experiment is reviewed here, and summarized graphically in Fig. 5.2. As the rod retracts (and the bridge height,  $\Lambda = h/2R$ , increases), the liquid bridge stretches, developing axial curvature (and hence negative pressure inside the liquid volume). The measured receding contact line speed,  $u_c/U$ , versus the contact line radius,  $\Upsilon = r(0)/R$ , is shown

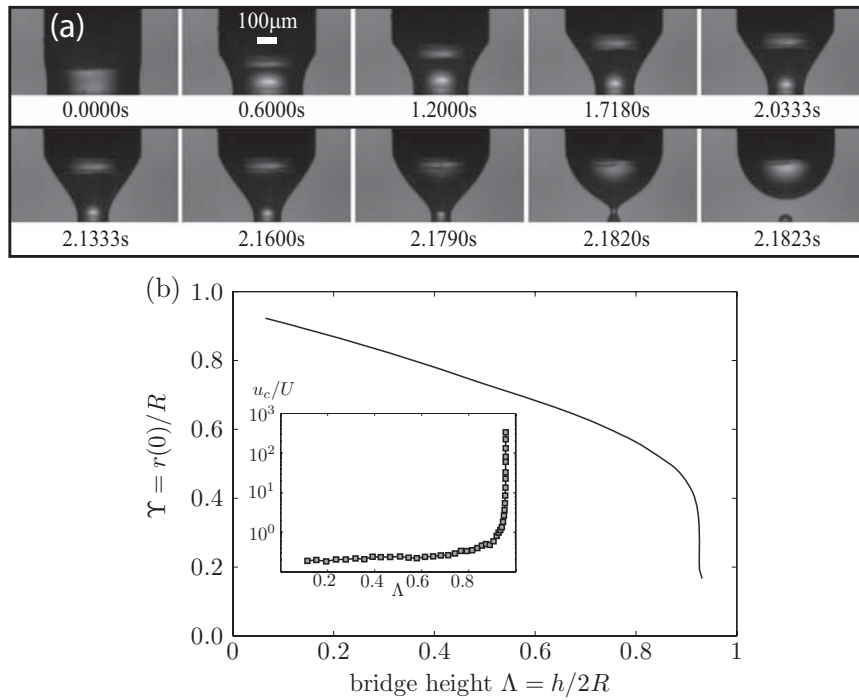


Figure 5.2: (a) Typical sequence of images of drop dispensing on a hydrophobic surface with a receding contact line. Two stages of contact line motions were observed: a slow retreating at the beginning (top row) and a rapid retraction prior to the bridge pinch-off (bottom row). The rod is  $510 \mu\text{m}$  in diameter and it lifts at a constant speed  $100 \mu\text{m/s}$ . (b) Corresponding measured contact line locations  $\Upsilon = r(0)/R$  as a function of bridge's heights  $\Lambda = h/2R$ . The inset shows the contact line speeds  $u_c/U$  measured from the evolution of the contact line.

for several retraction speeds,  $U$ , in Fig. 5.3 (for convenience, the contact line speed is defined as positive when the contact line contracts). As discussed earlier, we identify two phases of the bridge evolution. Initially, the contact line moves at a low speed which is comparable to the stretching speed,  $u_c/U \approx 1$ . Below a critical radius the contact line accelerates quickly to a speed comparable to the capillary wave speed. Although this behavior is generically similar to that observed in constant pressure dispensing [49], we see two chief differences. Firstly, during the low-speed phase of constant pressure dispensing, the normalized contact line speed,  $u_c/U$ , shows a weak dependence on  $U$ , whereas in the constant-volume case the speed collapses with no further dependence on the stretching speed. This scaling confirms the assumption of quasi-static stretching during this phase, since the contact line location,  $r(0)$ , as well as the bridge shape, is solely determined by the bridge height,  $h$ . In the constant pressure case, the weak dependence on  $U$  is due to the fact that the bridge volume increases with time. Secondly, in the constant-pressure case, both the critical radius at which the contact line starts to accelerate and the radius at which the contact line reaches its maximum speed decrease with the retraction speed,  $U$ . In contrast, for the current case, there is no discernible change in the critical radius as a function of  $U$ , and the variation in the maximum contact line speed location is more moderate than was observed in the constant-pressure case.

In the rapid-retraction phase, plotting the dimensionless contact line speed (inset of Fig. 5.3) as a function of the time to bridge breakup,  $t_m$ , shows a power-law dependence,  $u_c/u_{cp} \sim (t_m/t_{cp})^{-3/4}$ . Similar power-law behaviors have been observed in drop coalescence and wetting [108, 109, 110] who also found that the scaling exponent depends on the type of force resisting drop deformation [111] and the static equilibrium contact angle [110]. Note that the speed and time scale,  $u_{cp} = \sqrt{\gamma/\rho g}$  and  $t_{cp} = \sqrt{\rho R^3/\gamma}$ , are determined only by the liquid properties which is fixed in the experiment and thus the dimensional maximum contact line speed weakly relies on the dispensing speed. However, the dimensional contact line speed at the starting acceleration point does change with  $U$  and it is approximately equal to  $U$ . Therefore, the time taken to accelerate to the maximum contact line speed, and the distance that contact line retreats within that time both decrease with  $U$ .

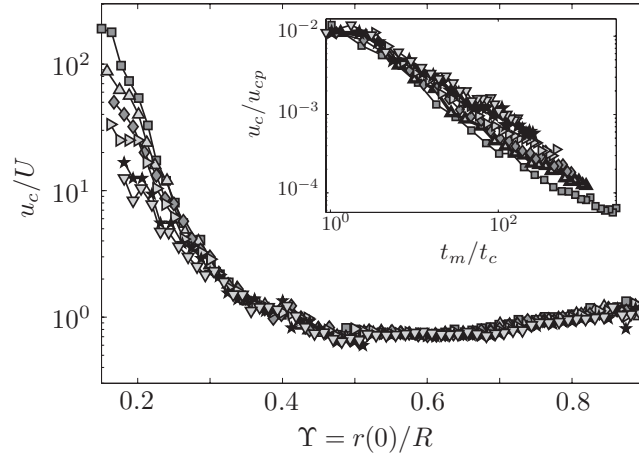


Figure 5.3: Experimentally measured non-dimensional contact line speeds from constant volume dispensing for  $U = 35(\square), 80(\triangle), 125(\diamond), 200(\triangleright), 400(\star)$  and  $600(\nabla) \mu\text{m/s}$ . The inset shows the dimensionless contact line speed as a function of time to the breakup,  $t_m$ . Speed and time is scaled by  $u_{cp} = \sqrt{\gamma/\rho g}$  and  $t_c = \sqrt{\rho R^3/\gamma}$ .

Combined with the fact that the critical radius is weakly dependent on the dispensing speed, we can conclude that the deposition drop size should increase with the dispensing speed for constant volume dispensing.

### Drop size

This expected dependence of the drop size on the retraction speed is confirmed in Figure 5.4, which shows the change in the dispensed drop size as a function of the rod speed for several different liquid volumes. As argued above, for a given volume, the drop size increases as the rod speed increases. This contrasts to that observed in constant-pressure dispensing, in which drop sizes dramatically decreases with increasing syringe speed, reaching a minimum the drop size, after which  $r_d$  starts to increase slowly [49]. Comparison of drop sizes between different bridge volumes reveals that enlarging the volume causes the drop size to increase, and furthermore, that the increase with  $U$  is more apparent for the larger initial volumes. Additionally, some data (not presented here) from experiments using a less hydrophobic surface ( $\theta_r = 70^\circ \pm 10^\circ$ ) shows that the drops generated on the less hydrophobic surface are larger than on a more hydrophobic surface for the same bridge

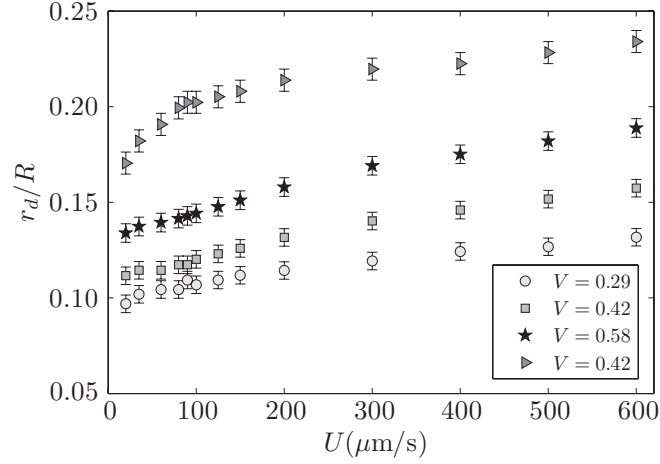


Figure 5.4: Experimentally measured dispensing drop sizes vary with rod speeds for three bridge volumes. The liquid bridges have a static receding contact angle  $\theta_r \sim 85^\circ$  on the surface. Also shown are drops dispensing on a less hydrophobic surface  $\theta_r \sim 70^\circ$  ( $\triangleright$ ) for one volume value  $V = 0.42$ . The rod has a diameter  $510\mu\text{m}$ .

volume. Unfortunately, difficulties in preparing consistent surfaces with a variety of contact angles prevented us from systematically investigating the effects of surface wettability on the resultant drop size.

#### 5.4.2 Stability of static liquid bridge

Having described the overall behavior of the drop deposition, the following sections use the analytical methods described earlier to quantitatively model the details of both the static, and dynamic phases of the process. In this section, we use the calculation procedure, described in sec. 5.3.1, to predict the point at which the contact line first moves inward, and the critical contact line radius at which the bridge becomes unstable.

##### The first movement of a contact line

The stable state of a liquid bridge with a fixed contact line can be determined in a plane of dimensionless bridge height,  $\Lambda = h/2R$ , and volume,  $V = v/\pi R^3$  (Fig. 5.5). Initially, the liquid bridge is cylindrical, with the contact line at  $\Upsilon = r(0)/R = 1$  and the contact angle at  $90^\circ$ ,

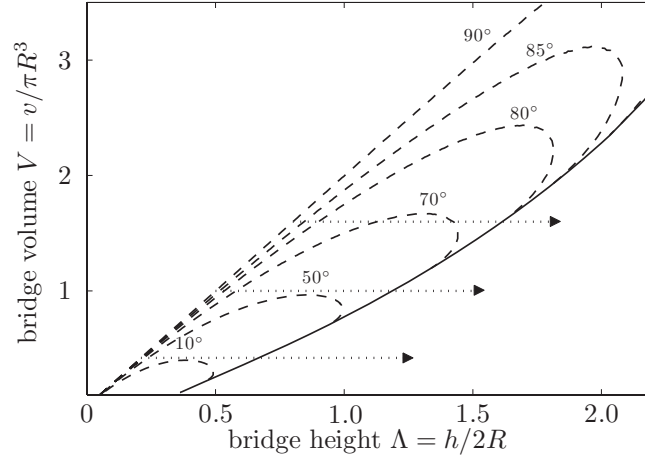


Figure 5.5: Starting moving point of a fixed contact line  $\Upsilon = 1$  on the  $(\Lambda, V)$  plane under a constraint of the contact angle  $\theta \geq \theta_r$ . The solid line is the stable limit of an axisymmetric liquid bridge with  $\Upsilon = 1$  and no contact angle constraint. The dash line is the level line on which the bridges have the same contact angle  $\theta$ . The dotted line shows the evolution path of a stretching liquid bridge of constant volume.

represented by the left-most contour. The experimental evolution follows a horizontal line, starting at this left-most line, and moving towards the right (indicated by the dotted arrows). As the rod retracts, the liquid bridge stretches and the contact angle at the substrate changes, first decreasing, and then increasing again. However, the bridge cannot be extruded indefinitely, and the stability boundary at which a statically stable bridge can no longer exist (Eq. 5.3) is shown as the solid line on the right side of Fig. 5.5. Crossing this boundary marks the onset of the rapid retraction phase.

This example is only valid for the bridge whose contact line is pinned at  $\Upsilon = 1$ . If there exists an additional wetting angle constraint,  $\theta \geq \theta_r$ , the contact line may move before the bridge pinchoff. In this situation, as  $\Lambda$  increases, and it crosses the contour at which the static contact angle,  $\theta$ , equals the receding contact angle,  $\theta_r$ , the contact line will start to retreat, at which point a new series of  $\Lambda - V$  maps, each representing the instantaneous value of  $\Upsilon$  need to be consulted.

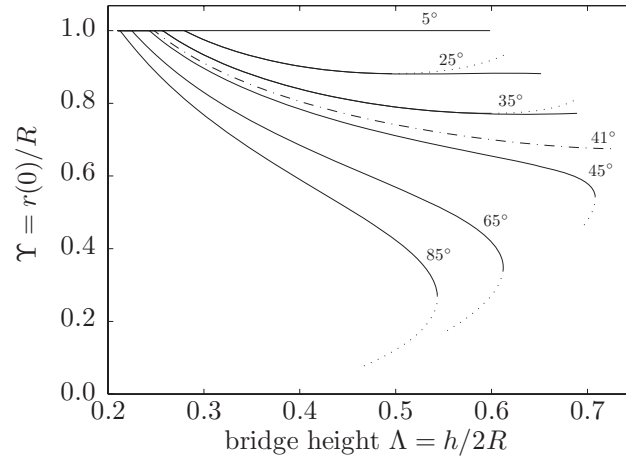


Figure 5.6: Static calculation of the locations of a free moving contact line  $\Upsilon$  as a function of the bridge height  $\Lambda$  under a contact angle constraint  $\theta \geq \theta_r$ . Calculated evolution curves (solid line) are shown for different limiting wetting angles  $\theta_r$ . The dotted line shows the theoretical possible but not practically feasible contact line locations. The dash-dot line shows the boundary across which the transition takes place from the fixed-receding-fixed contact line to the fixed-receding contact line.

### Evolution of freely moving contact lines

As the contact line moves, it is more convenient to analyze the problem in terms of the contact line position,  $\Upsilon = r(0)/R$ , versus the bridge height,  $\Lambda$ . For a given volume in the liquid bridge, the limiting wetting angles define three types of contact line behavior, and they can be identified on the  $(\Lambda, \Upsilon)$  plane: always-fixed contact line, fixed then receding contact line, and fixed-receding-fixed contact line (Fig. 5.6). For a low limiting wetting angle, for example  $5^\circ$ , the contact angle never falls below the critical value, and the contact line is always pinned at its initial position  $\Upsilon = 1$  until the bridge becomes unstable. During the stretching, the contact angle decreases initially and then increases again (as predicted by Fig 5.5).

For large minimum wetting angle, such as  $\theta = 65^\circ$ , the contact line is initially fixed, but as  $\Lambda$  increases, the contact angle reaches its limiting wetting angle and the contact line start to recede. The radius of the contact line continues to decrease monotonically with  $\Lambda$  (with the contact angle at its limiting value). However, at a critical height, there exists no statically stable solution (the

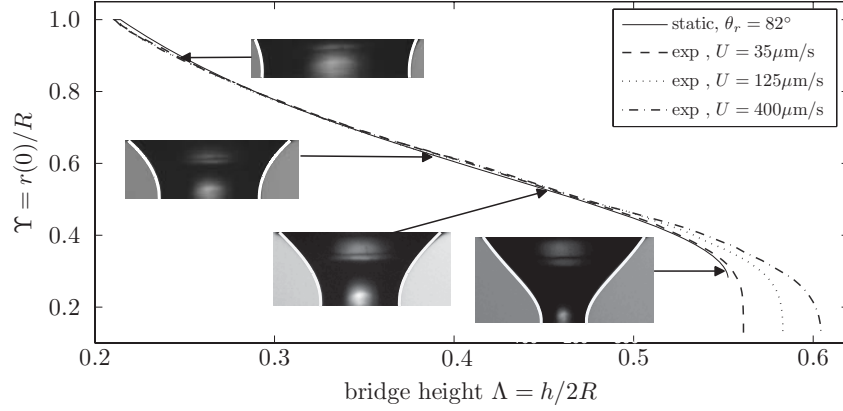


Figure 5.7: Evolution of contact lines from static calculation (solid) compared to those from experiments at three different stretching speeds  $U$  (dash). The insets show the comparison of calculated bridge shapes (white line) to that imaged from experiment at a stretching speed  $U = 35\mu\text{m/s}$ .

evolution path becomes vertical), and the bridge breaks. Note that for a given contact angle,  $\theta$ , there exists a second static equilibrium solution (dotted lines) for the same height  $\Lambda$ , but with a different contact line radius,  $\Upsilon$ . However, in our experiments the contact line recedes smoothly and no “radius jumping” was observed, so the lower branch of the static solution (dotted line) was not practically accessible.

For intermediate limiting wetting angles, for example,  $\theta = 35^\circ$ , the initial contact line behavior is as before: fixed initially, then retreating. However, for these cases, the theory predicts that when the bridge elongates to a certain height, the contact line reaches a minimum radius and then starts to expand (dotted line). In practice, however, contact angle hysteresis will result in a different observed path, and the contact line will stop moving while the contact angle grows above the receding angle (a horizontal line on the  $\Lambda - \Upsilon$  plane). One might then observe a situation in which the contact angle grows to its limiting advancing value, at which point the contact line would then expand, now on a different  $\theta$  line.

In our experiment, the liquid on the substrate exhibited a high static receding contact angle ( $\sim 85^\circ$ ) and so only the fixed-receding type of contact line behavior was observed. From the

Figure 5.6, it is clear that at a high limiting wetting angle the evolution path has a steeper slope and the contact line radius,  $\Upsilon$ , reduces faster with the stretching height. The end point of a evolution path denotes the critical radius at which the bridge breaks. For the fixed-receding contact lines, the breaking height and the critical radius both increase with the reducing wetting angle.

The prediction for  $\theta_r = 82^\circ$  is compared with our experimental data (Figure 5.7) for three retraction speeds. The angle chosen for calculation is slightly lower than the static receding angle ( $\sim 85^\circ$ ) observed in experiment due to the fact that the dynamic receding contact angle is always a little lower than the static angle. The dynamic contact angle is velocity-dependent [106, 105, 95] and it varies during the bridge stretching. However, during the quasi-static phase, the contact line speed is so small that the variations in the dynamic contact angle variation are too small to significantly affect the evolution path, and the static theory gives an excellent prediction of the contact line motion and the overall bridge profile for all three rod speeds. Close to the critical state, the contact line speed is much faster and the dynamic contact angle decreases more noticeably from its equilibrium value. This behavior results in an increase of the breaking height with higher rod speed. Additionally, as the rod speed increases, the viscous forces inside the liquid bridge are larger, which help to stabilize the stretching bridge and further postpone the breakup [48]. For both these reasons, the agreement between the experiment and the simple static theory is compromised in this region.

### **Effects of volumes and minimum wetting angles on the critical radius**

The critical radii at which the contact line starts to move, defined as  $\Upsilon^*$ , are shown as a function of the minimum wetting angles for four different bridge volumes in Figure 5.8). For each volume, there exists a wetting angle below which the critical radius remains at  $\Upsilon^* = 1$ , meaning that contact angle never reaches the minimum wetting angle and the contact line does not retreat during the bridge stretching process. For these fixed contact line cases, the neutrally-stable state of the liquid bridge is determined only by the bridge volume and height  $(V, \Lambda)$  [43]. However, if the wetting angle

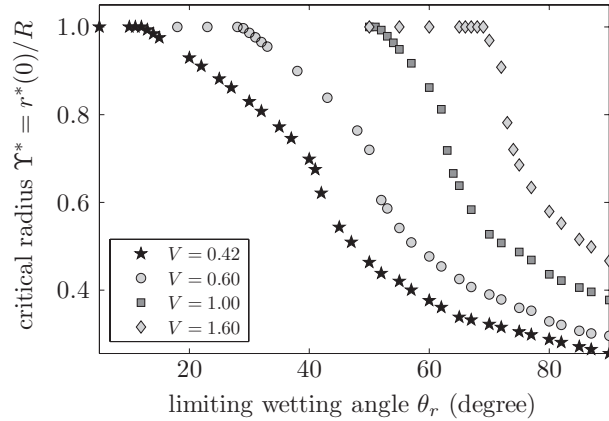


Figure 5.8: Calculated critical radius  $\Upsilon^* = r^*(0)/R$  as a function of limiting wetting angles  $\theta_r$  from static theory. Calculation are shown for four liquid volumes  $V = 0.42(\star)$ ,  $0.6(\circ)$ ,  $1.0(\square)$ ,  $1.6(\diamond)$ .

is higher than this threshold, the critical radius monotonically decreases as the limiting wetting angle rises. Since the higher limiting wetting angle is equivalent to lowering the surface wettability, the bridge starts breaking at a smaller value of  $\Upsilon$  on a more hydrophobic surface, which partially accounts for smaller deposition drops (Fig. 5.11). Moreover, the comparison in critical radius between different values of the bridge volume shows that, for the same minimum wetting angle, the smaller the volume, the smaller the critical radius that can be reached.<sup>1</sup>

### 5.4.3 Dynamics of the stretching liquid bridge

The static theory discussed above yields good predictions of the evolution of the liquid bridge prior to the critical state but, not surprisingly, it fails beyond this equilibrium boundary. To accurately model the dynamic bridge breakup and the contact line motion after the critical state, numerical calculations were performed using the one-dimensional model described in sec. 5.3.2. Both boundary conditions - the fixed contact angle and the dynamic variable contact angle - were implemented in numerical simulations to explore the effects of the velocity-dependent dynamic contact angle on

<sup>1</sup>For constant pressure dispensing, increasing the stretching speed is equivalent to lowering the rate at which the volume increases, and thus decreasing the critical radius. Therefore, raising the syringe speed creates smaller drops until the rod speed is much higher compared to the speed of fluid into the drop, at which the volume variation is negligible and the effect of the dynamic contact angle variation becomes dominant.

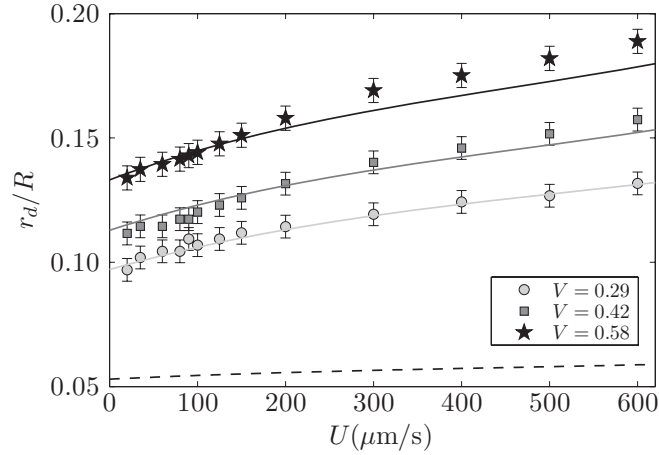


Figure 5.9: Calculated dispensing drop sizes (solid line) compared to experiment (symbols) for three bridge volumes. Here a dynamic contact angle model was included in the calculations with chosen parameters,  $\lambda = 0.02$ ,  $n = 1$ ,  $\theta_r = 85^\circ$ . Also shown are dispensing drop sizes from fixed contact angle calculation with  $\theta_r = 80^\circ$  for one volume  $V = 0.42$  (dash line).

the drop dispensing process.

### Predicting drop size

Figure 5.9 compares the calculated final drop sizes (solid line) for different rod speeds with those obtained from experiments (symbols) for three bridge volumes. The dynamic variable contact angle model was adopted in the numerical calculation, and the model parameters were adjusted to obtain good agreement between theory and experiment. Given this, it is perhaps not surprising that the numerical results agree well with the experiments, although it is reassuring that using a single set of parameters ( $\theta_r = 85^\circ$ ,  $\lambda = 0.02$ ,  $n = 1$ ) we are able to capture both the trend in which the drop size increases with rod speed, as well as the quantitative values obtained from experiment. Only at large bridge volumes do the predictions deviate in any significant manner from the measurements. For comparison, using a static contact angle,  $\theta_r$ , (dashed line) in the calculations gives very poor agreement with the corresponding measurements (squares) predicting drop sizes that are much smaller and only weakly dependent on the rod speed.

### Contact line speed

The discrepancy between the predictions obtained using the fixed and the dynamic variable angle calculations can be explained by the behavior of the contact line motion (Fig. 5.10-a). The contact line speeds from the dynamic contact angle calculation (solid lines) are plotted along with a single example from the fixed contact angle calculation (dashed line). Both calculations capture the general behavior observed in experiment. In the slowly-receding stage, calculations using both boundary conditions show only slight differences and both show little dependence on retraction speed (due to small variations in the receding angles). However, upon entering the high-speed stage, the contact line with a fixed contact angle moves much faster and the maximum contact line speed is ten times higher than that obtained using the dynamic angle calculation. The higher contact line speed leads directly to a smaller predicted drop size. In contrast, the contact line speed obtained using the dynamic contact angle calculation agrees with the experimental measurement not only in the slowly-receding stage but also in the high speed stage (Fig. 5.10-a). It is therefore not surprising that the dynamic contact angle model has a good prediction of dispensing drop sizes (Fig. 5.9). Comparing the maximum speeds found at different rod speeds shows that the radius at which contact line speed achieves its maximum increases slightly with  $U$ , in agreement with the experimental observation and the earlier discussion in sec. 5.4.1.

Also shown (Fig. 5.10-b) are the contact line speeds for three different bridge volumes, all obtained using the dynamic contact angle calculation. It is obvious that the larger volume liquid bridge experiences the sharp contact line acceleration at an earlier (i.e. larger) value of  $\Upsilon$ , and reaches a slightly lower maximum speed. Both of these contribute to the increase in the resultant drop size as a function of bridge volume (Fig. 5.9).

### Effects of surface wettability on drop sizes

The effects of different static receding angles on the dynamics of drop dispensing were not accessible in our experiments due to the difficulty of obtaining high quality surfaces with different surface

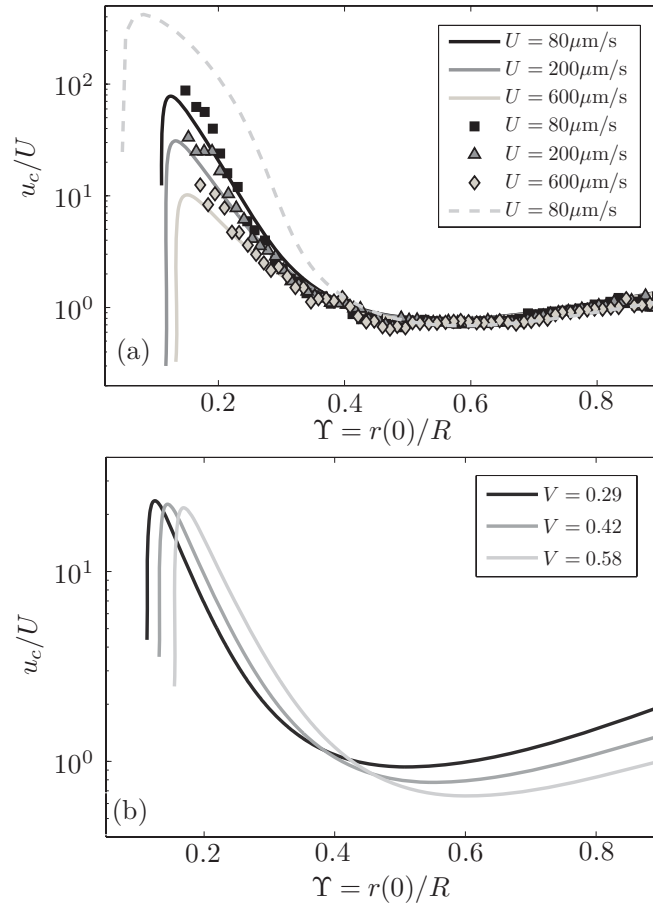


Figure 5.10: (a) Comparison in contact line speeds between experiments (symbols) and numerical calculations with the velocity dependent contact angle model in parameters  $\lambda = 0.02$ ,  $n = 1$ ,  $\theta_r = 85^\circ$  (solid line) and the fixed contact angle model  $\theta_r = 80^\circ$  (dash line). (a) Computed contact line receding speed at one stretching speed  $U = 200 \mu\text{m/s}$  for different volume values. A dynamic contact angle is applied as a boundary condition with parameters  $\lambda = 0.02$ ,  $n = 1$ ,  $\theta_r = 85^\circ$ .

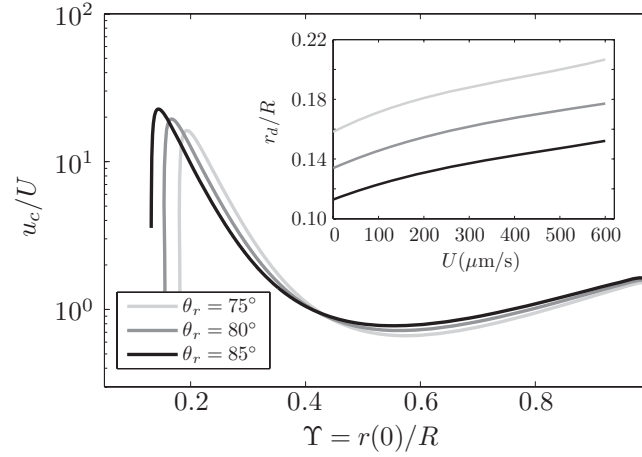


Figure 5.11: Effects of static receding angles  $\theta_r$  on the contact line speeds for one stretching speed  $U = 200 \mu\text{m/s}$  from dynamic contact angle calculation with the model parameters  $\lambda = 0.02$ ,  $n = 1$ . Corresponding dispensing drop sizes vs. stretching speeds are shown in the inset.

characteristics. However, this is easily explored in the simulations by changing  $\theta_r$  (keeping the other parameters in the model fixed at  $\lambda = 0.02$ ,  $n = 1$ ). Figure 5.11 shows the contact line speed, and resultant drop sizes for three static receding contact angles ( $V = 0.42$ ,  $U = 200 \mu\text{m/s}$ ). It is clear that as  $\theta_r$  decreases (i.e. increasing wettability), the liquid bridge becomes unstable at a larger critical radius, as predicted by the static analysis. However, in the dynamic pinch-off process, the stronger viscous drag prevents the contact line from following the rapid traction of the liquid bridge, which results in a lower maximum contact line speed and larger resultant drop size (Fig. 5.11).

### Sensitivity of drop sizes to the model parameters

Finally, we have already seen that the predictions of the resultant drop size obtained using the dynamic contact angle model are significantly more accurate than those obtained using the fixed contact angle model, and so it is not surprising that the results obtained from the numerical simulations are quite sensitive to the details of the dynamic contact angle model (parameters  $\lambda$  and  $n$ ) used (Fig. 5.12). For a fixed value of  $\lambda$ , the drop size increases with  $n$  at the same stretching speed and this behavior is more pronounced at higher stretching speeds. The size increase with  $n$  can be explained from the structure of the model (Eq. 5.6) by the fact that the maximum angle

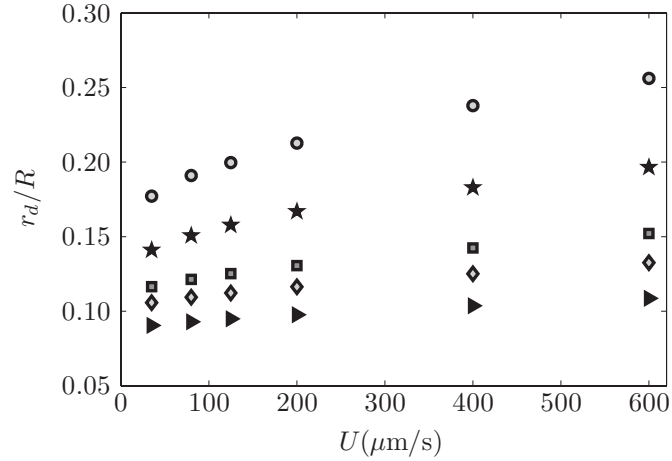


Figure 5.12: Influences of model parameters on the numerically calculated drop sizes. For  $\lambda = 0.03$ ,  $n = 1(\diamond)$ ,  $2(\star)$  and  $3(\circ)$ . For  $n = 1$ ,  $\lambda = 0.02(\square)$  and  $0.05(\triangleright)$ . Here the liquid bridge has a dimensionless volume  $V = 0.42$ .

variation,  $(\theta - \theta_r)$ , is less than one as the contact line recedes. For the same angle difference  $(\theta - \theta_r)$ , increasing  $n$  causes the contact line speed  $u_c$  to decrease, which, as we have seen above, leads to a smaller resultant drop. As  $n \rightarrow 0$  the contact line moves with less dependence on the contact angle, with which the drop size is expected to change slightly with the stretching speeds. For a fixed  $n$ , raising  $\lambda$  causes drop sizes to decrease because the contact line speed  $u_c$  is linearly proportional to  $\lambda$ . Numerical experiments with varying  $\lambda$  for  $n = 3$  shows that the drop size changes slowly with  $\lambda$  as the contact line speed  $u_c$  has a linear dependence on  $\lambda$  but is dominated by the power term:  $(\theta - \theta_r)^n$ . In the limit of  $\lambda \rightarrow 0$ , the contact line becomes immobile, which is identical to the stretching bridge with a fixed contact line.

## 5.5 CONCLUSION

We have used experimental and theoretical methods to understand the role of volume and surface wettability in the breakup of a stretching liquid bridge with a moving contact line. Unlike previous studies in which both contact lines are fixed, this system is strongly influenced by the details of the dynamic contact angle at the lower boundary, which controls the contact line motion and,

through this, the point at which the bridge becomes unstable to pinchoff. The configuration has many practical applications associated with drop dispensing from a syringe (constant pressure dispensing), although in the current case constant volume dispensing was studied in order to simplify the problem. Experimental measurements are reproduced with excellent accuracy using (i) a quasi-static analysis to predict the initial evolution of the bridge and the onset of contact line motion, (ii) a stability analysis to predict the onset of the rapid pinchoff of the column and (iii) a one-dimensional dynamical model, incorporating a variable contact line model, to predict the unsteady evolution of the bridge during the rapid pinchoff process.

For constant volume dispensing, a slight increase in the resultant drop size was observed as the bridge was stretched faster, an increase which can be attributed to the reduction in the time between the point at which the contact line starts to accelerate inwards and the point at which the liquid bridge breaks. Also drop size dependence on liquid volume was observed in experiment and can be explained (using the stability analysis) by the change in the critical radius as a function of the bridge volume. In addition, the effects of the equilibrium wetting angle on the critical radius were investigated within the framework of the the stability analysis and confirmed by both experiments and numerical calculations.

The combined effects of volume and dynamic break help to interpret the observed trend of the drop changing with the syringe speed in constant pressure dispensing, which shows a dramatic decrease in drop size at the beginning and down to a minimum the drop size slightly increases with the syringe speed. When the flow speed is still comparable to the syringe speed, the liquid volume determines the critical state of the liquid bridge and the role of the dynamic angle is insignificant. However, up to some point, the syringe speed is much higher than the flow speed and it can be assumed the volume change due to syringe speed is negligible. Similar to constant volume dispensing, the drop size slightly increases with syringe speed. The competition between the effects of volume and dynamic contact angle leads to a minimum drop size at an optimized syringe speed.

We also quantitatively investigated the influence of the dynamic contact angle on drop dispensing

by comparing the numerical results from calculations with conditions of fixed contact angle and dynamic variable contact angle. Although calculations with both conditions capture the essential features of the contact line motion, the numerical results from a dynamic contact angle model showed much better quantitative agreements with the experimental measurements. In the fixed contact angle calculation, the maximum contact line speed calculated is ten times higher than that observed in experiment, a discrepancy that leads to the prediction of smaller drop sizes that are observed in practice. Although the numerical calculation with a dynamic contact angle model matches well with experiments, this agreement is achieved by adjusting the model parameters, and it should be admitted that there is no general criteria for choosing the model parameters which may change from case to case. Moreover, the 1D model can not solve for the radial flow which will be significant when the contact line retreats at high speed. Exact numerical prediction of the dispensing drop size requires solving the full (two-dimensional) governing equations with an accurate model of the dynamic contact line, which couples length scales from microscopic (dynamic contact line) to macroscopic(liquid bridge).

## Chapter 6

# Conclusion

Through the first part of the manuscript, we studied two problems of fluid-structure interaction at low  $Re$  number. We first investigated the deformation of an elastic filament rotating in a viscous fluid. Its dynamic behaviors at various rotational moments were measured and compared with theoretical calculation. In addition, the governing dimensionless number was identified and its relation to the propulsion efficiency was calculated. Secondly, we used a simple model, a pair of rigid paddles, to demonstrate that hydrodynamic interaction indeed leads to synchronization. And the dependences of synchronization on model parameters were explored experimentally and analytically.

These studies can be extended to further examinations of microorganism locomotion. One natural extension is to investigate the hydrodynamic interaction between multiple rotating paddles, with connections to metachronal beating motions of cilia array. Another possibility is to investigate the interplay of shape deformation and hydrodynamic coordination. The locomotion in complex fluid is another area of future research, an area received increasing attention recently. Finally, the influence of environmental and actuation noise, resembling the thermal fluctuation and biochemical fluctuation of molecular motor for real bacteria, might be examined.

In the second part, we investigated contact drop dispensing on a hydrophobic surface. We

measured the changes of drop size with the dispensing speed, identified three dispensing regions, and proposed a scaling law governing drop dispensing. The mechanism in different dispensing regions has been interpreted with the aid of contact line measurement, stability analysis and numerical calculations. In particular, the dependence of liquid-bridge stability on the contact line movement was thoroughly discussed.

However, several issues related to contact drop dispensing remain unresolved. The first and most important one is the physical modeling of the rapid contact-line motions during bridge breakup. Another important issue is how the fluid properties affect the drop dispensing process, especially the influence of non-Newtonian rheology and dynamic surface tension in applications containing complex fluid. Finally, the pressure distributed inside the dispensing and the dynamic dispensing pressure control are crucial for determining and controlling the deposited drop size.

## Appendix A

# Oseen tensor for symmetric paddles

For  $\mathbf{H}$  evaluated at  $\mathbf{x}_i = \mathbf{0}$  and the matrices  $\mathbf{A}$ ,  $\mathbf{B}$ ,  $\mathbf{C}$ , and  $\mathbf{D}$  defined in Eqs. (3.31–3.32), expanding in powers of  $D^{-1}$  yields

$$\mathbf{A} = \begin{pmatrix} -\frac{1}{2} - \frac{9a}{32} - \frac{3}{32}a \cos(2\theta_1) & -\frac{3}{32}a \sin(2\theta_1) & -\frac{3a}{2D} & 0 \\ -\frac{3}{32}a \sin(2\theta_1) & -\frac{1}{2} - \frac{9a}{32} + \frac{3}{32}a \cos(2\theta_1) & 0 & -\frac{3a}{4D} \\ -\frac{3a}{2D} & 0 & -\frac{1}{2} - \frac{9a}{32} - \frac{3}{32}a \cos(2\theta_2) & -\frac{3}{32}a \sin(2\theta_2) \\ 0 & -\frac{3a}{4D} & -\frac{3}{32}a \sin(2\theta_2) & -\frac{1}{2} - \frac{9a}{32} + \frac{3}{32}a \cos(2\theta_2) \end{pmatrix} \quad (\text{A.1})$$

and

$$\mathbf{D} = \begin{pmatrix} -\frac{1}{2} - \frac{9a}{32} - \frac{3}{32}a \cos(2\theta_1) & -\frac{3}{32}a \sin(2\theta_1) & 0 & 0 \\ -\frac{3}{32}a \sin(2\theta_1) & \frac{1}{2} - \frac{9a}{32} + \frac{3}{32}a \cos(2\theta_1) & 0 & 0 \\ 0 & 0 & -\frac{1}{2} - \frac{9a}{32} - \frac{3}{32}a \cos(2\theta_2) & -\frac{3}{32}a \sin(2\theta_2) \\ 0 & 0 & -\frac{3}{32}a \sin(2\theta_2) & \frac{1}{2} - \frac{9a}{32} + \frac{3}{32}a \cos(2\theta_2) \end{pmatrix} \quad (\text{A.2})$$

for the blocks on the diagonal of the Oseen tensor. For the blocks off the diagonal, we have

$$\mathbf{B} = \begin{pmatrix} 0 & 0 & -\frac{3a^2}{2D^2} \cos \theta_2 & \frac{3a^2}{4D^2} \sin \theta_2 \\ 0 & 0 & \frac{3a^2}{4D^2} \sin \theta_2 & -\frac{3a^2}{2D^2} \cos \theta_2 \\ \frac{3a^2}{2D^2} \cos \theta_1 & -\frac{3a^2}{4D^2} \sin \theta_1 & 0 & 0 \\ -\frac{3a^2}{4D^2} \sin \theta_1 & \frac{3a^2}{2D^2} \cos \theta_1 & 0 & 0 \end{pmatrix} \quad (\text{A.3})$$

$$\mathbf{C} = \begin{pmatrix} 0 & 0 & -\frac{3a}{2D^2} \cos \theta_1 & \frac{3a}{4D^2} \sin \theta_1 \\ 0 & 0 & \frac{3a}{4D^2} \sin \theta_1 & -\frac{3a}{4D^2} \cos \theta_1 \\ \frac{3a}{2D^2} \cos \theta_2 & -\frac{3a}{4D^2} \sin \theta_2 & 0 & 0 \\ -\frac{3a}{4D^2} \sin \theta_2 & \frac{3a}{4D^2} \cos \theta_2 & 0 & 0 \end{pmatrix}. \quad (\text{A.4})$$

The second order spring deflection to leading order in  $\epsilon$  and  $a$  is

$$\mathbf{X}^{(2)} = a\epsilon \begin{pmatrix} (9/2)\dot{\theta}_2 \sin(2\theta_2) \\ -3\dot{\theta}_2 \\ -(9/2)\dot{\theta}_1 \sin(2\theta_1) \\ 3\dot{\theta}_1 \end{pmatrix} + \mathcal{O}(\epsilon a^2). \quad (\text{A.5})$$

The fourth order force difference to leading order in  $a$  and  $\epsilon$  is

$$\Delta \mathbf{F}^{(4)} \approx \frac{9}{4} a^2 \begin{pmatrix} -\dot{\theta}_1 [5 \sin \theta_1 + 3 \sin(3\theta_1)] \\ 2\dot{\theta}_1 \cos \theta_1 (1 + 3 \sin^2 \theta_1) \\ -\dot{\theta}_2 [5 \sin \theta_2 + 3 \sin(3\theta_2)] \\ 2\dot{\theta}_2 \cos \theta_2 (1 + 3 \sin^2 \theta_2) \end{pmatrix}. \quad (\text{A.6})$$

The third order spring deflection, leading order in  $\epsilon$  and  $a$ ,

$$\mathbf{X}^{(3)} = \frac{9}{2}a^2\epsilon \begin{pmatrix} 3\dot{\theta}_1 \sin(2\theta_1) \\ -\dot{\theta}_1 \\ -3\dot{\theta}_2 \sin(2\theta_2) \\ \dot{\theta}_2 \end{pmatrix}. \quad (\text{A.7})$$

Finally, again to leading order in  $\epsilon$  and  $a$ ,

$$\Delta \mathbf{F}^{(5)} = \frac{27}{4}a^3 \begin{pmatrix} -\dot{\theta}_2 [\sin \theta_1 + 6 \cos \theta_1 \sin(2\theta_2)] \\ \dot{\theta}_2 [\cos \theta_1 + 3 \sin \theta_1 \sin(2\theta_2)] \\ -\dot{\theta}_1 [\sin \theta_2 + 6 \cos \theta_2 \sin(2\theta_1)] \\ \dot{\theta}_1 [\cos \theta_2 + 3 \sin \theta_2 \sin(2\theta_1)] \end{pmatrix}. \quad (\text{A.8})$$

# Bibliography

- [1] X.-L. Wu and A. Libchaber, Particle diffusion in a quasi-two-dimensional bacterial bath, *Phys. Rev. Lett.* **84**, 3017 (2000).
- [2] M. J. Kim and K. S. Breuer, Enhanced diffusion due to motile bacteria, *Phys. Fluids* **16**, L78 (2004).
- [3] H. C. Berg, *E. coli in Motion*, Springer-Verlag, biological and medical physics series edition, (2003).
- [4] H. Mao, P. S. Cremer, and M. D. Manson, A sensitive, versatile microfluidic assay for bacterial chemotaxis, *Proc. Natl. Acad. Sci. USA* **100**, 5449 (2003).
- [5] A. Terray, J. Oakey, and D. W. M. Marr, Microfluidic control using colloidal devices, *Science* **296**, 1841 (2002).
- [6] L. Turner, W. S. Ryu, and H. C. Berg, Real-time imaging of fluorescent flagellar filaments, *J. Bacteriol.* **182**, 2793 (2000).
- [7] H. Ho and S. Suarez, Hyperactivation of mammalian spermatozoa: function and regulation, *Reproduction* **122**, 519 (2001).
- [8] E. M. Purcell, Life at low Reynolds number, *Am. J. Physics* **45**, 3 (1977).

- [9] P. Satir, Studies on cilia: III. further studies on the cilium tip and a “sliding filament” model of ciliary motility, *J. Cell Biol.* **39**, 77 (1968).
- [10] D. Bray, *Cell movements*, Garland Publishing, Inc., New York, (1992).
- [11] K. E. Machin, Wave propagation along flagella, *J. Exp. Biol.* **35**, 796 (1958).
- [12] J. Gray and G. J. Hancock, The propulsion of sea-urchin spermatozoa, *J. Exp. Biol.* **32**, 802 (1955).
- [13] C. H. Wiggins and R. E. Goldstein, Flexive and propulsive dynamics of elastica at low Reynolds number, *Phys. Rev. Lett.* **80**, 3879 (1998).
- [14] T. S. Yu, E. Lauga, and A. E. Hosoi, Experimental investigations of elastic tail propulsion at low Reynolds number, *Phys. Fluids* **18**, 091701 (2006).
- [15] M. Manghi, X. Schlagberger, and R. R. Netz, Propulsion with a rotating elastic nanorod, *Phys. Rev. Lett.* **96**, 068101 (2006).
- [16] M. Manghi, X. Schlagberger, Y.-W. Kim, and R. R. Netz, Hydrodynamic effects in driven soft matter, *Soft Matter* **2**, 653 (2006).
- [17] M. Polin, I. Tuval, K. Drescher, J. P. Gollub, and R. E. Goldstein, *Chlamydomonas* swims with two “gears” in a eukaryotic version of run-and-tumble locomotion, *Science* **325**, 487 (2009).
- [18] R. E. Goldstein, M. Polin, and I. Tuval, Noise and synchronization in pairs of beating eukaryotic flagella, *Phys. Rev. Lett.* **103**, 168103 (2009).
- [19] J. Gray, The mechanism of ciliary movement, *The American Naturalist* **63**, 68 (1929).
- [20] H. Machemer, Ciliary action and the origin of metachrony in *Paramecium*: effects of increased viscosity, *J. Exp. Biol.* **57**, 239 (1972).

- [21] S. S. Suarez and A. A. Pacey, Sperm transport in the female reproductive tract, *Human Reprod. Update* **12**, 23 (2006).
- [22] S. Nonaka, Y. Tanaka, S. Takeda, A. Harada, Y. Kanai, M. Kido, and N. Hirokawa, Randomization of left-right asymmetry due to loss of nodal cilia generating leftward flow of extraembryonic fluid in mice lacking KIF3b motor protein, *Cell* **95**, 829 (1998).
- [23] M. Bennett, M. F. Schatz, H. Rockwood, and K. Wiesenfeld, Huygens's clocks, *Proc. R. Soc. Lond. A* **458**, 563 (2002).
- [24] G. I. Taylor, Analysis of the swimming of microscopic organism, *Proc. R. Soc. London, Ser. A* **209**, 447 (1951).
- [25] S. Gueron, K. Levit-Gurevich, N. Liron, and J. J. Blum, Cilia internal mechanism and metachronal coordination as the result of hydrodynamical coupling, *Proc. Natl. Acad. Sci. USA* **94**, 6001 (1997).
- [26] S. Gueron and K. Levit-Gurevich, Computation of the internal forces in cilia: application to ciliary motion, the effects of viscosity, and cilia interactions, *Biophys. J.* **74**, 1658 (1998).
- [27] T. Niedermayer, B. Eckhardt, and P. Lenz, Synchronization, phase locking, and metachronal wave formation in ciliary chains, *Chaos* **18**, 037128 (2008).
- [28] P. Lenz and A. Ryskin, Collective effects in ciliar arrays, *Phys. Biol.* **3**, 285 (2006).
- [29] M. Reichert and H. Stark, Synchronization of rotating helices by hydrodynamic interactions, *Eur. Phys. J. E* **17**, 493 (2005).
- [30] M. J. Kim and T. R. Powers, Hydrodynamic interactions between rotating helices, *Phys. Rev. E* **69**, 061910 (2004).
- [31] U. R. Müller and D. V. Nicolau, *Microarray Technology and Its Application*, Springer, (2004).

- [32] D. S. Ginger, H. Zhang, and C. A. Mirkin, The evolution of dip-pen nanolithography, *Angew. Chem.* **43**, 30 (2004).
- [33] S. Deladi, N. R. Tas, J. W. Berenschot, G. J. M. Krijnen, M. J. de Boer, J. H. de Boer, M. Peter, and M. C. Elwenspoek, Micromachined fountain pen for atomic force microscope-based nanopatterning, *Appl. Phys. Lett.* **85**, 5361 (2004).
- [34] A. U. Chen and O. A. Basaran, A new method for significantly reducing drop radius without reducing nozzle radius in drop-on-demand drop production, *Phys. of Fluids* **14**, L1 (2002).
- [35] J. Plateau, Experimental and theoretical researches on the figures of equilibrium of a liquid mass withdrawn from the action of gravity, *Annual Report of the Board of Regents of the Smithsonian Institution* , 207 (1863).
- [36] L. Rayleigh, On the instability of jets, *Proc. Lond. Math. Soc.* **10** , 4 (1878).
- [37] J. Plateau, *Statique expérimentale et théorique des liquides soumis aux seules forces moléculaires*, Gauthier-Villars, Tubner et cie, F. Clemm, (1873).
- [38] I. Martinez, Stability of axisymmetric liquid bridges, ESA SP-191, ESA, Paris , 267 (1983).
- [39] S. R. Coriell, S. C. Hardy, and M. R. Cordes, Stability of liquid zones, *J. Colloid Interface Sci.* **60**, 126 (1977).
- [40] J. M. Vega and J. M. Perales, Almost cylindrical isorotating liquid bridges for small bond numbers, ESA SP-191, ESA, Paris , 247 (1983).
- [41] J. Meseguer, Stability of slender, axisymmetric liquid bridges between unequal disks, *J. Crystal Growth* **67**, 141 (1984).
- [42] A. D. Myshkis, V. G. Babskii, N. D. Kopachevskii, L. A. Slobozhanin, and A. D. Tyuptsov, *Low-Gravity Fluid Mechanics*, Springer-Verlag, (1987).

- [43] L. A. Slobozhanin and J. M. Perales, Stability of liquid bridges between equal disks in an axial gravity field, *Phys. Fluids A* **5**, 1305 (1993).
- [44] J. M. Perales, J. Meseguer, and I. Martinez, Minimum volume stability limits for axisymmetric liquid bridges subject to steady axial acceleration, *J. Crystal Growth* **110**, 885 (1991).
- [45] L. A. Slobozhanin and J. I. D. Alexander, Combined effect of disk inequality and axial gravity on axisymmetric liquid bridge stability, *Phys. Fluids* **10**, 2473 (1998).
- [46] J. Meseguer and A. Sanz, Numerical and experimental study of the dynamics of axisymmetric slender liquid bridges, *J. Fluid Mech.* **153**, 83 (1985).
- [47] J. Eggers, Universal pinching of 3d axisymmetric free-surface flow, *Phys. Rev. Lett.* **71**, 3458 (1993).
- [48] X. Zhang, R. S. Padgett, and O. A. Basaran, Nonlinear deformation and breakup of stretching liquid bridges, *J. Fluid Mech.* **329**, 207 (1996).
- [49] B. Qian, M. Loureiro, D. A. Gagnon, A. Tripathi, and K. S. Breuer, Micron-scale droplet deposition on a hydrophobic surface using a retreating syringe, *Phys. Rev. Lett.* **102**, 164502 (2009).
- [50] O. E. Yildirim and O. A. Basaran, Deformation and breakup of stretching bridges of newtonian and shear-thinning liquids: comparison of one- and two-dimensional models, *Chem. Eng. Sci.* **56**, 211 (2001).
- [51] Y. C. Liao, E. I. Franses, and O. A. Basaran, Deformation and breakup of a stretching liquid bridge covered with an insoluble surfactant monolayer, *Phys. Fluids*. **18**, 022101 (2006).
- [52] J. C. Panditaratne, *Deflection of microjets induced by asymmetric heating and related free surface flows with moving contact lines*, PhD thesis, Purdue University, 2003.

- [53] A. M. Alencar, E. Wolfe, and S. V. Buldyrev, Monte Carlo simulation of liquid bridge rupture: application to lung physiology, *Phys. Rev. E* **74**, 026311 (2006).
- [54] B. Basic, J. Koplik, and J. Banavar, Molecular dynamics simulation of liquid bridge extensional flows, *J. of Non-Newtonian Fluid Mech.* **109**, 51 (2003).
- [55] J. T. Smith, B. L. Viglianti, and W. M. Reichert, Spreading diagrams for the optimization of quill pin printed microarray density, *Langmuir* **18**, 6289 (2002).
- [56] S. Camalet, F. Jülicher, and J. Prost, Self-organized beating and swimming of internally driven filaments, *Phys. Rev. Lett.* **82**, 1590 (1999).
- [57] H. A. Praetorius and K. R. Spring, A physiological view of the primary cilium, *Annu. Rev. Physiol.* **67**, 515 (2005).
- [58] M. J. Kim, J. C. Bird, A. J. Van Parys, K. S. Breuer, and T. R. Powers, A macroscopic scale model of bacterial flagellar bundling, *Proc. Natl. Acad. Sci. USA* **100**, 15481 (2003).
- [59] R. Dreyfus, J. Baudry, M. L. Roper, M. Fermigier, H. A. Stone, and J. Bibette, Microscopic artificial swimmers, *Nature* **437**, 862 (2005).
- [60] J. B. Keller and S. I. Rubinow, Slender body theory for viscous flow, *J. Fluid Mech.* **75**, 705 (1976).
- [61] C. W. Wolgemuth, T. R. Powers, and R. E. Goldstein, Twirling and whirling: viscous dynamics of rotating elastic filaments, *Phys. Rev. Lett.* **84**, 1623 (2000).
- [62] S. Lim and C. S. Peskin, Simulations of the whirling instability by the immersed boundary method, *SIAM J. Sci. Comput.* **25**, 2066 (2004).
- [63] H. Wada and R. R. Netz, Non-equilibrium hydrodynamics of a rotating filament, *Euro. Phys. Lett.* **75**, 645 (2006).

- [64] L. D. Landau and E. M. Lifshitz, *Theory of elasticity*, Pergamon Press, Oxford, 3rd edition, (1986).
- [65] T. R. Powers, Role of body rotation in bacterial flagellar bundling, *Phys. Rev. E* **65**, 040903(R) (2002).
- [66] S. A. Koehler and T. R. Powers, Twirling elastica: kinks, viscous drag, and torsional stress, *Phys. Rev. Lett.* **85**, 4827 (2000).
- [67] W. H. Press, W. T. Vetterling, S. A. Teukolsky, and B. P. Flannery, *Numerical Recipes in C*, Cambridge University Press, Cambridge, England, 2nd edition, (1992).
- [68] E. Lauga, Floppy swimming: viscous locomotion of actuated elastica, *Phys. Rev. E* **75**, 041916 (2007).
- [69] I. H. Riedel, K. Kruse, and J. Howard, A self-organized vortex array of hydrodynamically entrained sperm cells, *Science* **309**, 300 (2005).
- [70] A. Pikovsky, M. Rosenblum, and J. Kurths, *Synchronization. A universal concept in nonlinear science*, Cambridge University Press, Cambridge, (2001).
- [71] J. Gray, *Ciliary movement*, Cambridge University Press, Cambridge, U.K., (1928).
- [72] M. A. Sleight, ed., *Cilia and flagella*, Academic Press, London, (1974).
- [73] L. J. Fauci, Interaction of oscillating filaments - A computational study, *J. Comp. Phys.* **86**, 294 (1990).
- [74] M. C. Lagomarsino, P. Jona, and B. Bassetti, Metachronal waves for deterministic switching two-state oscillators with hydrodynamic interaction, *Phys. Rev. E* **68**, 021908 (2003).
- [75] M. C. Lagomarsino, B. Bassetti, and P. Jona, Rows coupled hydrodynamically. Modeling possible mechanisms for the cooperation of cilia, *Europ. Phys. J. B* **26**, 81 (2002).

- [76] A. Vilfan and F. Jülicher, Hydrodynamic flow patterns and synchronization of beating cilia, *Phys. Rev. Lett.* **96**, 058102 (2006).
- [77] B. Guirao and J. F. Joanny, Spontaneous creation of macroscopic flow and metachronal waves in an array of cilia, *Biophys. J.* **92**, 1900 (2007).
- [78] G. J. Elfring and E. Lauga, Hydrodynamic phase locking of swimming microorganisms, *Phys. Rev. Lett.* **103**, 088101 (2009).
- [79] G. P. Alexander and J. M. Yeomans, Dumb-bell swimmers, *Euro. Phys. Lett.* **83**, 34006 (2008).
- [80] E. Lauga and D. Bartolo, No many-scallop theorem: Collective locomotion of reciprocal swimmers, *Phys. Rev. E* **78**, 030901 (2008).
- [81] S. Cortez, The method of regularized Stokeslets, *SIAM J. Sci. Comput.* **23**, 1204 (2001).
- [82] M. Doi and S. Edwards, *The theory of polymer dynamics*, Oxford University Press, Oxford, (1986).
- [83] S. H. Strogatz, *Nonlinear dynamics and chaos*, Perseus Books, Reading, MA, (1994).
- [84] W. Russel, D. Saville, and W. Schowalter, *Colloidal dispersions*, Cambridge University Press, Cambridge, (1989).
- [85] N. Moldovan, K.-H. Kim, and H. D. Espinosa, Design and fabrication of a novel microfluidic nanoprobe, *J. of Microelectromechanical Sys.* **15**, 204 (2006).
- [86] T. Leïchlé, L. Tanguy, and L. Nicu, Electrowetting-assisted drop deposition for controlled spotting, *Appl. Phys. Lett.* **91**, 224102 (2007).
- [87] B.-T. Pinhas, B. R. Mrad, , and A. A. Goldenberg, A conceptual design and FE analysis of a piezoceramic actuated dispensing system for microdrops generation in microarray applications, *Mechatronics* **17**, 1 (2007).

- [88] A. Meister, M. Liley, J. Brugger, R. Pugin, and H. Heinzelmann, Nanodispenser for attoliter volume deposition using atomic force microscopy probes modified by focused-ion-beam milling, *Appl. Phys. Lett.* **85**, 6260 (2004).
- [89] L. A. Slobozhanin, J. I. D. Alexander, and A. H. Resnick, Bifurcation of the equilibrium states of a weightless liquid bridge, *Phys. Fluids* **9**, 1893 (1997).
- [90] J. Eggers and T. F. Dupont, Drop formation in a one-dimensional approximation of the Navier-Stokes equation, *J. Fluid Mech.* **262**, 205 (1994).
- [91] G. H. McKinley and A. Tripathi, How to extract the newtonian viscosity from capillary breakup measurements in a filament rheometer, *J. Rheol.* **44**, 653 (2000).
- [92] W. Villanueva, J. Sjö Dahl, M. Stjernström, J. Roeraade, and G. Amberg, Microdroplet deposition under a liquid medium, *Langmuir* **23**, 1171 (2007).
- [93] C. Huh and L. Scriven, Hydrodynamic model of steady movement of a solid/liquid/fluid contact line, *J. Coll. Int. Sci.* **35**, 85 (1971).
- [94] J. Eggers and H. A. Stone, Characteristic lengths at moving contact lines for a perfectly wetting fluid: the influence of speed on the dynamic contact angle, *J. Fluid Mech.* **505**, 309 (2004).
- [95] D. Bonn, J. Eggers, J. Indekeu, J. Meunier, and E. Rolley, Wetting and spreading, *Rev. Mod. Phys.* **81**, 739 (2009).
- [96] B. Qian and K. S. Breuer, The motion, stability and breakup of a stretching liquid bridge with a receding contact line, submitted to *J. Fluid Mech.* (2010).
- [97] G. C. Mason, An experimental determination of the stable length of cylindrical liquid bubbles, *J. Colloid Interface Sci.* **32**, 172 (1970).

- [98] R. D. Gillette and D. C. Dyson, Stability of fluid interfaces of revolution between equal solid circular plates, *Chem. Eng. J.* **2**, 44 (1971).
- [99] A. Sanz and I. Martinez, Minimum volume for a liquid bridge between equal disks, *J. Colloid Interface Sci.* **93**, 235 (1983).
- [100] M. J. Russo and P. H. Steen, Instability of rounded capillary bridges to general disturbances, experiment and theory, *J. Colloid Interface Sci.* **113**, 154 (1986).
- [101] I. Frankel and D. Weihs, Stability of a capillary jet with linearly increasing axial velocity (with application to shaped charges), *J. Fluid Mech.* **155**, 289 (1985).
- [102] D. T. Papageorgiou, Analytical description of the breakup of liquid jets, *J. Fluid Mech.* **301**, 109 (1995).
- [103] S. Dodds, M. da Silveira Carvalho, and S. Kumar, Stretching and slipping of liquid bridges near plates and cavities, *Phys. Fluid* **21**, 092103 (2009).
- [104] A. Oron, S. H. Davis, and S. G. Bankoff, Long scale evolution of thin liquid films, *Rev. Mod. Phys.* **69**, 3 (1997).
- [105] L. H. Tanner., The spreading of silicone oil drops on horizontal surfaces, *J. Phys. D: Appl. Phys.* **12**, 1473 (1979).
- [106] E. B. Dussan V, On the spreading of liquid on the solid surfaces: static and dynamic contact lines, *Annu. Rev. Fluid Mech.* **11**, 371 (1979).
- [107] S. K. Wilson, R. Hunt, and B. R. Duffy, The rate of spreading in spin coating, *J. Fluid Mech.* **413**, 65 (2000).
- [108] D. G. Arts, H. N. Lekkerkerker, H. Guo, G. H. Wegdam, and D. Bonn, Hydrodynamics of droplet coalescence, *Phys. Rev. Lett.* **95**, 164503 (2005).

- [109] S. T. Thoroddesen, K. Takehara, and T. G. Etoh, The coalescence speed of a pendent and a sessile drop, *J. Fluid Mech.* **527**, 85 (2005).
- [110] J. C. Bird, S. Mandre, and H. A. Stone, Short-time dynamics of partial wetting, *Phys. Rev. Lett.* **100**, 234501 (2008).
- [111] J. Eggers, J. R. Lister, and H. A. Stone, Coalescence of liquid drops, *J. Fluid Mech.* **401**, 293 (1999).